

**TEMPORAL MODE STRUCTURE AND ITS MEASUREMENT
OF ENTANGLED FIELDS IN CONTINUOUS AND DISCRETE
VARIABLES**

by

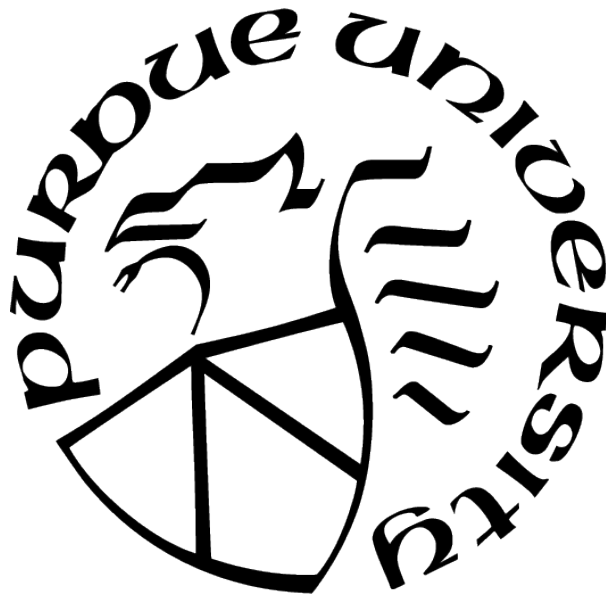
Xin Chen

A Dissertation

Submitted to the Faculty of Purdue University

In Partial Fulfillment of the Requirements for the degree of

Doctor of Philosophy



Department of Physics and Astronomy

West Lafayette, Indiana

August 2021

**THE PURDUE UNIVERSITY GRADUATE SCHOOL
STATEMENT OF COMMITTEE APPROVAL**

Dr. Zhe-Yu Jeff Ou, Chair

Department of Physics

Dr. Yogesh N Joglekar

Department of Physics

Dr. Horia Petrache

Department of Physics

Dr. Gautam Vemuri

Department of Physics

Dr. Daniel S. Elliott

Department of Physics and Astronomy

Approved by:

Dr. Ricardo Decca

ACKNOWLEDGMENTS

This work was supported in part by National Natural Science Foundation of China (91836302, 91736105, 11527808), the National Key Research and Development Program of China (2016YFA0301403), and in part by US National Science Foundation (Grant No. 1806425).

TABLE OF CONTENTS

| | |
|--|----|
| LIST OF FIGURES | 6 |
| ABSTRACT | 11 |
| 1 INTRODUCTION | 13 |
| 2 QUANTUM AND NONLINEAR OPTICS | 18 |
| 2.1 Background Knowledge of Quantum Optics | 18 |
| 2.1.1 Optical Modes | 23 |
| 2.1.2 Continuous and Discrete Variables | 28 |
| 2.2 Nonlinear Optics | 31 |
| 2.2.1 Classical Wave Theory of Nonlinear Optics | 31 |
| 2.2.2 Quantum Optical Theory of Nonlinear Optics | 33 |
| 2.2.3 Phase Matching Condition | 34 |
| 2.2.4 Spontaneous Parametric Down-conversion | 37 |
| Expansion of Joint Spectrum Function with Temporal Modes | 39 |
| 3 MEASUREMENT OF TEMPORAL MODE STRUCTURE OF ENTANGLED FIELDS IN CONTINUOUS AND DISCRETE VARIABLES | 44 |
| 3.1 Direct Temporal Mode Measurement for High Gain Parametric Amplifier | 44 |
| 3.1.1 Theoretical Simulation and Experimental Results | 47 |
| 3.2 Direct Temporal Mode Measurement for Low Gain Parametric Amplifier | 51 |
| 3.2.1 Simulations of Temporal Mode Determination Processes | 55 |
| 4 MODE STRUCTURE OF A BROADBAND HIGH GAIN PARAMETRIC AM- PLIFIER | 65 |
| 4.1 Multi-stage $SU(1,1)$ Interferometers | 66 |
| 4.2 Broadband Parametric Amplifier | 71 |
| 4.3 Eigen-modes of High Gain Parametric Processes | 76 |
| 4.4 Numerical Solutions | 78 |

| | | |
|-------|--|-----|
| 4.A | Appendix | 84 |
| 5 | MEASUREMENT OF JOINT SPECTRAL DENSITY | 89 |
| 5.1 | Research Background | 89 |
| 5.1.1 | Quasi-phase Matching for Periodic Poled Material | 91 |
| 5.1.2 | Experimental Implementation | 94 |
| 5.1.3 | Experimental Results and Discussions | 99 |
| 6 | PARAMETRIC AMPLIFIER FOR BELL MEASUREMENT IN CONTINUOUS-VARIABLE QUANTUM STATE TELEPORTATION | 104 |
| 6.1 | Quantum State Transformation of a Parametric Amplifier | 105 |
| 6.2 | Application to Quantum State Teleportation | 109 |
| 6.3 | Tolerance to Detection Loss | 111 |
| 6.4 | Influence of Losses via Fidelity | 114 |
| 6.4.1 | Scheme with Beam Splitter | 114 |
| 6.4.2 | Scheme with Parametric Amplifier | 117 |
| 6.5 | Influence of Loss on Entanglement | 122 |
| 6.5.1 | Fidelity | 122 |
| 6.5.2 | Inseparability | 125 |
| 6.6 | Summary and Discussion | 127 |
| 6.A | Appendix | 128 |
| 6.A.1 | Derivation of input-output relation of Wigner function for a PA [Eq.(6.6)] | 128 |
| 6.A.2 | Derivation of Eqs.(6.27) and (6.33) | 129 |
| 6.A.3 | Fidelity for Coherent States with Finite s and G | 131 |
| 7 | SUMMARY | 134 |
| | REFERENCES | 136 |

LIST OF FIGURES

| | | |
|------|--|----|
| 2.1 | (a) Phase-space portrait of the coherent state with the Wigner function. (b) The coherent state revolves about the origin in Phase-space and projected onto the $X - t$ space | 21 |
| 2.2 | Wigner function for a number state $ n\rangle$ | 22 |
| 2.3 | (a) Young’s double slit experiment. The pure-wavelength light sent through two slits is diffracted into a fringes pattern. (b) The visibility of the interference pattern of double slit experiment reduces for broadband light source | 25 |
| 2.4 | Two dimensional Cartesian coordinate system has the basis of x, y axis. The linear combination of the original basis $X = x\cos\theta + y\sin\theta, Y = -x\sin\theta + y\cos\theta$ is also a basis. | 26 |
| 2.5 | (a) Arbitrary function can be expanded in an infinite dimensional space with the basis vector of $\delta(x - x')$. The index for the basis vector is x' (b) The function can be expanded with the new basis of Fourier transform functions e^{ik_jx} , too. The index of the basis vector is k_j | 27 |
| 2.6 | The first three mode amplitudes for an example of the TM. Each mode is orthogonal to each other. | 28 |
| 2.7 | (a) The quantum fluctuation is amplified too when the intensity of the field is amplified by the Homodyne detection technique. (b) Continuous photon-current under relatively strong light intensity. (c) Photon counting technique for weak optical fields. | 30 |
| 2.8 | The pump field (the red line) at frequency 2ω propagates in a $\chi^{(2)}$ crystal. Second harmonic generated field (the blue line) at frequency 2ω is generated through the medium. When the phase matching condition is satisfied, the waves of generated fields at different locations propagate in phase with each other and amplitudes add constructively. | 35 |
| 2.9 | Comparison of second harmonic generation when it is phase-matched, phase mismatched and quasi-phase matched. The amplitude of the second harmonic generated field increases exponentially when the phase matching condition is satisfied (the solid line). When the phase is mismatched, the generated field oscillates at low amplitude and there is almost no output field (the dashed line). Quasi-phase matching technique alternates crystal orientation periodically so that the energy flows positively consecutively from the pump field to the second harmonic generated field (the dash-dot line). | 37 |
| 2.10 | Schematic of SPDC process. The process obeys the conservation law of momentum and energy. | 39 |

| | | |
|------|---|----|
| 2.11 | Normalized absolute value of the JSF $ F(\Omega_1, \Omega_2)/F(0, 0) $ of twin beams generated by a pulse pumped SPDC process. The frequency is in the unit of the power of the pump field σ_p | 40 |
| 2.12 | Entangled two-photon states consisting of various TMs A_k, B_k ($k = 1, 2, 3, \dots$) in the signal and idler fields generated from a pulse-pumped parametric process (Adapted from Ref.[39]). | 43 |
| 3.1 | Schematic diagram for measuring the mode functions at high gain. WS: wave shaper. | 45 |
| 3.2 | Working principle: Arbitrary field can be expanded with TMs. The fields of each mode are amplified independently with the amplification rate proportional to the $(\cosh G_k)/G'$. The mode with the largest amplification will be left after iterating the process. | 48 |
| 3.3 | Simulation results for the amplitudes (top) and converged phases (bottom) of the output spectral functions $\psi_k(\Omega_s)$ ($\Omega_s \equiv \omega_s - \omega_{s0}$ in the unit of pump bandwidth σ_p) for (a) $k = 1$, (b) $k = 2$, (c) $k = 3$. The green curves are the input spectral functions while the blue and red curves are intermediate outputs after the iteration steps N indicated in the legends. The dashed curves are the final outputs. | 49 |
| 3.4 | Measured spectral intensity $ \psi_k(\omega) ^2$ for $k =$ (a) 1, (b) 2, (c) 3, and those ((d),(e),(f)) for the corresponding idler field (Adapted from Ref.[19]). The dotted lines are the initially injected seed (not shown for (c) due to crowdedness). The pink curve in (a) is the output after two iterations. The blue lines are the output signal and the red lines are the feedback to the input (red is covered by blue in (a)). (g) is the experimental setup. WS, wave shaper; FOPA, fiber optical parametric amplifier; OSA, optical spectrum analyzer. | 50 |
| 3.5 | Schematic diagram for measuring the mode functions at low gain (Adapted from Ref.[39]). WS: wave shaper. The directly related light fields have the same line style (dashed or solid) and color (red or blue) and the direction of the arrow shows the flow of the iteration. The converged functions are the outputs that give the measured mode functions $\psi_k(\omega), \varphi_k(\omega)$ | 52 |
| 3.6 | Simulated convergent output spectral functions with their magnitudes and phases for the first three modes $k = 1, 2, 3$ for the JSF given in Eq.(3.27) (Adapted from Ref.[39]). (a) signal field $\psi_k(\Omega_s)$ and (b) idler field $\varphi_k(\Omega_i)$. The green dash-dotted curves are the input spectral functions while the blue dotted and red solid curves are intermediate outputs after the iteration steps indicated in the legends. The black dashed curves are the final outputs. | 58 |
| 3.7 | Mode number distribution obtained by simulation for the JSF given in Eq.(3.27) (Adapted from Ref.[39]). | 59 |

| | | |
|------|---|----|
| 3.8 | Simulated convergent output spectral functions with their magnitudes and phases for the first three modes $k = 1, 2, 3$ for the JSF given in Eq.(3.27) but with a chirped pump phase of $e^{i(\Omega_s+\Omega_i)^2/\sigma_p^2}$ (Adapted from Ref.[39]). (a) signal field $\psi_k(\Omega_s)$ and (b) idler field $\varphi_k(\Omega_i)$. The green dash-dotted curves are the input spectral functions while the blue dotted and red solid curves are intermediate outputs after the iteration steps indicated in the legends. The black dashed curves are the final outputs. | 60 |
| 3.9 | Mode number distribution obtained by simulation for the JSF given in Eq.(3.27) but with a modified phase of $e^{i(\Omega_s+\Omega_i)^2/\sigma_p^2}$ added due to chirping of the pump field (Adapted from Ref.[39]). | 61 |
| 3.10 | Normalized ratio $R_k^{(M)}/Gr_1(k = 1, 2, 3)$ as a function of iteration step M , (a) ; obtained by simulation for the JSF given in Eq.(3.27) (Adapted from Ref.[39]), (b) for the JSF given in Eq.(3.27) but with a modified phase of $e^{i(\Omega_s+\Omega_i)^2/\sigma_p^2}$ added due to chirping of the pump field. The straight lines are the limiting values of r_k/r_1 | 64 |
| 4.1 | An SU(1,1) interferometer with PAs (PA ₁ ,PA ₂) in place of beam splitters (Adapted from Ref.[49]). | 66 |
| 4.2 | A multi-stage SU(1,1) interferometer (Adapted from Ref.[49]). | 68 |
| 4.3 | A PA from a single-pass pulse-pumped nonlinear medium (Adapted from Ref.[49]). | 73 |
| 4.4 | Contour plot of the amplitude of $h_{2a}(\Omega_1, \Omega_2)$ for $K =$ (a) 0.01, (b) 2, (c) 4, (d) 10. $\Omega_i \equiv (\omega_i - \omega_{i0})/\sigma_p$ ($i = 1, 2$) (Adapted from Ref.[49]). | 79 |
| 4.5 | The amplitude function $\psi_1^{(a)}$ of mode 1 for pump parameter $K = 0.01, 2, 4, 10$, showing the broadening of the width. Inset: the full width at half maximum (FWHM) of mode 1 function as a function of the pump parameter K (Adapted from Ref.[49]). | 80 |
| 4.6 | Mode coefficients r_k/r_1 as a function of dimensionless pump parameter K (Adapted from Ref.[49]). | 80 |
| 4.7 | Contour plot of the amplitude of $h_{2a}(\Omega_1, \Omega_2)$ for the case of $1/\Delta_1 = 2.198, 1/\Delta_2 = -2.198$ with $K =$ (a) 0.01, (b) 2, (c) 4, (d) 10. $\Omega_i \equiv (\omega_i - \omega_{i0})/\sigma_p$ ($i = 1, 2$) (Adapted from Ref.[49]). | 82 |
| 4.8 | Mode coefficients r_k/r_1 as a function of dimensionless pump parameter K for the nearly factorized case of $1/\Delta_1 = 2.198, 1/\Delta_2 = -2.198$ (Adapted from Ref.[49]). | 83 |
| 4.9 | Mode number M as a function of pump parameter K for the cases shown in Fig.4.4 (orange, (a)) and Fig.4.7 (blue, (b)). The dashed line corresponds to $M = 1$ (Adapted from Ref.[49]). | 85 |

| | | |
|-----|---|-----|
| 5.1 | Reconstruction of a typical joint spectral density, shared by the SPDC and its counterpart stimulated emission process for the same nonlinear crystal at the same pump configuration. A narrow-band seed laser beam at frequency ω_{10} stimulates the emission of a spectrally pre-conditioned coherent output beam in the idler mode. This spectrum is proportional to the joint spectral density with the signal frequency being ω_{10} (Eq.(5.2)). The joint spectral density can be obtained by sweeping the frequency of the seed beam. | 91 |
| 5.2 | The joint spectral density for PPKTP obtained by theoretical calculation | 95 |
| 5.3 | The spectrum of the femtosecond Ti:Sapphire laser measured with OSA. The central wavelength of the pulse spectrum is around 810 nm. The bandwidth of the pulse beam is around 6.5 nm. | 97 |
| 5.4 | A schematic diagram for the first stage of the experiment. DBS: dichroic beam splitter. PBS: polarized beam splitter. ECDL: external-cavity diode laser. FM: flipper mirror. LA: lock-in amplifier. ISO: optical isolator. LF: optical longpass filter. | 98 |
| 5.5 | A schematic diagram for the second stage of the experiment. DBS: dichroic beam splitter. PBS: polarized beam splitter. ECDL: external-cavity diode laser. FM: flipper mirror. LA: lock-in amplifier. ISO: optical isolator. OSA: optical spectrum analyzer | 99 |
| 5.6 | A photograph of the experimental setup taken from above the optical table. . . | 100 |
| 5.7 | Experimental joint spectral intensity (normalized with the peak value) obtained by stimulated emission based measurements. The spectrum of the stimulated output is measured with an optical detector and lock-in amplifier. measurements | 101 |
| 5.8 | Experimental joint spectral intensity (normalized with the peak value) obtained by stimulated emission based measurements. The spectrum of the stimulated output is measured with OSA. | 102 |
| 5.9 | The spectrum of the stimulated output measured with OSA when the wavelength of the seed beam is 809 nm. | 103 |
| 6.1 | Schematics for the continuous-variable quantum state teleportation with a parametric amplifier (PA, inset) in place of a beam splitter (BS) (Adapted from Ref.[65]). NOPA: non-degenerate optical parametric amplifier; HD: homodyne detection; LO: local oscillator. | 108 |
| 6.2 | Fidelity F as a function of detection loss in the teleportation scheme with a BS for a coherent state $ \alpha\rangle$ with $\alpha = 3 + 3j$ (dashed line) and Fock states of $N = 1, 3, 5$ (Adapted from Ref.[65]). | 116 |

| | | |
|-----|--|-----|
| 6.3 | Three-dimensional plot of fidelity F as a function of transmission η (opposite of loss) and gain parameter $R(G \equiv \cosh R)$ of the PA used in Bell measurement for teleportation of the coherent state $ \alpha\rangle$ with $\alpha = 3 + 3j$ (Adapted from Ref.[65]). The light curve at $R = 0$ corresponds to the case of using a beam splitter for the Bell measurement (the dashed line in Fig.6.2). | 118 |
| 6.4 | Fidelity F as a function of gain of PA at a loss of $\eta = 0.7$ for Fock state $ N\rangle$ with $N = 1, 5, 10$. The dashed lines are for the BS scheme (Adapted from Ref.[65]). . . | 119 |
| 6.5 | Fidelity F as a function of transmission η for Fock state $ N\rangle$ with $N = 5$ at gain of $R = 1, 2, 3$ ($G = 1.54, 3.76, 10.07$) for the PA-assisted scheme. The case of BS scheme is plotted as the dashed line for comparison (Adapted from Ref.[65]). . . | 121 |
| 6.6 | Entanglement fidelity F_e as a function of transmission η for a thermal state (one field of the EPR-entangled two-mode squeezed state) with average photon number $\bar{n} = \sinh^2(-1) = 1.38$ for the PA-assisted scheme with gain parameters of $R = 1, 2, 3$ (solid) and for the BS scheme (dashed) (Adapted from Ref.[65]). . . | 124 |
| 6.7 | Normalized inseparability $I_s/I_s^{(0)}$ ($I_s^{(0)} = 4$ for vacuum) in log-scale as a function of transmission η for the EPR-entangled state with initial input $I_s^{EPR}/I_s^{(0)} = 0.135 = -8.69$ dB for various gain parameters of $R = 1, 2, 3$ for the PA-assisted scheme (solid) and the BS scheme (dashed). The light black line at 0 dB is the threshold for entanglement (Adapted from Ref.[65]). | 126 |

ABSTRACT

Field-orthogonal temporal mode analysis of optical fields was recently developed to form a new framework of quantum information science. But so far, the exact profiles of the temporal modes are not known, which makes it difficult to achieve mode selection and de-multiplexing. A novel feedback-iteration method which, combined with the stimulated emission method, can give rise to the exact forms of the temporal mode structure of pulse-pumped spontaneous parametric processes both for high gain parametric process, which gives rise to quantum entanglement in continuous variables, and for the low gain case, which produces a two-photon entangled state for discrete variables.

For the temporal mode analysis in high gain situations, the common treatment of parametric interaction Hamiltonian does not consider the issue of time ordering problem of interaction Hamiltonian and thus leads to the inaccurate conclusion that the mode structure and the temporal mode functions do not change as the gain increases. We use an approach that is usually employed for treating nonlinear interferometers and avoids the time ordering issue. This allows us to derive an evolution equation in differential-integral form. Numerical solutions for high gain situations indicate a gain-dependent mode structure that has its mode distributions changed and mode functions broadened as the gain increases. This will enable us to have a complete picture of the mode structure of parametric processes and produce high quality quantum sources for a variety of applications of quantum technology.

To verify the feedback-iteration method which measures temporal mode structure directly, we measure the joint spectral density of photon pairs produced with the spontaneous parametric down-conversion process of a pulse-pumped PPKTP crystal. The measurement method is based on a stimulated emission process which significantly improves the measurement time and accuracy compared with old spectrally resolved photon coincidence measurement. With the measured joint spectral density, the amplitude of the temporal modes can be obtained with the mathematical tool of singular value decomposition and compared with those measured directly with the feedback-iteration method.

Because the parametric amplifier is in essence a linear four-port device, it couples and linearly mixes two inputs before amplifying and sending them to two output ports. We

show that for quadrature phase amplitudes, a parametric amplifier can replace beam splitters to play the role of mixer. We apply this idea to a continuous-variable quantum state teleportation scheme in which a parametric amplifier replaces a beam splitter in the Bell measurement. We show that this scheme is loss-tolerant in the Bell measurement process and thus demonstrate the advantage of parametric amplifiers over beam splitter in the applications in quantum measurement.

1. INTRODUCTION

It has been around thirty years since the field of quantum information science (QIS) arose [1]. A lot of developments have been achieved after that. It has shown promising future applications in many fields such as quantum computing, quantum simulation, quantum communication and quantum metrology [2].

The quantum computer holds the promises to deliver a huge leap forward in computation to solve certain types of problems that today's most powerful supercomputers cannot solve, for example, encrypting data or simulating chemical reactions, by taking the advantage of the quantum mechanical concepts such as superposition and entanglement [3]. It requires a quantum internet to share quantum information between different quantum computers in a secure way, with quantum cryptography which utilizes the techniques of quantum teleportation and quantum key distribution. Although the quantum computation is generally implemented in atoms, which facilitate the implementation of stationary logical processors and quantum memories, the photons are usually used to carry fragile quantum information in transmission of the quantum network [4], [5], because of their nature of weak interaction with the environment which means low decoherence during the transmission. Any electromagnetic field, no matter what state (quantum or classical) it is in, is first characterized by its modes, which are a special class of solutions to the Maxwell equation [6]. There are four degrees of freedom (DOF) for electromagnetic field corresponding to four DOF of the modes: these are the helicity and the three components of the momentum vector. In a beam-like geometry these may be stated as polarization mode, transverse modes (encompassing two DOFs), and temporal mode (TM). In the QIS, the modes of the electromagnetic field are used to encode quantum information. Polarization is most widely used to encode information and the transverse mode has also been investigated as a basis of encoding information. It was only until recently TM was exploited as the basis for quantum information encoding and a complete tool kit for the TM QIS framework was proposed by [7]. Compared with the polarization mode and transverse modes, TM shows its own advantages. For example, the polarization modes span merely two dimensional Hilbert space, while TMs span an infinite dimensional Hilbert space. The transverse spatial mode is sensitive to medium perturbation

(such as turbulence, which affects the free space propagation) and is inherently incompatible with the existing single-mode fiber network because the information is encoded in different spatial modes. Those drawbacks can be avoided by TM.

Pulse-pumped spontaneous parametric down-conversion, because of precise timing provided by the ultra-short pump pulses [8], [9], have wide applications in QIS such as time-bin entanglement, quantum multi-photon interference of independent sources, heralded single-photon sources. In the tool kit of the TM QIS framework, spontaneous parametric down-conversion (SPDC) serves as the source of generating fields with a rich intrinsic TM structure. This structure is decoupled from the transverse spatial modes and polarization mode, and is encoded in the complicated spectral correlation in frequency domain, as the so-called joint spectrum function, due to the broad bandwidth of the pump field and strict phase matching condition in highly dispersive nonlinear medium. The issue of the complicated spectral correlation can be solved in the time domain, fortunately. Law et al. first made a Schmidt decomposition of the joint spectrum function and found that the generated two-entangled field can be decomposed into a superposition of independent pairs of TMs [7]. This method significantly simplifies the quantum description for the two entangled fields, leading to multi-dimensional temporal quantum entanglement. Moreover, a quantum pulse gate (QPG) technique through nonlinear interaction processes was developed to distinguish and coherently manipulate TM, which completes the tool kit of the TM QIS framework. [10]–[14].

On the other hand, the specific mode functions of the TMs are only revealed by theoretical simulations through the joint spectrum function of parametric processes [7], [15]–[17]. Although they can be indirectly obtained through singular value decomposition when the joint spectrum function is measured [18], they have never been measured directly. It gives rise to a requirement of an exact measurement of TM mode structure in the experiment to provide information for TM-related measurement and manipulation. For example, the mode-matched homodyne detection of the quantum fields which reveals the quantum entanglement in continuous variables is only allowed with the knowledge of the temporal profiles of the TMs [19]. The implementation of the QPGs in TM selection and de-multiplexing also requires the information of the TM. It should be pointed out that because of the two

different measurement techniques for the continuous and discrete variables of the quantum fields, the SPDC source needs to be operated in both the relatively high and low gain regime. As we show in Chapter 4, the mode structure changes with the gain. Therefore, the direct measurement of mode structure in the experiment should be different for the two cases.

In the previous study the issue of time ordering was usually ignored in the treatment of parametric interaction Hamiltonian [15]. This treatment only works in the limit of low gain or in the regime of spontaneous emission but fails at high gain because the ignorance of time ordering of the Hamiltonian will lead to significant error of the result in the high gain limit [20] and will get a wrong TM profile. Because the measurement of the quantum field relies on the homodyne measurement technique in which the mode match between the local oscillator field (LO) and the quantum field is paramount, the mode mismatch caused by the error of the TM profile leads to losses and introduces extra vacuum noise. Obtaining a correct TM profile is also critical for QPG [10], [11], [13] in TM multiplexing. We will investigate the pulse-pumped single-pass parametric processes at arbitrary pumping power. We will use an operator input-output approach to avoid the time ordering issue of the interaction Hamiltonian and allow us to derive a set of coupled operator evolution equations in differential-integral form. We solve them numerically and analyze the mode structure and mode functions at the final output ports as a function of the pump parameter. It is further discussed the modification of the feedback-iteration method to suit SPDC at arbitrary pumping power.

As mentioned above, the TM structure of the SPDC can be derived with the mathematical tool, singular value decomposition once the joint spectrum function is measured. Although the joint spectrum function is able to be measured, the normalized magnitude of joint spectrum function, joint spectral density is often measured in the laboratory insteadly for it is much easier to achieve. To date, JSD has been obtained by performing spectrally resolved single photon coincidence measurements [21]–[23]. The measurement relies on the single-photon detection, which requires very low power of the pumping laser and the photon generation probability much less than unity. This leads to the measurement being very time-consuming because a large number of measurements have to be performed to get the whole JSD. This unavoidably introduces the error for the frequency drift of the pump laser

in a long time duration, and results in low resolution. Recently the relation of the SPDC and its simulated process counterpart has been utilized. Due to the fact that SPDC and stimulated emission share the same phase match relation and pump beam spectrum, the JSD of the spontaneous process can be measured through the corresponding simulated process by a narrow-band seed laser beam [24], [25]. The stimulated emission will significantly increase the output field intensity, which allows the replacement of the single photon detection with a spectrometer in the detection, therefore reducing the integration time. With the aim to compare the indirect measurement of TM with the direct feedback-iteration measurement method, we will investigate the measurement of the JSD for a SPDC process of the nonlinear crystal PPKTP (Periodically Poled KTP) with a narrow-band seed laser beam to stimulate the emission.

Quantum teleportation provides a novel opportunity for communicating quantum information securely other than quantum cryptography (Their combination may further prompt the security of data transformation). When quantum information (qubit) is teleported between two locations, it is transferred through two channels. One is a classical communication channel and the other is a quantum channel. Only when the information from the two channels are received, the receiver can retrieve the original information. Combining this with the no-cloning theorem of quantum mechanics, which states that it is impossible to create an identical copy of an arbitrary unknown quantum state, it significantly improves the security of data communication. It is well-known that losses are notorious in degrading quantum effects and are the key obstacle in many protocols of quantum information processing. Detection process often introduces losses due to imperfect coupling and less-than-unit quantum efficiency. Highly efficient detectors are only available for some limited spectrum of the electromagnetic waves. Thus, it has become a major concern in high fidelity quantum communication involving quantum measurement by detection. Quantum state teleportation is one of such quantum communication protocols where a Bell measurement [26], [27] is performed to projectively select out the required states [28]–[31]. For continuous-variable quantum state teleportation, Bell measurement is usually achieved by homodyne detection, which is sensitive to losses. This will inevitably affect the fidelity of the teleported state. On the other hand, amplification is known to overcome the effect of losses. In essence, a PA is

a four-port linear device just like a beam splitter which makes it possible to replace beam splitter (BS) in many situations to play the role of mixer while amplifying the input fields. We will investigate the feasibility of replacing a beam splitter by a parametric amplifier for Bell measurement in the quantum teleportation scheme and demonstrate the loss tolerant property of the new scheme.

The thesis is organized as follows:

In the chapter “Quantum and Nonlinear Optics,” a general knowledge of quantum optics, nonlinear optics and relevant topics are introduced. The important role optical mode plays in quantum optics is explained. The TM is highlighted in the explanation. The two types (continuous and discrete dimension) of Hilbert space, the quantum optical state spanned corresponding to two different measurement methods in quantum optics, are discussed. The classical and quantum theory of nonlinear optics is given. The nonlinear process SPDC is explained with the introduction of the joint spectrum function. Phase match and quasi-phase match conditions are analyzed.

In the chapter “Measurement of TM Structure of Entangled Fields in Continuous and Discrete Variables,” we propose a direct TM structure measurement, feedback-iteration method, of entangled fields for both high gain and low gain PAs. The simulation results are analyzed. In the chapter “Mode Structure of a Broadband High Gain Parametric Amplifier,” Time-ordering issue of interaction Hamiltonian for parametric processes in the high gain regime is further discussed. In the chapter “Measurement of JSD,” an experiment of fast and highly resolved capture of the JSD of photon pairs is described. In the chapter “PA for Bell Measurement in Continuous-Variable Quantum State Teleportation,” we propose a new continuous-variable quantum state teleportation scheme in which a PA replaces a beam splitter in Bell measurement, and demonstrates its feasibility. The loss-tolerant property of the new scheme will be discussed on the transmission of a coherent state, Fock states, and Einstein, Podolsky and Rosen (EPR) entangled state [32]. It is followed by the chapter ”summary” with conclusion and further discussion.

2. QUANTUM AND NONLINEAR OPTICS

2.1 Background Knowledge of Quantum Optics

Quantum optics is a study of how individual quanta of light, known as photons, interact with atoms and molecules. The initial motivation to quantize the light is that the classical optics can not explain the phenomenon of spontaneous emission. The photoelectric effect was further evidence of this quantization as explained by Albert Einstein. The later study found some quantum states of light giving rise to the phenomenon also could not be described by classical electromagnetism. For example, single photon state, entangled state, and squeezed state. Quantum optics actually refers to the second quantization of light. The first quantization is already involved in the Maxwell equations (we use the cgs unit system, in which the electric field and magnetic field have the same unit and the Maxwell equations are symmetric with respect to these two quantities in the free space).

$$\begin{aligned}\nabla \cdot \mathbf{E} &= 4\pi\rho \\ \nabla \cdot \mathbf{B} &= 0 \\ \nabla \times \mathbf{E} &= -\frac{1}{c} \frac{\partial \mathbf{B}}{\partial t} \\ \nabla \times \mathbf{B} &= \frac{1}{c} \left(\frac{\partial \mathbf{E}}{\partial t} + 4\pi\mathbf{J} \right).\end{aligned}\tag{2.1}$$

This can be seen from the comparison of the Lagrangian of the scalar Klein Gordon field

$$\mathcal{L} = \frac{1}{2} \partial_\mu \partial^\mu \varphi - \frac{1}{2} m^2 \varphi^2\tag{2.2}$$

for massive particles and the electromagnetic vector potential field

$$\mathcal{L} = -\frac{1}{4} F_{\mu\nu} F^{\mu\nu},\tag{2.3}$$

for photons, where $F^{\mu\nu} = \partial^\mu A^\nu - \partial^\nu A^\mu$ and $A^{\mu,\nu}$ is the component of four dimensional electromagnetic vector potential $\mathbf{A}' = (\varphi, \mathbf{A})$. The relation of the electric and magnetic fields with the scalar and the three dimensional vector potential φ, \mathbf{A} is given by

$$\mathbf{E} = -\frac{1}{c} \frac{\partial \mathbf{A}}{\partial t} - \nabla \varphi, \quad \mathbf{B} = \nabla \times \mathbf{A}. \quad (2.4)$$

From the Lagrangian of the Klein Gordon field Eq.(2.2) it derives the Klein Gordon equation

$$\partial_\mu \partial^\mu \varphi + m^2 \varphi = 0, \quad (2.5)$$

which is the relativistic version of Schrödinger's equation. And from the Lagrangian of the four dimensional vector field Eq.(2.3) it derives the electromagnetic vector potential version of the Maxwell equation in free space.

$$\partial_\mu \partial^\mu \mathbf{A}' = 0. \quad (2.6)$$

From Eq.(2.5) we can see if we substitute the quantum operator of momentum $\hat{\mathbf{P}} = -i\hbar\nabla$ and energy $\hat{E} = i\hbar\partial_t$ to the energy-momentum relation of special relativity $\mathbf{P}^2 - E^2 + m^2 = 0$, we can derive the Klein Gordon equation. It is the same as the way we quantize the equation of classical energy-momentum relation $E = \mathbf{P}^2/2m + V$ and obtain the Schrödinger's equation.

$$i\hbar\partial_t\varphi = \left(-\frac{\hbar^2}{2m}\nabla^2 + V\right)\varphi. \quad (2.7)$$

Therefore the solution of the Klein Gordon equation is the quantum wave field due to the first quantization. In the same way, the classic electromagnetic wave field is the solution of the Maxwell equation due to the first quantization.

The solution of the Maxwell equations is given by.

$$\begin{aligned} \mathbf{E}(r, t) &= \sum_{\omega} i\sqrt{2\pi\hbar\omega} \mathbf{A}_k(r) \alpha(\omega) e^{-i\omega t} + h.c. \\ \mathbf{B}(r, t) &= \sum_{\omega} \sqrt{\frac{2\pi c^2 \hbar}{\omega}} \nabla \times \mathbf{A}_k(r) \alpha(\omega) e^{-i\omega t} + h.c. \end{aligned} \quad (2.8)$$

Here, *h.c.* stands for Hermitian conjugate, and $\int d^3r \mathbf{A}_k^*(r) \cdot \mathbf{A}_{k'}(r) = \delta_{k,k'}$ represents the normalized orthogonal spatial distribution of the field. The second quantization can be achieved by just replacing the complex amplitude $\alpha(\omega)$ with the annihilation operator $\hat{a}(\omega)$. Of course the derivation process of the quantization is a little bit more complicated. Let $Q_\omega = \sqrt{\hbar/2\omega}[\alpha(\omega) + \alpha^*(\omega)]$ and $P_\omega = \sqrt{\omega\hbar/2}[\alpha(\omega) - \alpha^*(\omega)]/i$, and substitute Eq.(2.8) to the Hamiltonian of the electromagnetic field $H = (1/8\pi) \int d^3r (E \cdot E + B \cdot B)$ and will get an expression in the same form of the harmonic oscillation, and then quantize it with the same method of the harmonic oscillator. We will have

$$\hat{H} = \sum_{\omega} (\hat{a}^\dagger \hat{a} + \frac{1}{2}) \hbar\omega = \sum_{\omega} \left(\hat{n} + \frac{1}{2} \right) \hbar\omega \quad (2.9)$$

Here the creation and annihilation operator \hat{a} , \hat{a}^\dagger and the number operator \hat{n} all refer to the functions of the variable ω . Actually the wavefunction of other matters can be second quantized in the same way. All the results and conclusions we got from the harmonic oscillator can be applied here too. The number operator \hat{n} which is equal to $\hat{a}^\dagger \hat{a}$ is a measure of how many quanta of photons there are in the field. And the total energy is the total number multiplied by the energy of each photon $\hbar\omega$. In the first quantization, the particle is a field of waves, the classical variables such as position and momentum should be quantized to some quantum states, so that the field is a probability distribution of the particle over these states. In the second quantization, the field itself (total energy) has to be quantized too. And the quantized field includes the probability distribution over the states of the first quantization variables, such as position and momentum, and the probability distribution of the states of the second quantization variables: particle number.

We define a quadrature amplitude operator $\hat{X} = \hat{a} + \hat{a}^\dagger$ and a quadrature phase operator $\hat{Y} = (\hat{a} - \hat{a}^\dagger)/i$. By comparing with the quantum theory of harmonic oscillators, we can see they are just a factor different from the position operator \hat{x} and momentum operator \hat{p} . But we should notice here they are not related to the real position and momentum operators which belong to the concept of the first quantization, but related to the real and imaginary part of the complex amplitude of the electromagnetic field. But comparing them with the position and momentum quantities in the harmonic oscillator can help us have a deeper understanding

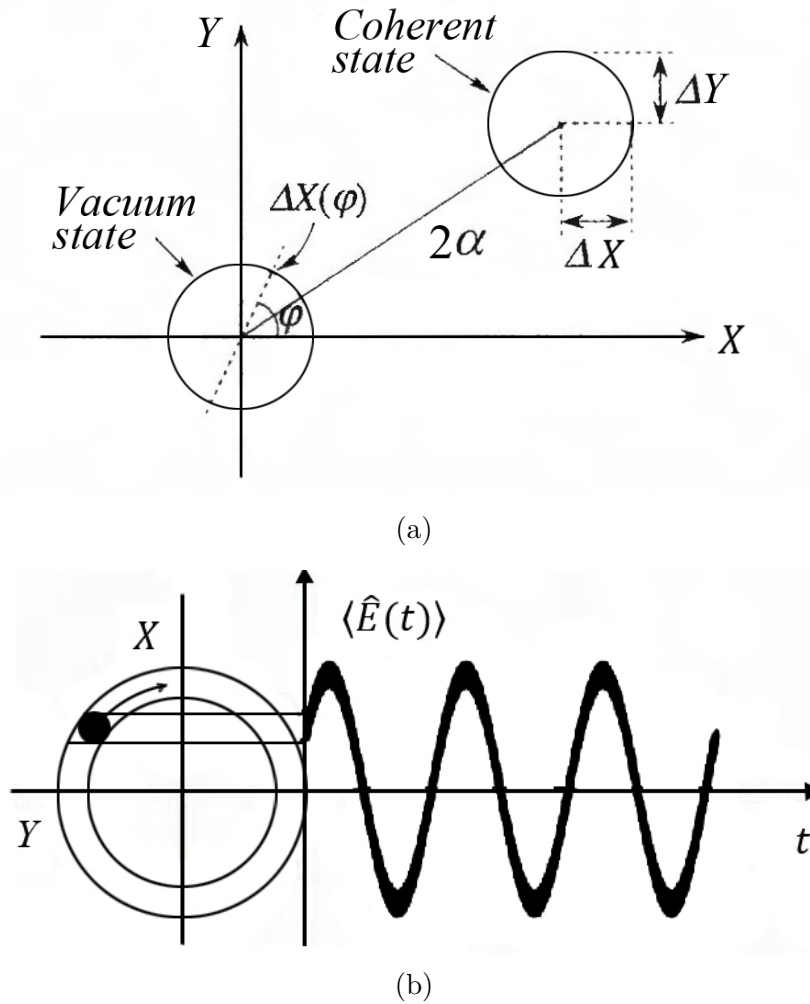


Figure 2.1. (a) Phase-space portrait of the coherent state with the Wigner function. (b) The coherent state revolves about the origin in Phase-space and projected onto the $X - t$ space

of the physical meaning behind those quantities. And if we ignore the factors and units, they can even be used to simulate the position and momentum in the first quantization due to the same mathematical formation. For example, the Einstein, Podolsky and Rosen state which describes two particles spatially separated by x_0 but perfectly correlated in both position and momentum. It can be expressed in $x - p$ phase space with Wigner function (which was introduced [33] by Eugene Wigner in 1932 to study quantum corrections to classical statistical mechanics. Due to the uncertainty principle, the concept of probability distribution of x and p in the phase space for a classical particle fails for a quantum particle. But the

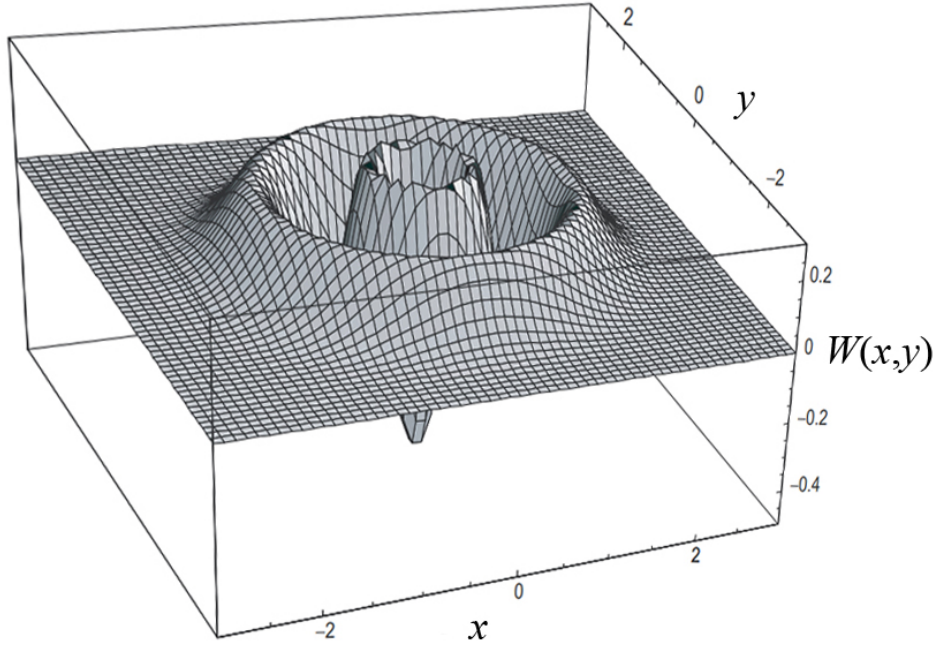


Figure 2.2. Wigner function for a number state $|n\rangle$.

quasiprobability Wigner distribution plays an analogous role. By smoothing the Wigner distribution with the resolution larger than \hbar , we can obtain the semi-classical probability distribution.) [34]: $\delta(x_1 - x_2 + x_0)\delta(p_1 + p_2)$. The EPR state can be simulated by the outputs of a nondegenerate optical parametric amplifier (NOPA) which possess the same correlation properties of the EPR state except that the two particles are replaced by the virtual harmonic oscillators and the position and momentum of the particles by the quadrature amplitude and phase. A classical object should have no quantum fluctuation of the position and momentum, and the two quantities can be measured at the same time. The quantum state most close to a classical object is the coherent state. It is the eigenstate of the annihilation operator $\hat{a}|\alpha\rangle = \alpha|\alpha\rangle$ Here \hat{a} is not Hermitian operator, so α is a complex number. For a coherent state the fluctuation of X and Y are minimal, equal to unity. Fig.2.1(a) is a coherent state represented in the $X - Y$ phase space. It is a disc in the plane with the radius equal to unity representing the fluctuation $\langle \Delta^2 \hat{X} \rangle = \langle \Delta^2 \hat{Y} \rangle = 1$. As the time going, the disc will rotate about the original point. In a $X - t$ coordination, it describes a wave as shown in

Fig.2.1(b). This is the same with harmonic oscillation. In the experiment, the laser beam state is the coherent state. Because it is the state most close to a classical object, the Schrödinger's cat state can be expressed as a coherent combination of two coherent states. $|\varphi\rangle_{cat} = \mathfrak{N}(|\alpha\rangle + e^{i\theta}|\beta\rangle)$. By contrast, the number state is the eigenstate of the number operator $\hat{n}|n\rangle = n|n\rangle$. It is a non-classical state. Fig.2.2 shows the three photons state $|3\rangle$ in the $X - Y$ phase space. As we can see the probability in some areas is negative which shows its non-classical properties. That can not be understood in a classical view. The coherent state can be expanded in the number state space as this

$$|\alpha\rangle = e^{-\frac{|\alpha|^2}{2}} \sum_n \frac{\alpha^n}{\sqrt{n!}} |n\rangle. \quad (2.10)$$

When α is very small, the one photon state $|1\rangle$ will dominate in probability besides the vacuum state $|0\rangle$. Therefore in the experiment we usually put some attenuators in the laser beam path to reduce the laser intensity to obtain a small number photon state or even single photon state when we need to do the experiment at the photon counting level.

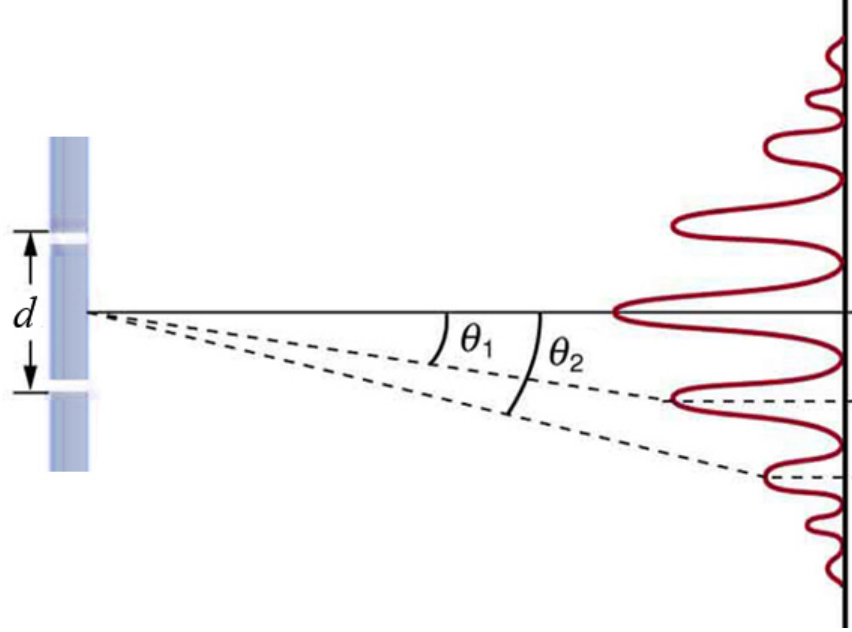
2.1.1 Optical Modes

Let's get back to the first and second quantization. So how do we connect the first quantization and the second quantization? We can understand them in a way that the linear independent wave function solutions of the first quantization equations (Maxwell equations for the electromagnetic field), are like sets of houses. We call these houses modes. For each house there is a harmonic oscillator living inside. Each quanta of energy of the harmonic oscillation corresponds to one photon. In quantum field theory one particle is equivalent to one quanta of energy since the energy of one particle is equal to $\hbar\omega$. Here there is an important property. Just like two quanta of energy of a harmonic oscillator can not be distinguished, two particles in the same mode are indistinguishable. Notice the indistinguishability is born in the process of the second quantization, the precondition that they are in the same mode is important for the two particles to be indistinguishable. If the two particles are in two orthogonal modes, they are totally distinguishable. If they are in two modes which partially overlap, the two particles are partially indistinguishable.

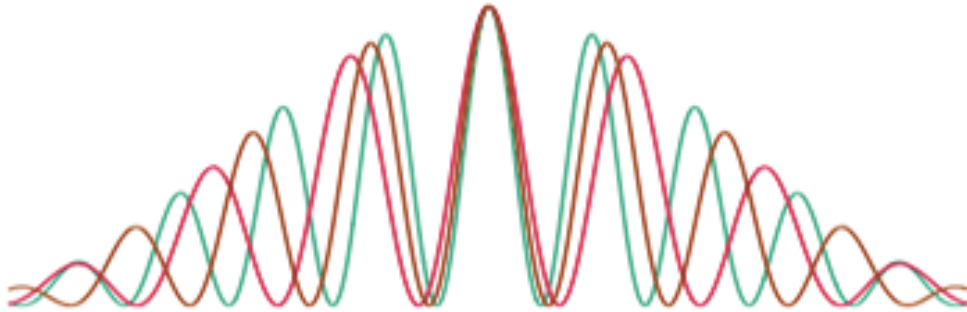
Also notice there are no position and momentum variables in the second quantization process. Therefore the quantum photon is not localized. The probability to find the photon at some position and time is determined by the first quantization wave solution. For a pulsed wave, for example, the probability distribution is confined in the pulse shaped wave. For a continuous-wave (CW) light, on the other hand, the light source is operated continuously, not pulsed. The probability is the same everywhere, so the detection of the photon at some position and time is fully uncertain.

Since modes are a set of linear independent solutions of the first quantization equations with the boundary condition, they span a linear space. An arbitrary field can be written as a linear combination of each mode. The modes also represent the degree of freedom of the field. Electromagnetic fields have four DOFs. Three spatial modes in different dimensions and the polarization mode which is related to the spin of the photon. In a waveguide fiber we are familiar with the three dimensional spatial modes. Two dimensions perpendicular to the propagation path are called transverse mode. One dimension spatial mode along the propagation direction is called longitudinal mode. In a beam-like geometry, the momentum of the longitudinal mode is related to the frequency by the medium dispersion relation $k(\omega)$. One momentum corresponds to one frequency component. So the longitudinal mode is equivalently understood as the temporal mode. Frequency is a better parameter than the longitudinal momentum to label the mode because it is fixed in all material while momentum changes in different materials. A simple example can give us a basic understanding is Young's two-slit interference experiment. In the experiment, if the light source is monochromatic light, namely light with single frequency, the visibility of the interference pattern is highest, as shown in Fig.2.3(a). If we use a broadband light source such as white light, the visibility of the interference pattern will reduce, as shown Fig.2.3(b). That is because the light of the same frequency interferes with itself. The interference pattern of different frequencies overlaps, which reduces the visibility.

Modifying Young's two-slit interference experiment to a quantum version, we can use the single photon as a light source and repeat the experiment for many times, we will still obtain the interference pattern. From the quantum version of Young's two-slit interference experiment, Dirac obtained the conclusion: Each photon interferes only with itself. However, the



(a)



(b)

Figure 2.3. (a) Young's double slit experiment. The pure-wavelength light sent through two slits is diffracted into a fringes pattern. (b) The visibility of the interference pattern of double slit experiment reduces for broadband light source

later research shows two photons can also interfere if they can not be distinguished. From the previous discussion we know that only the photons in the same mode are indistinguishable. Therefore the optical coherence is related to the indistinguishability and modes of the photons. In the QIS, modes are used to encode information. In early work, the polarization modes are often used to encode the information. The information is encoded in the coherent phase of the state: $(|\uparrow\rangle + e^{i\theta} |\downarrow\rangle)/\sqrt{2}$. However polarizations span a only two dimensional

Hilbert space. TM can offer an infinite dimensional basis because of the infinite number of frequencies or momentum for a given boundary condition. Therefore more information is allowed to be encoded on. Besides that, in a quantum network or multi photon interference experiment, photons from different sources are required to interface with each other, which requires the indistinguishability between photons, thus they have to be shaped in the same modes.

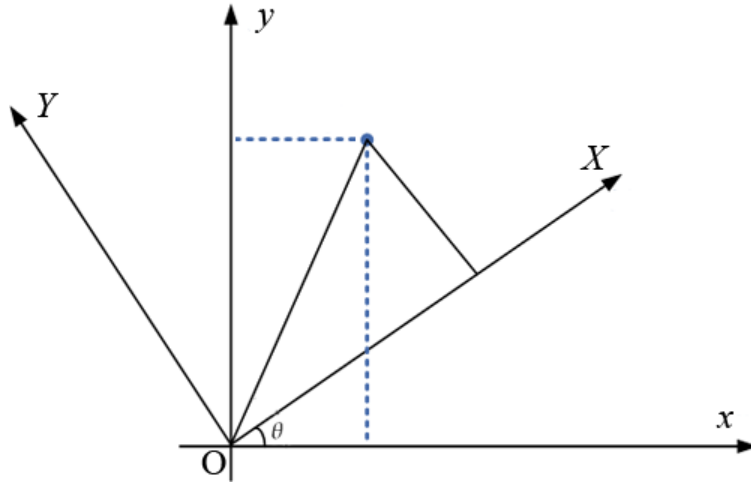


Figure 2.4. Two dimensional Cartesian coordinate system has the basis of x, y axis. The linear combination of the original basis $X = x\cos\theta + y\sin\theta, Y = -x\sin\theta + y\cos\theta$ is also a basis.

From Young's two-slit experiment we can see that each frequency can be treated as a mode. Just like the two dimensional Cartesian coordinate system, the x, y axes can be treated as the basis, but if we rotate the coordination, we can get another basis with the basis vectors being a linear combination of the original basis vectors, as shown in Fig.2.4. The TM is not unique, either. There are infinite choices of linear combinations of the frequency modes. Notice that In quantum mechanics, the eigenstates of the position operator \hat{x} form an infinite dimension space. The eigenfunction is $\delta(x - x')$. We can call it the position state. This is different from the Cartesian coordinate system. The concept is a little bit similar to the first and second quantization. x, y form a two dimensional space in the Cartesian coordinate system, and x, y are the basis vectors. But for each one dimension position x, y themselves, they are the infinite dimension space, with the basis vector being the position

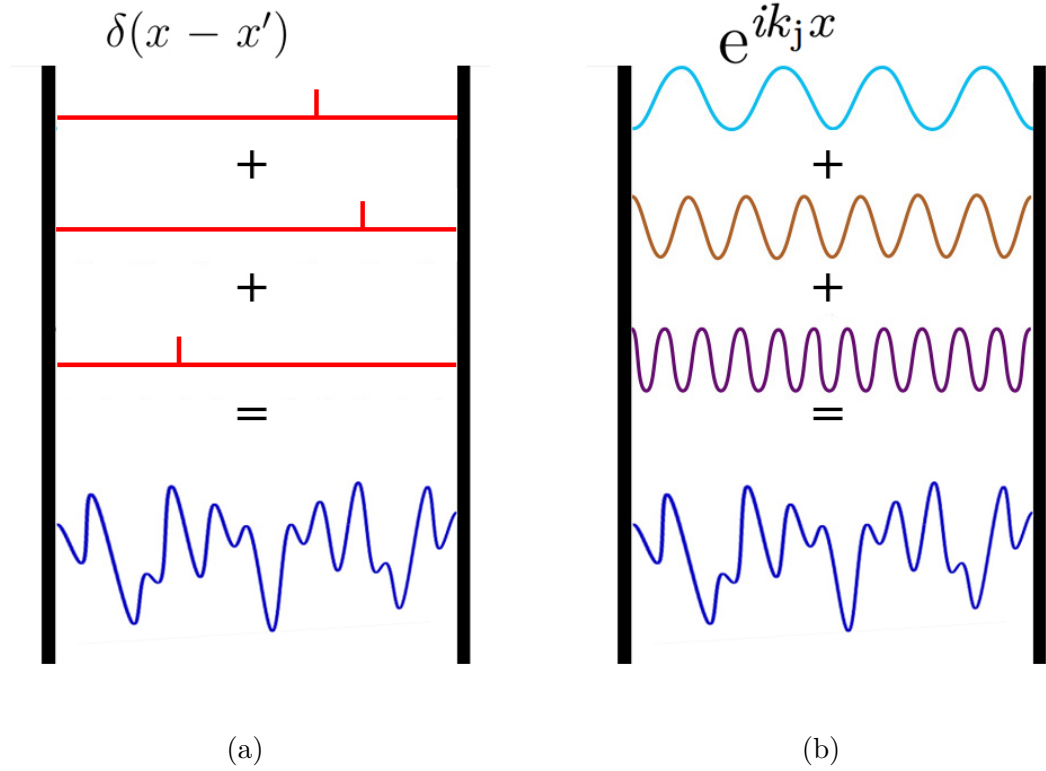


Figure 2.5. (a) Arbitrary function can be expanded in an infinite dimensional space with the basis vector of $\delta(x - x')$. The index for the basis vector is x'
 (b) The function can be expanded with the new basis of Fourier transform functions $e^{ik_j x}$, too. The index of the basis vector is k_j

state, $\delta(x - x')$ or $\delta(y - y')$. So any arbitrary function can be expanded in the position state $f(x) = \int dx' f(x') \delta(x - x')$ as shown in Fig.2.5(a). But we can also choose another basis with the basis vectors being a linear combination of the position states, such as the Fourier transform term, $e^{ik_j x}$, that the function can be expanded in this basis in the same space too: $f(x) = \sum_j A_j e^{ik_j x}$, as shown in Fig.2.5(b). In the position state, the index of the state is x' . In the Fourier function $e^{ik_j x}$, the index of the state is the momentum k_j . It is the same for the frequency mode too. We can write the annihilation operator in the frequency mode as $\hat{a}(\omega)$, which can be also understood to be expanded in the frequency state basis as $\hat{a}(\omega) = \int d\omega' \delta(\omega - \omega') \hat{a}(\omega')$. If we choose the Fourier function form combination of the frequency, $e^{i\omega t}$, we got the annihilation operator $\hat{a}(t) = \int \frac{d\omega}{2\pi} e^{-i\omega t} \hat{a}(\omega)$. Now time t is the index of the new basis, this is just the annihilation operator in the time domain. Besides these two

choices, we can choose any linear combination of the frequency $A(\omega)$ (an example given in Fig.2.6) as long as the basis vectors are chosen orthogonal to each other. Being orthogonal means the inner product of the different basis vectors is zero. Here the inner product is defined as the integral of $\int d\omega A_k^*(\omega)A_{k'}(\omega) = \delta_{k,k'}$. Why is it in this form? Because, in a Cartesian coordinate, we multiply the x, y components of the two vectors, respectively, and then do a summation of them. In the same way, in this infinite dimensional space we multiply the components of the vector at different frequency states ω , respectively, and integrate them. And in a complex space, the inner product is defined by multiplying a vector with the complex conjugate of the second vector.

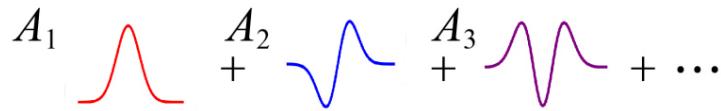


Figure 2.6. The first three mode amplitudes for an example of the TM. Each mode is orthogonal to each other.

2.1.2 Continuous and Discrete Variables

In quantum mechanics, the eigenstates of an Hermitian operator form a Hilbert space. The eigenvalue can be continuous, such as the position and momentum, or discrete, such as the photon number. The momentum in a waveguide is also discrete. In quantum optics the concept is the same. Moreover, they are related to two main techniques of measurement in the quantum optics experiment. The first method is called homodyne detection which use the regular continuous photo-electric detector (Fig.2.7(b)), it amplifies the weak optical field in a way that quantum fluctuation is amplified too, as shown in Fig.2.7(a). So the quantum properties can be measured. It can be used to measure the continuous variable quadrature amplitude and phase, X and Y , their quantum fluctuation and also the correlation of these continuous variables. The second method is called the photon counting technique as shown in Fig.2.7(c). For this method the optical field source has to be prepared to be very weak so that the photons reach the detector one by one separately, and each photon will generate

an electric pulse signal. Using two or more single photon detectors, we can also measure the correlation of the field by connecting them to the logical electrical circuit block, and counting the rate of two electrical pulses arriving at the same time. Therefore the photon counting method is usually used to measure the photon number state and the correlation of the discrete variable such as polarization and photon number. It is more consistent with our intuition that the entanglement of discrete variable (for example, entanglement in the polarization modes) should be measured in a photon counting way, because each photon has to be projected to one of the eigenstates and check the correlation between the different photons. Measuring them in an ensemble average will make the problem more complicated. While the homodyne detection is more unconditional. It can be used to measure a statistical average quantity of all quantum states.

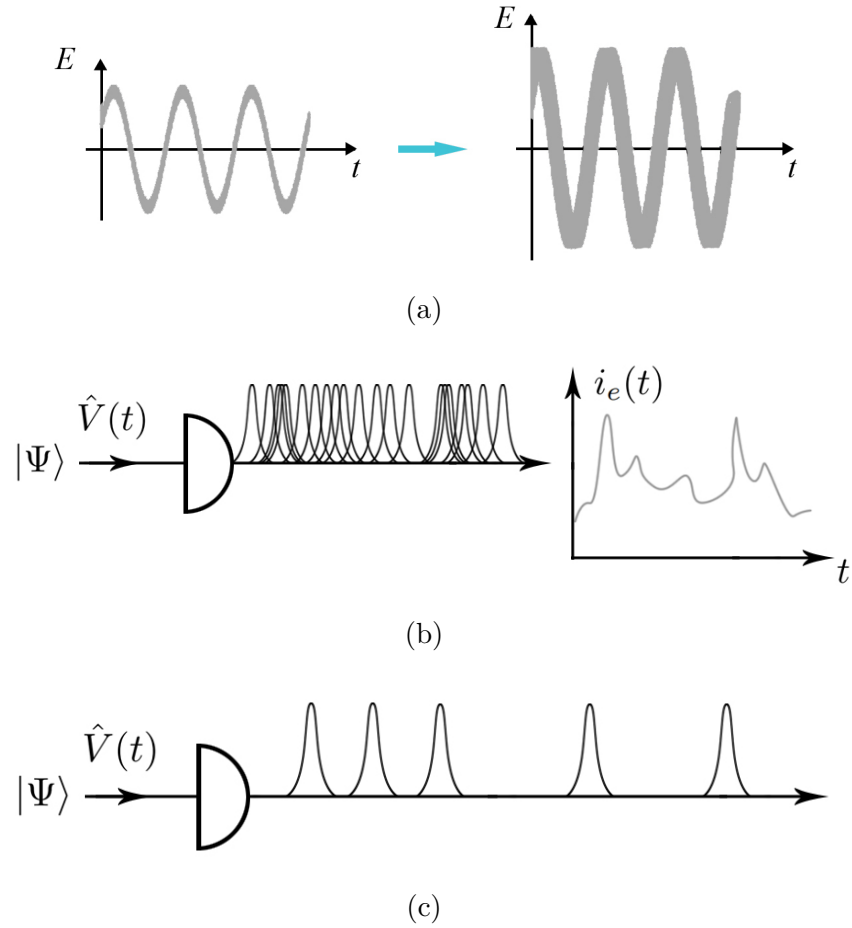


Figure 2.7. (a) The quantum fluctuation is amplified too when the intensity of the field is amplified by the Homodyne detection technique. (b) Continuous photon-current under relatively strong light intensity. (c) Photon counting technique for weak optical fields.

2.2 Nonlinear Optics

In recent decades, nonlinear optics has developed rapidly in the physics field. It is the study of how intense light interacts with matter. In this condition the nonlinear response of the atoms plays an important role. The invention of the laser by Maiman in 1960 plays a key role in the evolution of nonlinear optics. It provides sufficiently high intensive light required to experiment in this field. Franken and coworkers observed the nonlinear optical phenomenon in an experiment with a ruby laser for the first time in 1961 [35]. The red light was frequency doubled into ultraviolet in the process of second harmonic generation. The emergence of pulse lasers provides a chance to obtain more pronounced nonlinear phenomena with a moderate laser power. Since they concentrate light energy temporally, the magnitude of the peak pulse power can be many orders higher than the intensity of the CW laser. Nonlinear optics leads to many applications such as ultrafast pulse laser, optical signal processing, ultrafast switches, laser amplifiers, optical computers, sensors, and many others. The common material used in nonlinear optics today are usually birefringent crystals with large nonlinearities such as BBO, LBO, KTP, ZGP and Quasi-Phase matched Periodic poled material such as PPLN, PPKTP, PPLT.

Nonlinear optics processes can be described with both classical wave theory and quantum optical theory, although some nonlinear effects can only be explained by quantum theory. For example, the process of SPDC which involves spontaneous emission. In this section, we will present both methods.

2.2.1 Classical Wave Theory of Nonlinear Optics

Nonlinear optical effects arise for the nonlinear response of the material in the applied field. In most cases nonlinear magnetization responses can be ignored. We will only consider nonlinear responses of polarization here. In nonlinear medium the electrical polarization \vec{P} is given

$$\mathbf{P} = \epsilon_0[\chi^{(1)} : \mathbf{E} + \chi^{(2)} : \mathbf{E}\mathbf{E} + \chi^{(3)} : \mathbf{E}\mathbf{E}\mathbf{E} + \dots] \quad (2.11)$$

where $\chi^{(n)}$ is $(n + 1)$ th order tensor representing n th order electric susceptibility (Note that for the medium invariant under spatial inversion, the even order susceptibility is zero. The first nonzero nonlinear term is the third order one). To simplify the problem, here we assume the medium response to the applied field instantaneously which means the medium is nondispersive.

From the Maxwell equation in medium, we have

$$\nabla \times \nabla \times \mathbf{E} + \frac{1}{c^2} \frac{\partial^2 \mathbf{E}}{\partial t^2} = -\mu_0 \frac{\partial^2 \mathbf{P}}{\partial t^2}. \quad (2.12)$$

This tells us polarization can work as a source of electrical fields. When polarization oscillates, it will generate a field oscillating with the same frequency. Only consider the second order nonlinear susceptibility, with the applied field being $E(t) = E_0 \cos \omega t$, the nonlinear polarization P_{NL} will be

$$P_{NL}(t) = \epsilon_0 \chi^{(2)} E(t)^2 = \frac{1}{2} \epsilon_0 \chi^{(2)} E_0^2 (1 + \cos 2\omega t). \quad (2.13)$$

As we can see the polarization oscillates with twice the frequency as the applied field. It generates the new field which doubles the frequency of the incident field. This is the second harmonic generation. Now if the applied field includes two components with different frequencies, $E(t) = E_1 \cos \omega_1 t + E_2 \cos \omega_2 t$, the nonlinear polarization is

$$\begin{aligned} P_{NL}(t) = & \frac{1}{2} \epsilon_0 \chi^{(2)} E_1^2 (1 + \cos 2\omega_1 t) + E_2^2 (1 + \cos 2\omega_2 t) \\ & + 2E_1 E_2 [\cos(\omega_1 + \omega_2)t + \cos(\omega_1 - \omega_2)t]. \end{aligned} \quad (2.14)$$

The components of the new field will not only contain the double frequency terms of the initial two components but also the sum and difference of their frequencies. This is the sum and difference generation process, respectively. In the derivation of P_{NL} above, we only consider one dimension and the scalars. The wave transmission in space was also ignored.

2.2.2 Quantum Optical Theory of Nonlinear Optics

The quantum optical theory of nonlinear optics explains nonlinear optics at the level of photon interaction. The nonlinear effect couples the photons in the different frequency modes, by annihilating photons in some frequency modes and creating some other photons in different frequency modes, which can not be achieved in the linear optics. It therefore can generate the entangled states and non-classical states such as squeeze states, which can not be obtained in linear optics.

The quantum theory of nonlinear optics is given as follows (Notice that the recent research shows it is wrong to use electrical fields to quantize in nonlinear optics, we still use the old method in this report. It will lead to an incorrect factor in the nonlinear interaction Hamiltonian [36]. The factor will be corrected by experiment measurement): The energy of electromagnetic field in a non-magnetic medium is given by

$$H = \int \frac{1}{2\mu_0} \mathbf{B}^2(\mathbf{r}, t) d^3r + \int d^3r \int_0^{\mathbf{D}(\vec{r}, t)} \mathbf{E}(\mathbf{r}, t) \cdot d\mathbf{D}(\mathbf{r}, t). \quad (2.15)$$

Here $\mathbf{D}(\mathbf{r}, t)$ is the electric displacement vector which can be expressed in the form

$$\mathbf{D}(\mathbf{r}, t) = \epsilon_0 \mathbf{E}(\mathbf{r}, t) + \mathbf{P}(\mathbf{r}, t). \quad (2.16)$$

Substitute Eq.(2.11) and (2.16) into Eq.(2.15), it can be easily seen the Hamiltonian can be treated as an ordinary term H_0 for electromagnetic field in linear medium plus a nonlinear interaction term given by

$$H_{int} = \sum_{n=2}^{\infty} \int d^3r \frac{n}{n+1} \epsilon_0 \mathbf{E}(\mathbf{r}, t) \cdot \chi^{(n)} : \mathbf{E}(\mathbf{r}, t)^n \quad (2.17)$$

Quantizing the Hamiltonian in linear medium H_0 , we obtain the electrical field with one dimension approximation as

$$\hat{E} = \hat{E}^{(+)} + \hat{E}^{(-)}, \quad (2.18)$$

with

$$[\hat{E}^{(-)}]^\dagger = \hat{E}^{(+)} = \hat{\sigma} \sqrt{\frac{\hbar\omega}{\epsilon}} \int d\omega \hat{a}(\omega) e^{i(k(\omega)z - \omega t)}, \quad (2.19)$$

where $\hat{\sigma}$ is the polarization and ϵ is the permittivity of the linear medium. Using the three-wave mixing (TWM) as example, let $\hat{E} = \hat{E}(\omega_1) + \hat{E}(\omega_2) + \hat{E}(\omega_3)$, and substitute the electrical field operator to the second order nonlinear interaction Hamiltonian

$$H_{int}^{(2)} = \int d^3r \frac{2}{3} \epsilon_0 \mathbf{E}(\mathbf{r}, t) \cdot \chi^{(2)} : \mathbf{E}(\mathbf{r}, t)^2, \quad (2.20)$$

and quantize it, we obtain the general form

$$\frac{1}{i\hbar} \int dt \hat{H}_{int}^{TWM} = \int d\omega_1 d\omega_2 \phi(\omega_1, \omega_2) \hat{a}^\dagger(\omega_1) \hat{a}^\dagger(\omega_2) \hat{a}(\omega_1 + \omega_2) + h.c., \quad (2.21)$$

where we used $\int dt e^{i\omega t} = 2\pi\delta(\omega)$. And

$$\phi(\omega_1, \omega_2) = \zeta \frac{\sin(\Delta KL/2)}{\Delta K} e^{-i\Delta KL/2}, \quad (2.22)$$

where ζ is a constant proportional to the second order susceptibility, L is the length of the medium and $\Delta K = k(\omega_1) + k(\omega_2) - k(\omega_1 + \omega_2)$ is the phase mismatch. More details of the phase matching is explained in the next section. Eq.(2.21) gives the quantum explanation of sum and difference generation processes. The creation and annihilation operators just tell that one photon is annihilated while two photons are created and the reverse process is in the hermitian conjugate term.

2.2.3 Phase Matching Condition

Because nonlinear optics is about the annihilation and creation of photons in different frequency modes, and the process should obey the law of conservation of energy and momentum, there exists an correlation of the energy and momentum between the output photons. The energy and momentum of a photon correspond to the frequency and wavelength in a wave view of optics. And the frequency and wavelength are related to each other by the refractive index of the propagation medium. There are only some specific nonlinear mediums

with the refractive index satisfying the dispersion relationship that will generate significant nonlinear phenomena. This frequency, momentum correlation of the input and output beams refers to the phase matching condition.

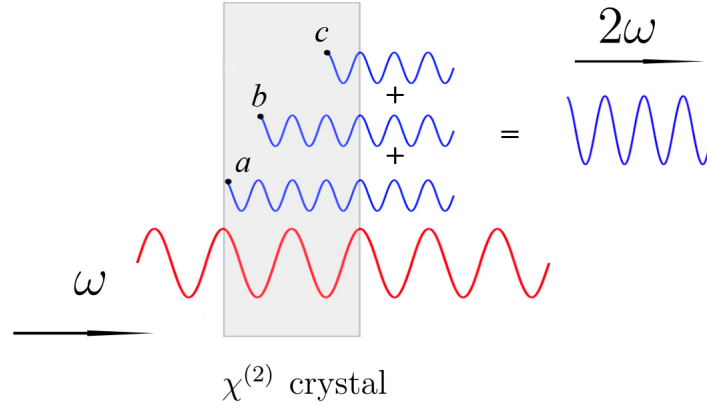


Figure 2.8. The pump field (the red line) at frequency 2ω propagates in a $\chi^{(2)}$ crystal. Second harmonic generated field (the blue line) at frequency 2ω is generated through the medium. When the phase matching condition is satisfied, the waves of generated fields at different locations propagate in phase with each other and amplitudes add constructively.

Phase matching can also be explained by the classical nonlinear optics theory. From Eq.(2.14) we see that double frequency, sum frequency and difference frequency are all generated at the same time. These effects usually can not be generated at the same time for the same nonlinear crystal. Only one of these nonlinear phenomenon will happen when its phase matching condition satisfied. Take the second harmonic generation as example, if its phase matching condition is satisfied, the one of sum frequency and difference frequency generations will not be satisfied, thus only double frequency survives at the output of the crystal. Let $E(t) = E_0 \cos(k(\omega)z - \omega t)$, and only consider the second harmonic oscillation term, the second order nonlinear polarization will be

$$P_{NL}(z, t) = \frac{1}{2} \epsilon_0 \chi^{(2)} E_0^2 [\cos(2k(\omega)z - 2\omega t)] = \frac{1}{2} \epsilon_0 \chi^{(2)} E_0^2 [\cos(k(2\omega)z - 2\omega t)]. \quad (2.23)$$

This shows the generated second harmonic fields in different locations of the crystal have a phase difference $k(2\omega)z$. Only when the relation $k(2\omega) = 2k(\omega)$ is satisfied, the field gener-

ated in different locations will contribute constructively and get amplified as they propagate through the crystal. Otherwise, if the phase matching condition is not satisfied, the generated second harmonics field at different locations will interfere destructively, causing the direction of energy flow between the generated field and the pump field in the crystal to periodically change. In Fig.2.8, it assumes the phase matching condition is satisfied, the second harmonic fields generated in three different locations a, b and c are in phase as they propagate through the crystal. So the intensity of the generated field would increase exponentially. Fig.2.9 shows the intensity of the generated second harmonic field as a function of propagation distance in the crystal. The solid line shows the intensity of the second harmonic generation field when the phase matching condition is satisfied. The dashed line shows the intensity of the generated field oscillates at low amplitude when the phase matching condition is not satisfied (phases mismatched). To satisfy the phase matching condition in the second harmonic generation, $k(2\omega)$ has to be equal to $2k(\omega)$ as in the previous analysis. Most materials have normal dispersion: the refractive index n increases when the frequency of the input field increases, and can not satisfy it. It can be solved with birefringent material, in which the dispersion relation depends on the polarization and propagation direction of light. If the pump light and the generated light have different polarizations, they don't have to obey the same dispersion relation. Therefore the phase matching condition is possible to be satisfied.

Another way to solve this problem is to use quasi-phase matching. We already know that when the phase is mis-matched, the energy flows periodically between the pump field and generated fields. The technique of quasi-phase matching periodically flip the orientation of the crystalline axes whenever the energy is about to flow back from the generated fields to the pump field. This ensures that the energy always flows from the pump field to the second harmonic fields even though their phases are not matched perfectly. The quasi-phase matched crystals are usually made with the technique of periodic poling. The most common periodic polled materials in the lab are PPLN, PPKTP, PPLT, etc. Fig.2.9 shows the comparison of phase-matched, phase-mismatched and quasi-phase matched conditions.

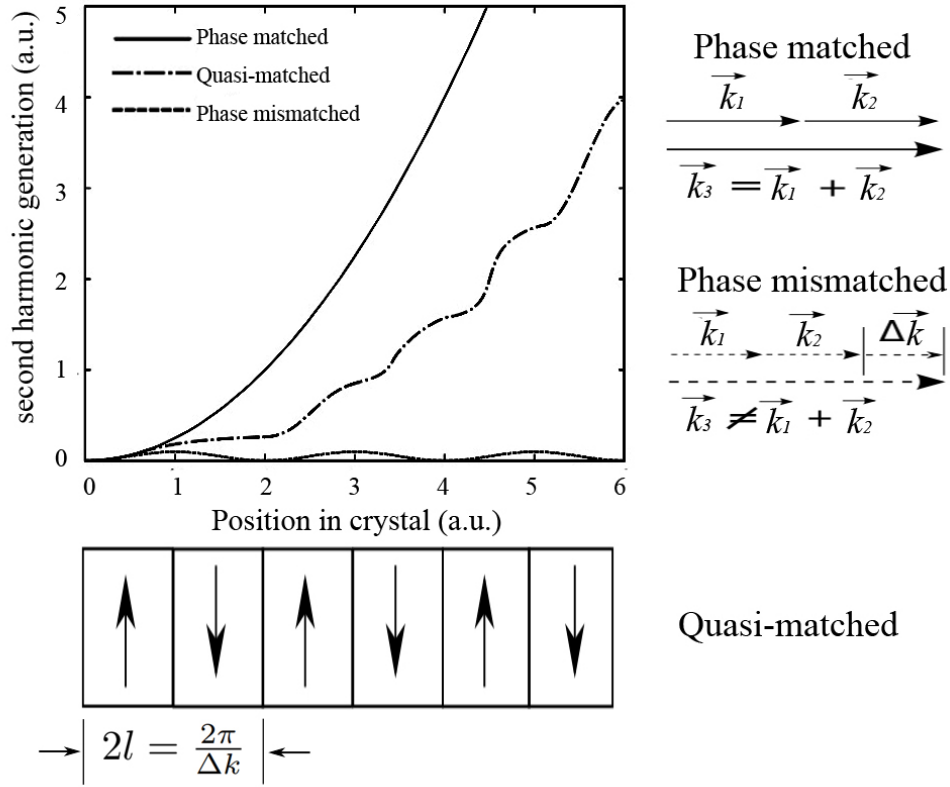


Figure 2.9. Comparison of second harmonic generation when it is phase-matched, phase mismatched and quasi-phase matched. The amplitude of the second harmonic generated field increases exponentially when the phase matching condition is satisfied (the solid line). When the phase is mismatched, the generated field oscillates at low amplitude and there is almost no output field (the dashed line). Quasi-phase matching technique alternates crystal orientation periodically so that the energy flows positively consecutively from the pump field to the second harmonic generated field (the dash-dot line).

2.2.4 Spontaneous Parametric Down-conversion

Spontaneous parametric down-conversion is one type of nonlinear TWM process which converts one pump light beam of frequency of ω_3 into two light beams of frequencies of ω_1, ω_2 . It is usually achieved by the nonlinear crystals pumped by a strong pulse laser beam. It will produce two output fields entangled in many variables. We give them the names: signal and ideal beam. The input and output photons obey the conservation law of energy and

momentum, as shown in Fig.2.10. SPDC is caused by the second order expansion term of electrical polarization. Since the $\hat{a}(\omega_1 + \omega_2)$ -field in Eq.(2.21) is in a coherent state from a strong pump laser. We replace the operator with a complex number: $\hat{a}(\omega_1 + \omega_2) \rightarrow \alpha_p(\omega_1 + \omega_2)$ where $\alpha_p(\omega_1 + \omega_2)$ is the spectral profile of the laser which is usually a Gaussian function (since the time duration of a laser pulse is short and Heisenberg uncertainty principle, the conjugate variable frequency band should be broad). We have

$$\frac{1}{i\hbar} \int dt \hat{H}_{int} = \int d\omega_1 d\omega_2 F(\omega_1, \omega_2) \hat{a}_s^\dagger(\omega_1) \hat{a}_i^\dagger(\omega_2) + h.c., \quad (2.24)$$

where

$$F(\omega_1, \omega_2) = \zeta \text{sinc}(\Delta K L / 2) e^{-i\Delta K L / 2} \alpha_p(\omega_1 + \omega_2). \quad (2.25)$$

$F(\omega_1, \omega_2)$ is joint spectrum function. In particular, $|F(\omega_1, \omega_2)|^2$ is known as joint spectral intensity. Fig.2.11 plots a typical normalized amplitude of JSF $|F(\Omega_1, \Omega_2)/F(0, 0)|$. Here the zero point of the frequency of ω is shifted to the center frequency of the pump beam and normalized to Ω which has the unit of unity. We can see that the frequencies of signal and idler fields are anti-correlated. The distribution ranges of frequency in the direction perpendicular and parallel to the line of $\Omega_1 + \Omega_2 = 0$ are confined by the the pump envelope term $\alpha_p(\Omega_1 + \Omega_2)$ and phase matching term $\text{sinc}(\Delta K L / 2)$, respectively.

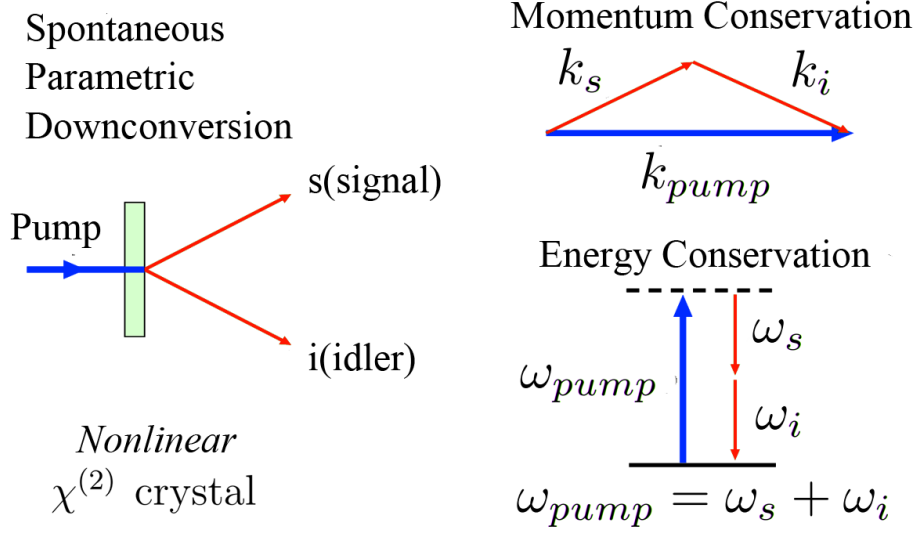


Figure 2.10. Schematic of SPDC process. The process obeys the conservation law of momentum and energy.

Expansion of Joint Spectrum Function with Temporal Modes

SPDC is a very important source in the quantum network to generate optical fields in the desired way. It is also widely used to generate entanglement beams, and also to make heralded single photons, so it is important to study and measure its TMs. Analyzing the JSF can give us a lot of information such as the degree of the entanglement and the TM structure of the output beam.

Let's first review the TM. Without loss of generality, we use the single-photon state to introduce TM for concise purposes. In the previous section, we know that TMs form a complete basis in the frequency mode space. For a fixed polarization and spatial mode optical field, any single-photon state can be expanded by this basis.

$$\int d\omega f(\omega) |1_\omega\rangle = \sum_{j=1}^{\infty} \int \frac{d\omega}{2\pi} c_j f_j(\omega) \hat{a}^\dagger(\omega) |0\rangle = \sum_{j=1}^{\infty} \int dt c_j \tilde{f}_j(t) \hat{a}^\dagger(t) |0\rangle, \quad (2.26)$$

where c_j is the complex-valued expansion coefficient. $\tilde{f}_j(t)$ is the Fourier transform of f_j , and they satisfied

$$\frac{1}{2\pi} \int d\omega f_j^*(\omega) f_k(\omega) = \int dt \tilde{f}_j^*(t) \tilde{f}_k(t) = \delta_{j,k}. \quad (2.27)$$

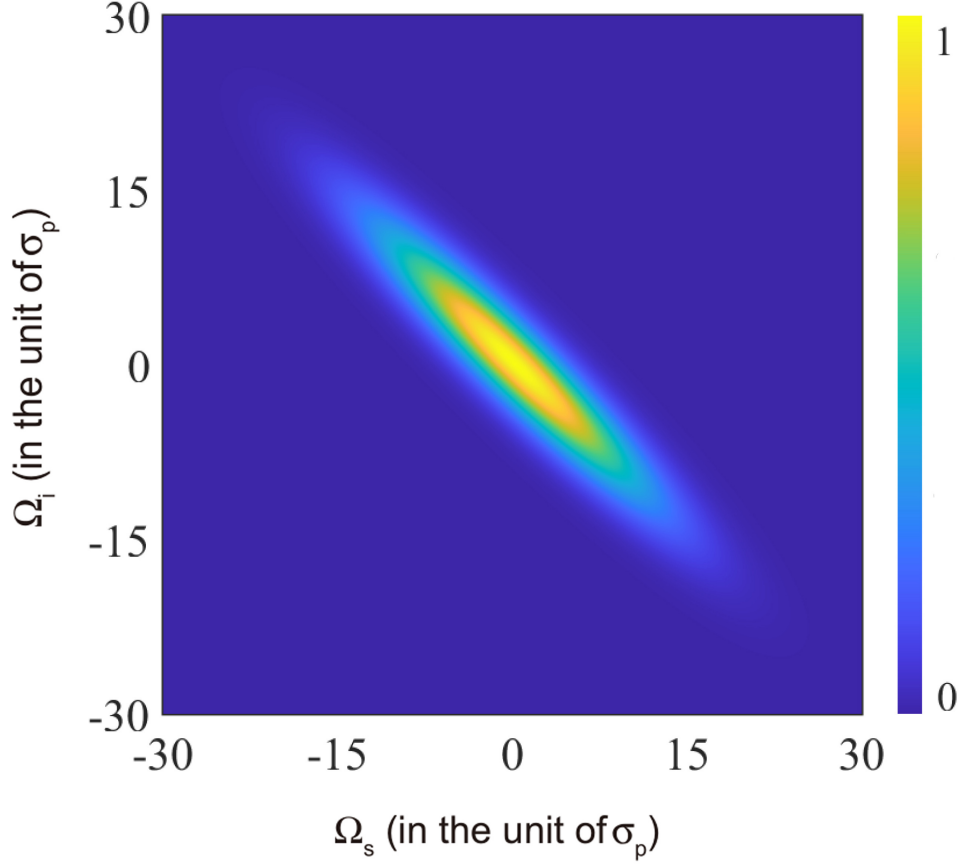


Figure 2.11. Normalized absolute value of the JSF $|F(\Omega_1, \Omega_2)/F(0, 0)|$ of twin beams generated by a pulse pumped SPDC process. The frequency is in the unit of the power of the pump field σ_p

The operator can be defined as

$$\hat{A}_j^\dagger = \frac{1}{2\pi} \int d\omega f_j(\omega) \hat{a}^\dagger(\omega) = \int dt \tilde{f}_j(t) \hat{a}^\dagger(t). \quad (2.28)$$

The single-photon state can be expressed as $\sum_{j=1}^{\infty} c_j \hat{A}_j^\dagger |0\rangle$.

In the SPDC process pumped by pulse laser fields, two-photon states are generated in the signal and idler fields. When the pump power is relatively low, the dominating

interaction leads to two-photon generation. The generated signal and idler fields and the output quantum state takes the form of [37]

$$|\Psi_2\rangle \approx |vac\rangle + \int d\omega_1 d\omega_2 F(\omega_1, \omega_2) \hat{a}^\dagger(\omega_1) \hat{a}^\dagger(\omega_2) |vac\rangle, \quad (2.29)$$

This is obtained by expansion of the time evolution operator and takes the first two terms:

$$\hat{U} = \exp\left(\int dt \frac{\hat{H}_{int}^{(2)}}{i\hbar}\right) \approx 1 + \int dt \frac{\hat{H}_{int}^{(2)}}{i\hbar}. \quad (2.30)$$

When the JSF $F(\omega_1, \omega_2)$ can be factorized to $G\psi(\omega_1)\varphi(\omega_2)$, with $\int d\omega_1 \psi^*(\omega_1)\psi(\omega_1) = 1 = \int d\omega_2 \varphi^*(\omega_2)\varphi(\omega_2)$, we obtain the A^\dagger and B^\dagger by integrating the frequencies ω_1 and ω_2 . The output state is

$$|\Psi_2\rangle \approx |vac\rangle + G\hat{A}^\dagger\hat{B}^\dagger|vac\rangle = |vac\rangle + G|1\rangle_s|1\rangle_i, \quad (2.31)$$

where operators $\hat{A}^\dagger \equiv \int d\omega_1 \psi(\omega_1) \hat{a}_s^\dagger(\omega_1)$, $\hat{B}^\dagger \equiv \int d\omega_2 \varphi(\omega_2) \hat{a}_i^\dagger(\omega_2)$, define single TM for the signal and idler fields, respectively. $|1\rangle_s \equiv \hat{A}^\dagger|vac\rangle$ and $|1\rangle_i \equiv \hat{B}^\dagger|vac\rangle$ are the single-photon states in those TMs. From it we can see the TM \hat{A}^\dagger and \hat{B}^\dagger are not entangled. In this case, if we just look at one beam, either signal or idler, the output is in a single TM. We can get single photon or multi photons in the single mode in one beam by detecting the other beam.

When the JSF can not be factorized, we use a mathematical tool, singular value decomposition, to deal with this situation [7], [15], [38]. It says any two variable function $F(\omega_1, \omega_2)$ can be expressed via singular mode decomposition method as Schmidt mode expansion in a form of

$$F(\omega_1, \omega_2) = \sum_k G r_k \psi_k(\omega_1) \varphi_k(\omega_2) \quad (2.32)$$

with $r_k \geq 0$ ($k = 1, 2, \dots$) and $\sum_k r_k^2 = 1$ and two sets of orthonormal functions $\{\psi_k(\omega_1), \varphi_k(\omega_2)\}$ satisfying

$$\int d\omega_1 \psi_k^*(\omega_1) \psi_{k'}(\omega_1) = \delta_{kk'} = \int d\omega_2 \varphi_k^*(\omega_2) \varphi_{k'}(\omega_2). \quad (2.33)$$

With mode decomposition in Eq.(2.32), the state in Eq.(2.29) can be rewritten as

$$|\Psi_2\rangle \approx |vac\rangle + G \sum_k r_k \hat{A}_k^\dagger \hat{B}_k^\dagger |vac\rangle = |vac\rangle + G \sum_k r_k |1_k\rangle_s |1_k\rangle_i, \quad (2.34)$$

where operators $\hat{A}_k^\dagger \equiv \int d\omega \psi_k(\omega) \hat{a}_s^\dagger(\omega)$, $\hat{B}_k^\dagger \equiv \int d\omega \varphi_k(\omega) \hat{a}_i^\dagger(\omega)$, define TMs for the signal and idler fields, respectively. And $|1_k\rangle_s \equiv \hat{A}_k^\dagger |vac\rangle$, $|1_k\rangle_i \equiv \hat{B}_k^\dagger |vac\rangle$ are the single-photon states in those TMs. The way in which $|\Psi_2\rangle$ is expressed in terms of the TMs in Eq.(2.34) indicates that it is a multi-mode two-photon state and is in the form of high-dimensional entanglement. It means if the signal beam is at the k th TM \hat{A}_k^\dagger , the idler beam must be at the k th TM \hat{B}_k^\dagger , as shown in the Fig.2.12. If we look at only one beam and ignore the other one by tracing it, we will get a multi-modes beam. It is also a mixed state in the first quantization view.

In Heisenberg picture, the input output relations for SPDC is

$$\begin{aligned} \hat{A}_k^{out} &= \hat{A}_k^{in} \cosh G_k + \hat{B}_k^{in\dagger} \sinh G_k \\ \hat{B}_k^{out} &= \hat{B}_k^{in} \cosh G_k + \hat{A}_k^{in\dagger} \sinh G_k. \end{aligned} \quad (2.35)$$

where $G_k \equiv r_k G$. It is equivalent to the output state expression in Eq.(2.31) derived in the interaction picture. The input and output annihilation relation tells that the input and output fields are only related within the same TM. The fields from different TM are decoupled.

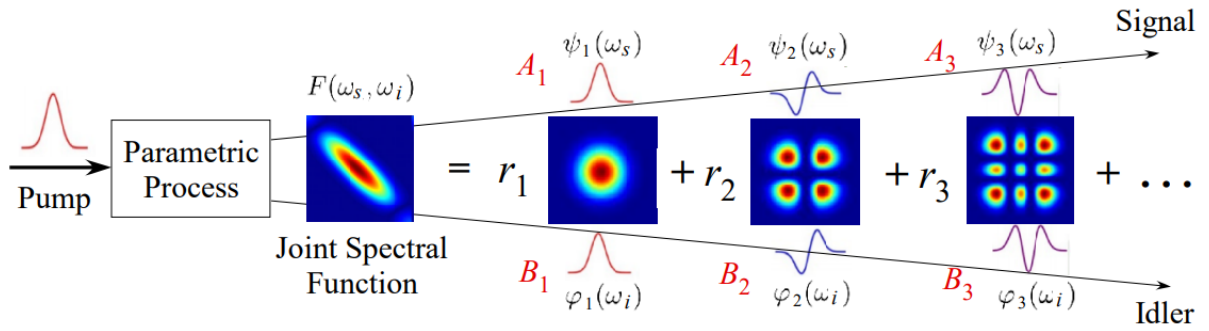


Figure 2.12. Entangled two-photon states consisting of various TMs A_k , B_k ($k = 1, 2, 3, \dots$) in the signal and idler fields generated from a pulse-pumped parametric process (Adapted from Ref.[39]).

3. MEASUREMENT OF TEMPORAL MODE STRUCTURE OF ENTANGLED FIELDS IN CONTINUOUS AND DISCRETE VARIABLES

3.1 Direct Temporal Mode Measurement for High Gain Parametric Amplifier

Pulse-pumped spontaneous parametric processes, because of precise timing provided by the ultra-short pump pulses [8], [9], have wide applications in QIS such as time-bin entanglement, quantum multi-photon interference of independent sources, heralded single-photon sources. However, the broad bandwidth of the pump field and strict phase matching condition in highly dispersive nonlinear medium lead to complicated spectral correlation in the frequency domain.

Fortunately, the issue of complicated spectral correlation was solved in the time domain by making a Schmidt decomposition of the JSF and finding that the generated two-photon field can be decomposed into a superposition of independent pairs of TMs [7], as Eq.(2.31) shown. It was shown later that this mode decomposition can be extended to the high gain domain [15]–[17]. This method significantly simplifies the quantum description for the two-photon fields, leading to multi-dimensional temporal quantum entanglement. Such a TM description was recently extended more generally into field-orthogonal TM analysis of electromagnetic fields and was shown to form a different framework for QIS [12].

On the other hand, the specific mode functions of the TMs are only revealed by theoretical simulations through the JSF of parametric processes [7], [15]–[17]. They can be indirectly obtained through singular value decomposition when the JSF is measured [18]. But they have never been measured directly. We use a feedback-iteration method with a trial seed pulse to obtain and eventually measure the exact forms of the TMs of the two correlated fields generated from a pulse-pumped single-pass broadband fiber PA. In our method, we exploit the stimulated emission process corresponding to SPDC, which is often called optical parametric amplifier (OPA). It is just SPDC plus a seed signal or idler field. SPDC can be treated as the OPA applied on the vacuum. With the seed field, OPA will enhance the

output field significantly while sharing the same phase match relation of SPDC. This can be seen from

$$\begin{aligned}\hat{a}^\dagger |0\rangle &= 1 \times |0\rangle, \\ \hat{a}^\dagger |n\rangle &= \sqrt{n+1} |n+1\rangle.\end{aligned}\tag{3.1}$$

When the creation operator \hat{a}^\dagger in Eq.(3.1) applies to the vacuum state, the probability of emission is proportional to unity, while when it applies to the $|n\rangle$ state, the probability of emission is proportional to $n+1$.

Our method of measuring the mode structure has to be adjusted a little bit for the two different situations, high gain and low gain case of SPDC process. The two cases just refer to a relatively stronger and weaker power of the pump beam. The higher power pump beam will result in a relatively larger output field. The high gain SPDC is usually used as the light source in the continuous variable measurement or application with the homodyne detection technique. The low power pump beam produces a weak output field. It is often used as the light source in the discrete variable measurement or application with the photon counting detection technique.

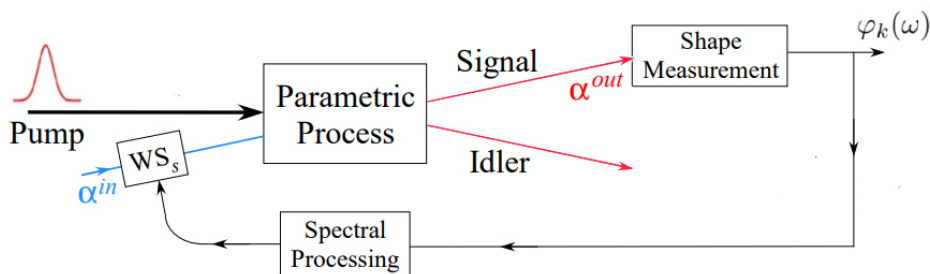


Figure 3.1. Schematic diagram for measuring the mode functions at high gain. WS: wave shaper.

Our procedure to find the mode functions $\psi_k(\omega), \varphi_k(\omega)$ is based on Eq.(2.35). We inject a seed into the signal field and observe its output by using the pulse characterization method [40]. This is somewhat similar to the method of stimulated emission tomography [25], [41]. But here, after measuring the spectral shape of the output, we feed the result back to

modify the input seed and iterate the process (see Fig.3.1). This part is similar to the adaptive method of Polycarpou *et al* [42]. To see what this leads to, we consider a coherent pulse of spectral shape $\alpha_0(\omega)$ injected into the field A . Because of the orthogonality and completeness of the TM basis in the frequency space, we can expand it as

$$\alpha_0(\omega) = \sum_k \xi_k \psi_k(\omega) \quad (3.2)$$

with $\xi_k = \int d\omega \psi_k^*(\omega) \alpha_0(\omega)$. Using Eq.(2.35) and assuming $|\xi_k|^2 \gg 1$ to ignore spontaneous emission, we find

$$\alpha^{out}(\omega) = \sum_k \xi_k \cosh G_k \psi_k(\omega). \quad (3.3)$$

So, each mode is amplified but with different gain. Now let us exploit this gain difference: we can measure the output spectral function (amplitude and phase) and then program a new input field with a wave shaper according to the measured function. To keep the input power low, we can attenuate the output by a factor, say $(\cosh G_1)^{-1}$, so that the new input becomes

$$\alpha_1(\omega) = \sum_k \xi_k (\cosh G_k / \cosh G_1) \psi_k(\omega). \quad (3.4)$$

Since G_k 's are different for different k , let us arrange mode order: $G_1 > G_2 > \dots$ and $\cosh G_k / \cosh G_1 < 1$ for all except $k = 1$. We iterate the procedure N times and the field after N iterations becomes

$$\alpha_N(\omega) = \sum_k \xi_k (\cosh G_k / \cosh G_1)^N \psi_k(\omega). \quad (3.5)$$

With N large enough, $(\cosh G_k / \cosh G_1)^N \rightarrow 0$ for $k \neq 1$ and we are left with only the first mode: $\alpha_N(\omega) \propto \psi_1(\omega)$.

To obtain the mode function for $k = 2$, we need to have an input field that is orthogonal to $\psi_1(\omega)$, that is, $\xi_1 = 0$. To achieve this, we use the Gram-Schmidt process: with $\psi_1(\omega)$ known, we set the input as $\alpha'(\omega) = \alpha(\omega) - \xi_1 \psi_1(\omega)$, which has $\xi'_1 = 0$. Then the dominating mode

is $k = 2$. We perform orthogonalization after each iteration to ensure $\xi'_1 = 0$. Subsequent modes can be obtained in a similar way but with the orthogonalization changed to $\alpha'(\omega) = \alpha(\omega) - \sum_{i=1}^{k-1} \xi_i \psi_i(\omega)$ for mode k .

This method can also be understood in the following way which provides a more clear picture but less precise in equation derivation. Since the idler input port of the OPA is always left in the vacuum state, we can simplify the first equation of Eq.(2.35) as

$$\hat{A}_k^{out} = \hat{A}_k^{in} \cosh G_k \quad (3.6)$$

with classical approximation. In the method we program the seed field each time based on the spectral profile of the output beam, and iterate the process. It is equivalent to a virtual process that uses the output field directly as the seed beam and goes through the same nonlinear interaction. Therefore we can describe the iteration process with

$$\hat{A}_k^{out} = \hat{A}_k^{in} (\cosh^n G_k) / G'^n \quad (3.7)$$

by iteratively substituting \hat{A}_k^{out} with \hat{A}_k^{in} in Eq.(3.6). Here n is the iteration number and G' is the factor by which the power of the output field is scaled down to the same level of the input seed field.

From this we can see, the fields of each mode are amplified independently with the amplification rate proportional to the $(\cosh G_k) / G'$. The amplification rate of the mode with small index is larger than the one with large index as discussed above. Therefore after repeating the process many times, only the mode with the largest amplification is left, as shown in Fig.3.2.

3.1.1 Theoretical Simulation and Experimental Results

In order to demonstrate the validity of the method, we run some simulations based on Eq.(3.5) for the JSF given in Ref.[17] but with a chirped pump phase of $e^{i\Omega^2/2\sigma_p^2}$. The parametric process is a pulse-pumped four-wave mixing in a dispersion-shifted fiber. With

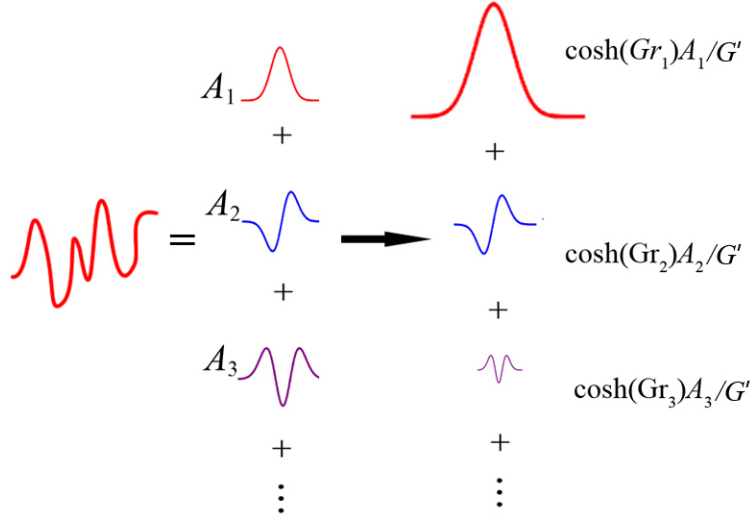


Figure 3.2. Working principle: Arbitrary field can be expanded with TMs. The fields of each mode are amplified independently with the amplification rate proportional to the $(\cosh G_k)/G'$. The mode with the largest amplification will be left after iterating the process.

spectrum shifted to the center frequencies ω_{s0}, ω_{i0} of signal and idler beams by defining $\Omega_{s,i} \equiv \omega_{s,i} - \omega_{s0,i0}$, the JSF has the specific form of

$$F(\Omega_s, \Omega_i) = F e^{i(\Omega_s + \Omega_i)^2 / 2\sigma_p^2} \exp\left\{-\frac{(\Omega_s + \Omega_i)^2}{4\sigma_p^2}\right\} \times \exp\left\{\left(\frac{-i\Delta kL}{2}\right)\right\} \text{sinc}\left(\pi \frac{\Delta kL}{2}\right). \quad (3.8)$$

Here F is some constant proportional to the amplitudes of the pump fields and nonlinear coefficient. The value of F is set so that $|F(\Omega_s, \Omega_i)|^2 = 2$ in the simulation. σ_p is the bandwidth of the pump field, ΔkL is the phase mismatch for fiber length of L . For the dispersion-shifted fiber used in Ref.[17], it is given by

$$\frac{\Delta kL}{2} \approx 0.125 \frac{\Omega_s}{\sigma_p} - 0.075 \frac{\Omega_i}{\sigma_p}. \quad (3.9)$$

The results are shown in Fig.3.3 for the first three modes. The green and dashed curves are the initial input and the final output spectral functions, respectively. The blue and red curves are for the intermediate steps with the step numbers shown in the legends.

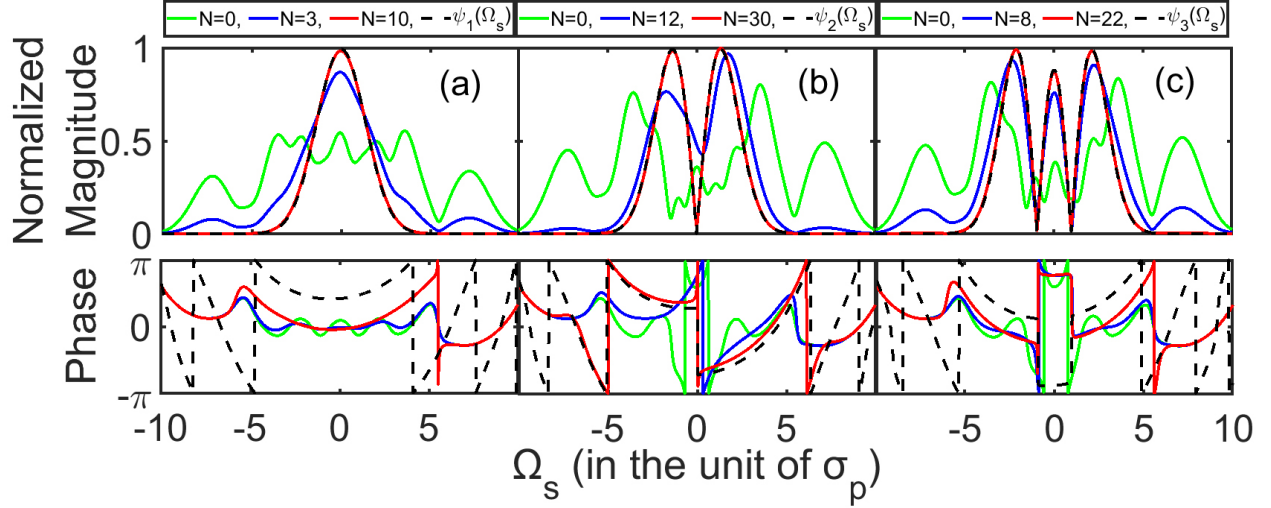


Figure 3.3. Simulation results for the amplitudes (top) and converged phases (bottom) of the output spectral functions $\psi_k(\Omega_s)$ ($\Omega_s \equiv \omega_s - \omega_{s0}$ in the unit of pump bandwidth σ_p) for (a) $k = 1$, (b) $k = 2$, (c) $k = 3$. The green curves are the input spectral functions while the blue and red curves are intermediate outputs after the iteration steps N indicated in the legends. The dashed curves are the final outputs.

An experiment is completed by a research group we cooperate with in Tianjin university to measure the mode structure of the pulse pumped fiber optical parametric amplifier (FOPA) in a high gain case. The experimental setup is shown in Fig.3.4(g), in which the pulse-pumped FOPA consists of two dispersion-shifted fibers (DSFs) and a single-mode fiber (SMF) [43]. The pump and the seed, with their path lengths carefully balanced through a delay line (not shown), are combined with a 90/10 beam splitter and simultaneously launched into the FOPA. The output of FOPA is measured by optical spectrum analyzer (OSA) to determine the spectral profile.

The TM profiles of the fiber PA are determined directly by the feedback-iteration method described previously. The recorded spectrum of the signal field by an OSA is used to reshape the input seed with a wave shaper. Although an OSA only measures the spectral intensity, here, in the first order approximation, it is assumed that there is no dispersion in the phases of the mode functions except a jump of π at zeros for higher order modes. Such an assumption is valid because the spectral phases are relatively flat within the spectral width (~ 3.5 nm) of the specially engineered source (see Ref.[44]). So a sign change is implemented for the higher

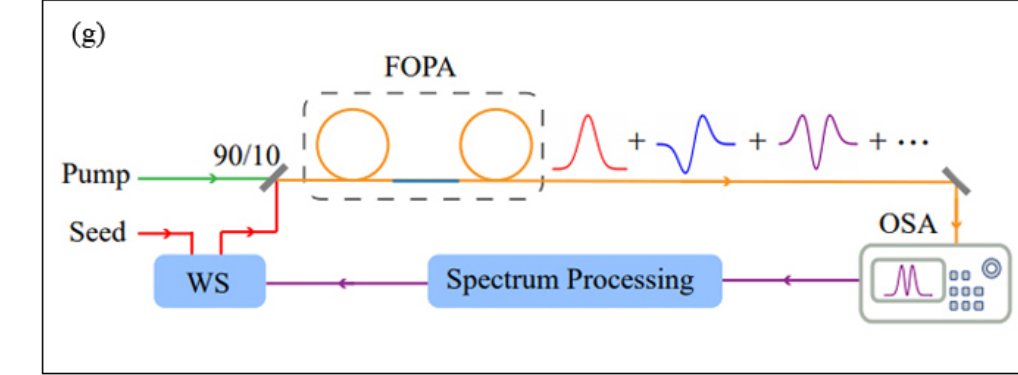
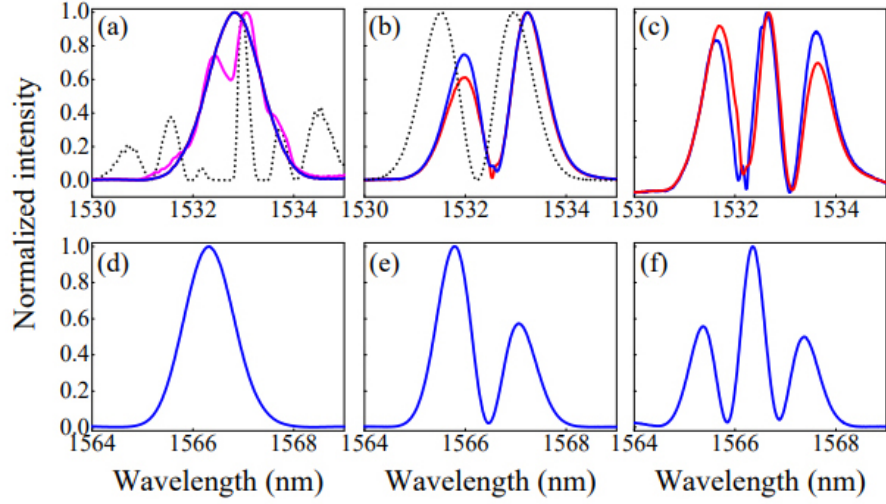


Figure 3.4. Measured spectral intensity $|\psi_k(\omega)|^2$ for $k =$ (a) 1, (b) 2, (c) 3, and those ((d),(e),(f)) for the corresponding idler field (Adapted from Ref.[19]). The dotted lines are the initially injected seed (not shown for (c) due to crowdedness). The pink curve in (a) is the output after two iterations. The blue lines are the output signal and the red lines are the feedback to the input (red is covered by blue in (a)). (g) is the experimental setup. WS, wave shaper; FOPA, fiber optical parametric amplifier; OSA, optical spectrum analyzer.

order mode cases whenever the spectral intensity goes to zero. After a number of iterations ($\sim 6 - 8$ depending on the shape of the initial injection), a steady shape is reached, which corresponds to one of the eigen TMs from the PA. The other eigen TMs are found following the steps described previously. The blue curves in Fig.3.4 are the converged spectral intensity of the first three TMs (a,b,c) together with those for the corresponding idler field (d,e,f). The curves are normalized to the maximum values. The dotted lines are the initially injected seed (only for (a) and (b)). The pink curve in Fig.3.4(a) is the output after only two iterations,

showing fast convergence of the iteration. For the higher order modes ($k = 2, 3$), there is a slight difference between the feedback input (red) and the output (blue). This is caused by the non-uniform spectral response of the detector as well as dispersion in phase of the higher order modes.

3.2 Direct Temporal Mode Measurement for Low Gain Parametric Amplifier

The method described above has to rely on the large gain difference among the different modes to eventually lead to the convergence to the mode with highest gain. At the low gain regime of spontaneous emission, the amplifier operates at near unit gain ($\cosh G_k \approx 1$ for all $G_k \approx 0$, this is due to the stimulated field is too small for the low gain case that it is dominated and covered by the seed beam) for all modes so there is basically no difference in gain and the method will not lead to a converged shape. One may want to turn up the pump power to push into the high gain regime but it is known that mode structure in parametric processes changes with the pump power at high gain [41], [45]. Thus the method in Ref.[19] does not work in the low gain regime for spontaneous photon pair generation to reveal the TM structure of the entangled photons discovered by Law et al [7]. We can solve this problem by making a small modification to the method so as to apply it to the low gain case to directly measure the mode functions.

For low gain case, $|G_k| \ll 1$ so Eq.(2.35) can be approximated as

$$\begin{aligned}\hat{A}_k^{out} &\approx \hat{A}_k^{in} + G_k \hat{B}_k^{in\dagger} \\ \hat{B}_k^{out} &\approx \hat{B}_k^{in} + G_k \hat{A}_k^{in\dagger},\end{aligned}\tag{3.10}$$

or in terms of photon state format, the output state is approximately a two-photon state of the form [7], [15]–[17]

$$\begin{aligned}|\Psi_2\rangle &= |vac\rangle + \int d\omega_1 d\omega_2 F(\omega_1, \omega_2) \hat{a}_s^\dagger(\omega_1) \hat{a}_i^\dagger(\omega_2) |vac\rangle \\ &= |vac\rangle + \sum_k G_k \hat{A}_k^\dagger \hat{B}_k^\dagger |vac\rangle \\ &= |vac\rangle + G \sum_k r_k |1_{A_k}\rangle_s |1_{B_k}\rangle_i,\end{aligned}\tag{3.11}$$

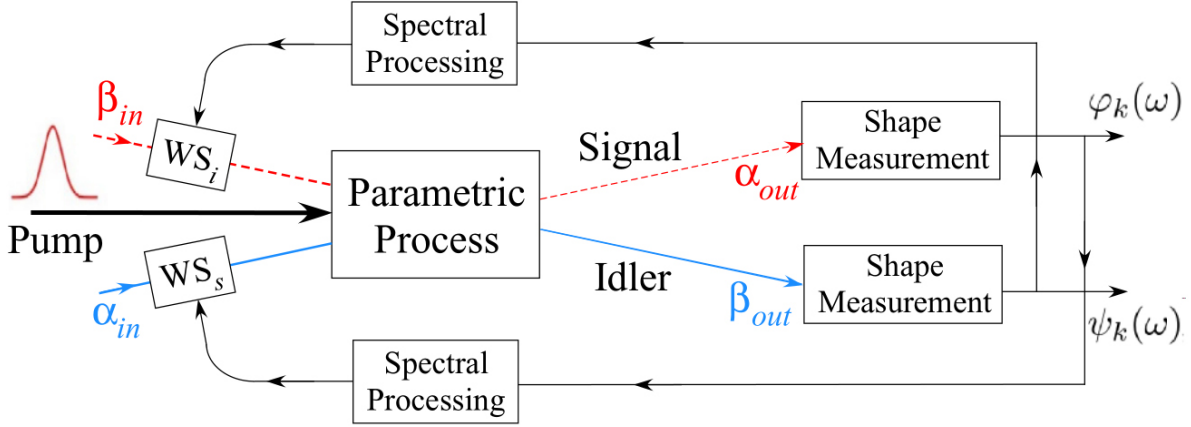


Figure 3.5. Schematic diagram for measuring the mode functions at low gain (Adapted from Ref.[39]). WS: wave shaper. The directly related light fields have the same line style (dashed or solid) and color (red or blue) and the direction of the arrow shows the flow of the iteration. The converged functions are the outputs that give the measured mode functions $\psi_k(\omega), \varphi_k(\omega)$.

where $|1_{A_k}\rangle_s \equiv \hat{A}_k^\dagger|vac\rangle = \int d\omega_1 \psi_k(\omega_1)|\omega_1\rangle_s, |1_{B_k}\rangle_i \equiv \hat{B}_k^\dagger|vac\rangle = \int d\omega_2 \varphi_k(\omega_2)|\omega_2\rangle_i$ are the single-photon states of modes \hat{A}_k, \hat{B}_k .

As shown in Fig.3.5, we first inject a seed (α_{in}) into the signal field and observe the output at the idler field (β_{out}). We use the information obtained at the measurement to modify the input seed with wave shapers: with the shape measured at idler (β_{out}), we then inject this shape of pulse into the idler field and in the meantime observe the output at the signal field (α_{out}). Now we have a new shape for the input signal seed. We then alternately inject the seed (α_{in} or β_{in}) at the signal or idler input based on the measurement result (α_{out} or β_{out}) and repeat this procedure until steady shapes are observed in both signal and idler fields.

To show the procedure converges, consider a coherent pulse of spectral shape $\alpha_{in}^{(0)}(\omega)$ as the initial injected seed into the signal field A . Because of the orthonormality of TMs (Eq.(2.33)), we can expand it as

$$\alpha_{in}^{(0)}(\omega) = \sum_k \xi_k \psi_k(\omega) \quad (3.12)$$

with $\xi_k = \int d\omega \psi_k^*(\omega) \alpha_{in}^{(0)}(\omega)$ as the excitation amplitude for mode k . Throughout the paper, we will assume $|\xi_k|^2 \gg 1$ in order to ignore spontaneous emission in the discussion. Since the gain is nearly 1, the signal output has no information about G_k . But it is different for the idler field. Using Eq.(3.10), we find the output at the idler field is approximately

$$\beta_{out}^{(1)}(\omega) = \sum_k \xi_k^* G_k \varphi_k(\omega). \quad (3.13)$$

So, the excitations for each mode are modified by G_k but with different coefficients. Now let us exploit this difference in the coefficients: we can measure the output spectral shape $\beta_{out}^{(1)}(\omega)$ at the idler field by using pulse characterization method [40] and then program an input seed of the shape $\beta_{in}^{(0)}(\omega) = C \beta_{out}^{(1)}(\omega)$ with a wave shaper (WS_i). The wave shaper electronic gain constant C can be taken as $C = 1/G_1$ to increase the input intensity, with G_1 defined in Eq.(2.35). At this time, the injection to the signal input is blocked, so the output at the signal field becomes

$$\alpha_{out}^{(1)}(\omega) = \frac{1}{G_1} \sum_k \xi_k G_k^2 \psi_k(\omega). \quad (3.14)$$

Now apply this to another wave shaper (WS_s) with the same gain $C = 1/G_1$ to produce a new spectral shape for the input seed of the signal field and obtain

$$\begin{aligned} \alpha_{in}^{(1)}(\omega) &= C \alpha_{out}^{(1)}(\omega) \\ &= \frac{1}{G_1^2} \sum_k \xi_k G_k^2 \psi_k(\omega) \\ &= \sum_k \xi_k (r_k/r_1)^2 \psi_k(\omega), \end{aligned} \quad (3.15)$$

which, from Eq.(3.13), leads to the output at the idler:

$$\begin{aligned} \beta_{out}^{(2)}(\omega) &= \frac{1}{G_1^2} \sum_k \xi_k^* G_k^3 \varphi_k(\omega) \\ &= G_1 \sum_k \xi_k^* (r_k/r_1)^3 \varphi_k(\omega), \end{aligned} \quad (3.16)$$

Since $r_1 > r_2 > \dots$, we have $(r_k/r_1)^2 < 1$ for all modes except the first one ($k = 1$) and their excitation amplitudes are reduced. We can then iterate the procedure N times and the output field after N iterations becomes

$$\begin{aligned}\beta_{out}^{(N)}(\omega) &= G_1 \sum_k \xi_k (r_k/r_1)^{2N-1} \varphi_k(\omega) \\ \alpha_{out}^{(N)}(\omega) &= G_1 \sum_k \xi_k (r_k/r_1)^{2N} \psi_k(\omega).\end{aligned}\tag{3.17}$$

With N large enough, $(r_k/r_1)^{2N} \rightarrow 0$ for $k \neq 1$ and we are left with only the first mode: $\alpha_{out}^{(N)}(\omega) \propto \psi_1(\omega)$ and $\beta_{out}^{(N)}(\omega) \propto \varphi_1(\omega)$. This procedure uniquely determines $\psi_1(\omega), \varphi_1(\omega)$ up to a normalization constant.

Similar with the high gain case, to obtain the mode function for $k = 2$, we use the Gram-Schmidt process: with $\psi_1(\omega), \varphi_1(\omega)$ known, we set the input as $\alpha'(\omega) = \alpha(\omega) - \xi_1 \psi_1(\omega)$ or $\beta'(\omega) = \beta(\omega) - \eta_1 \varphi_1(\omega)$ with $\eta_1 = \int d\omega \varphi_1^*(\omega) \beta(\omega)$, which gives $\xi'_1 = 0$ or $\eta' = 0$. Then the dominating mode will be $k = 2$. To ensure $\xi_1 = 0$ in the input of each iteration, we perform the orthogonalization step after each measurement of the output. Subsequent modes can be obtained in a similar way but with the orthogonal step changed to $\alpha'(\omega) = \alpha(\omega) - \sum_{i=1}^{k-1} \xi_i \psi_i(\omega)$ or $\beta'(\omega) = \beta(\omega) - \sum_{i=1}^{k-1} \eta_i \varphi_i(\omega)$ for mode k .

Same with the high gain case, this method can also be understood in a less precise way while providing a more clear picture. Since one of the input port of the OPA in the iteration process is left in the vacuum state, we can simplify Eq.(2.35) as

$$\begin{aligned}\hat{A}_k^{out} &\approx G_k \hat{B}_k^{in\dagger} \\ \hat{B}_k^{out} &\approx G_k \hat{A}_k^{in\dagger},\end{aligned}\tag{3.18}$$

with classical approximation. The step programming the seed field each time based on the measurement of the spectral profile of the output beam is equivalent to a virtual process

that uses the output field directly as the seed beam and goes through the same nonlinear interaction. Therefore we can describe the iteration process with

$$\begin{aligned}\hat{A}_k^{out} &\approx G_k^{2n} \hat{A}_k^{in} \\ \hat{B}_k^{out} &\approx G_k^{2n+1} \hat{A}_k^{in},\end{aligned}\tag{3.19}$$

by iteratively substituting \hat{A}_k^{out} with \hat{A}_k^{in} , and \hat{B}_k^{out} with \hat{B}_k^{in} in Eq.(3.18), respectively.

From this we can see, the fields of each mode TM A_k are amplified independently (it is actually reduced) by G_k^{2n} . In the meanwhile the corresponding TM B_k are also amplified by G_k^{2n+1} . Therefore after renormalization only the mode with the largest amplification is left with a large iteration number n .

3.2.1 Simulations of Temporal Mode Determination Processes

The argument above is based on the singular value decomposition of the JSF. To demonstrate its validity, we go back to the time evolution operator

$$\hat{U} = \exp \left\{ \frac{1}{i\hbar} \int dt \hat{H} \right\}\tag{3.20}$$

and check the output from the evolution process [15]. Unfortunately, because of the complexity in the JSF, we cannot have an analytical expression so we resort to numerical simulation. The evolution operator given in Eq.(3.20) for large pumping power is hard to evaluate [46] but at low pump power for the low gain regime, the dimensionless quantity $G^2 \equiv \int d\omega_1 d\omega_2 |F(\omega_1, \omega_2)|^2 \ll 1$ and we can expand the exponential in an infinite series and drop the higher order terms. So, the evolution operator can be approximated as [15], [47]

$$\begin{aligned}\hat{U} &= \exp \left\{ \frac{1}{i\hbar} \int dt \hat{H} \right\} \approx 1 + \frac{1}{i\hbar} \int dt \hat{H} \\ &= 1 + \int d\omega_1 d\omega_2 [F(\omega_1, \omega_2) \hat{a}_s^\dagger(\omega_1) \hat{a}_1^\dagger(\omega_2) - h.c.].\end{aligned}\tag{3.21}$$

So, the output becomes

$$\begin{aligned}\hat{a}_s^{out}(\omega) &= \hat{U}^\dagger \hat{a}_s(\omega) \hat{U} \\ &\approx \hat{a}_s(\omega) + \int d\omega_2 F(\omega, \omega_2) \hat{a}_i^\dagger(\omega_2),\end{aligned}\quad (3.22)$$

where we used the commutation relation $[\hat{a}_s(\omega), \hat{a}_s^\dagger(\omega_1)] = \delta(\omega - \omega_1)$ and dropped the higher order terms in $F(\omega_1, \omega_2)$. Similarly,

$$\begin{aligned}\hat{a}_i^{out}(\omega) &= \hat{U}^\dagger \hat{a}_i(\omega) \hat{U} \\ &\approx \hat{a}_i(\omega) + \int d\omega_1 F(\omega_1, \omega) \hat{a}_s^\dagger(\omega_1).\end{aligned}\quad (3.23)$$

If we inject a coherent state of $|\{\alpha(\omega)\}\rangle$ at the signal input port but vacuum at the idler port, the expectation value at the idler output will be

$$\langle \hat{a}_i^{out}(\omega) \rangle = \int d\omega_1 F(\omega_1, \omega) \alpha^*(\omega_1) \equiv \beta_{out}(\omega) \quad (3.24)$$

because the coherent state is independent. Similarly, for an input at the idler port of $|\{\beta(\omega)\}\rangle$, the output at the signal field is

$$\langle \hat{a}_s^{out}(\omega) \rangle = \int d\omega_2 F(\omega, \omega_2) \beta^*(\omega_2) \equiv \alpha_{out}(\omega). \quad (3.25)$$

Notice that with singular value decomposition in Eq.(2.32) for $F(\omega_1, \omega_2)$ and decomposition of Eq.(3.12) for $\alpha(\omega)$, we recover Eq.(3.13) from Eq.(3.24) by using the orthonormal relation in Eq.(2.33).

Furthermore, if we choose a mode-independent electronic gain constant C for the wave shaper, from Eq.(3.15) we find that once a specific eigenfunction, say, ψ_{k_0} is reached, that is, $\xi_k = \delta_{k, k_0}$, the ratio between next two outputs in the procedure is simply

$$\frac{\alpha_{out}^{(N+1)}(\omega)}{\alpha_{out}^{(N)}(\omega)} = CG^2 r_{k_0}^2 \propto r_{k_0}^2. \quad (3.26)$$

So, we can determine the mode numbers $\{r_k\}$ up to a normalization constant.

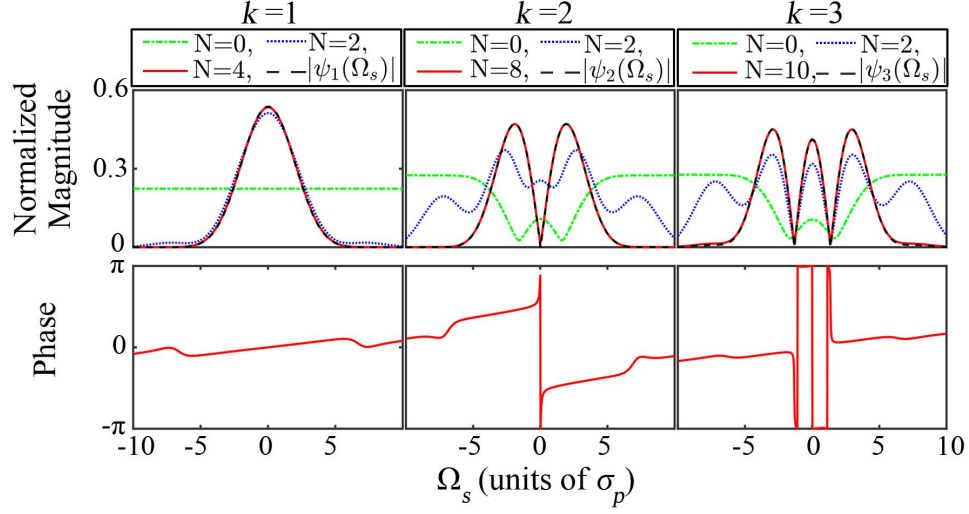
In order to demonstrate the validity of the procedure above, we consider the JSF given in Ref.[17] where the parametric process is a pulse-pumped four-wave mixing in a dispersion-shifted fiber. With spectrum shifted to the center frequencies ω_{s0}, ω_{i0} of signal and idler beams by defining $\Omega_{s,i} \equiv \omega_{s,i} - \omega_{s0,i0}$, the JSF has the specific form of

$$F(\Omega_s, \Omega_i) = F \exp \left\{ -\frac{(\Omega_s + \Omega_i)^2}{4\sigma_p^2} \right\} \times \exp \left\{ \left(\frac{-i\Delta kL}{2} \right) \right\} \text{sinc} \left(\frac{\Delta kL}{2} \right). \quad (3.27)$$

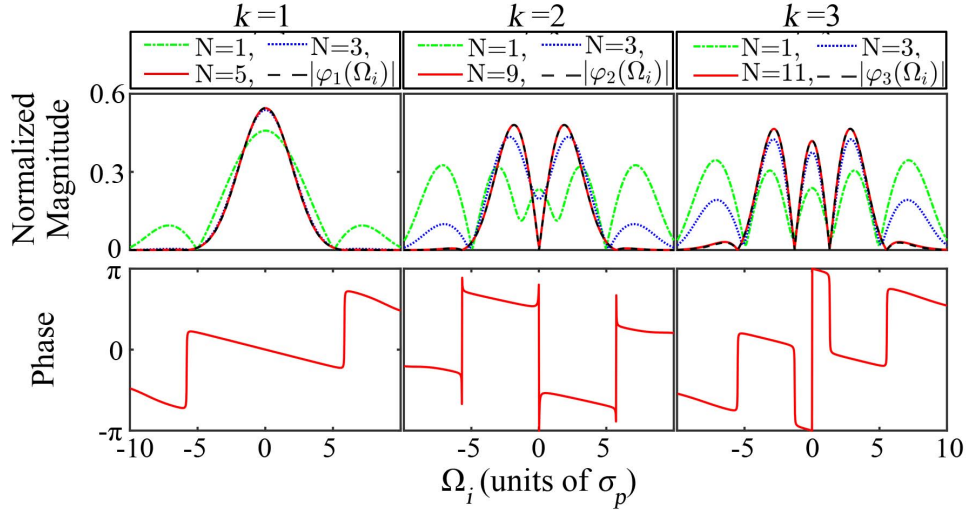
Here F is some constant proportional to the amplitudes of the pump fields and nonlinear coefficient, σ_p is the bandwidth of the pump field, ΔkL is the phase mismatch for fiber length of L . For the dispersion-shifted fiber used in Ref.[17], it is given by

$$\frac{\Delta kL}{2} \approx 0.125 \frac{\Omega_s}{\sigma_p} - 0.075 \frac{\Omega_i}{\sigma_p}. \quad (3.28)$$

Our simulation is based on Eq.(3.10), which is derived with the assumption of small $F(\Omega_s, \Omega_i)$ or $F \ll 1$ for low gain cases. But because of the small F value, the magnitudes of $\beta(\omega)$ and $\alpha(\omega)$ will become progressively decreased as we iterate the process. To maintain the size, we normalize the mode functions $\beta(\omega)$ and $\alpha(\omega)$ after each step of application of Eqs.(3.24, 3.25). So the results are independent of F , which is then set to 1 in the simulation. The absolute values and phases of the final converged mode functions of first three orders are shown in Fig.3.6(a) for the signal field ($\psi_{1,2,3}(\omega)$) and in Fig.3.6(b) for the idler field ($\varphi_{1,2,3}(\omega)$). The green dash-dotted curves are the initial input spectral functions and the black dashed curves are the final output spectral functions. The blue dotted and red solid curves are the output functions in the intermediate steps with the number of iterations shown in the legends. The magnitudes and phases of the mode functions are plotted separately with only final converged phase functions shown. It can be seen that the phase parts vary slowly except the π -jumps at zeros of the magnitude. The mode numbers $\{r_k\}$ are plotted in Fig.3.7 with normalization to r_1 . It can be seen that the mode functions and the mode numbers are the same as those obtained by the singular value decomposition method in Ref.[17] within the calculation accuracy.



(a)



(b)

Figure 3.6. Simulated convergent output spectral functions with their magnitudes and phases for the first three modes $k = 1, 2, 3$ for the JSF given in Eq.(3.27) (Adapted from Ref.[39]). (a) signal field $\psi_k(\Omega_s)$ and (b) idler field $\varphi_k(\Omega_i)$. The green dash-dotted curves are the input spectral functions while the blue dotted and red solid curves are intermediate outputs after the iteration steps indicated in the legends. The black dashed curves are the final outputs.

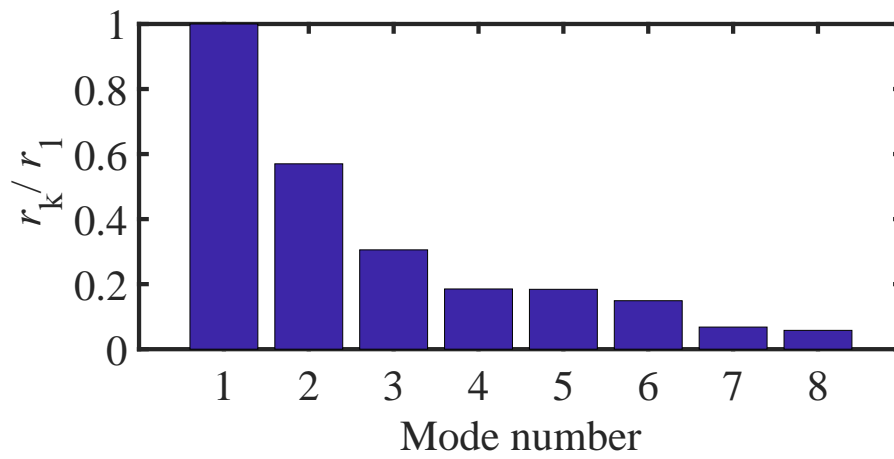


Figure 3.7. Mode number distribution obtained by simulation for the JSF given in Eq.(3.27) (Adapted from Ref.[39]).

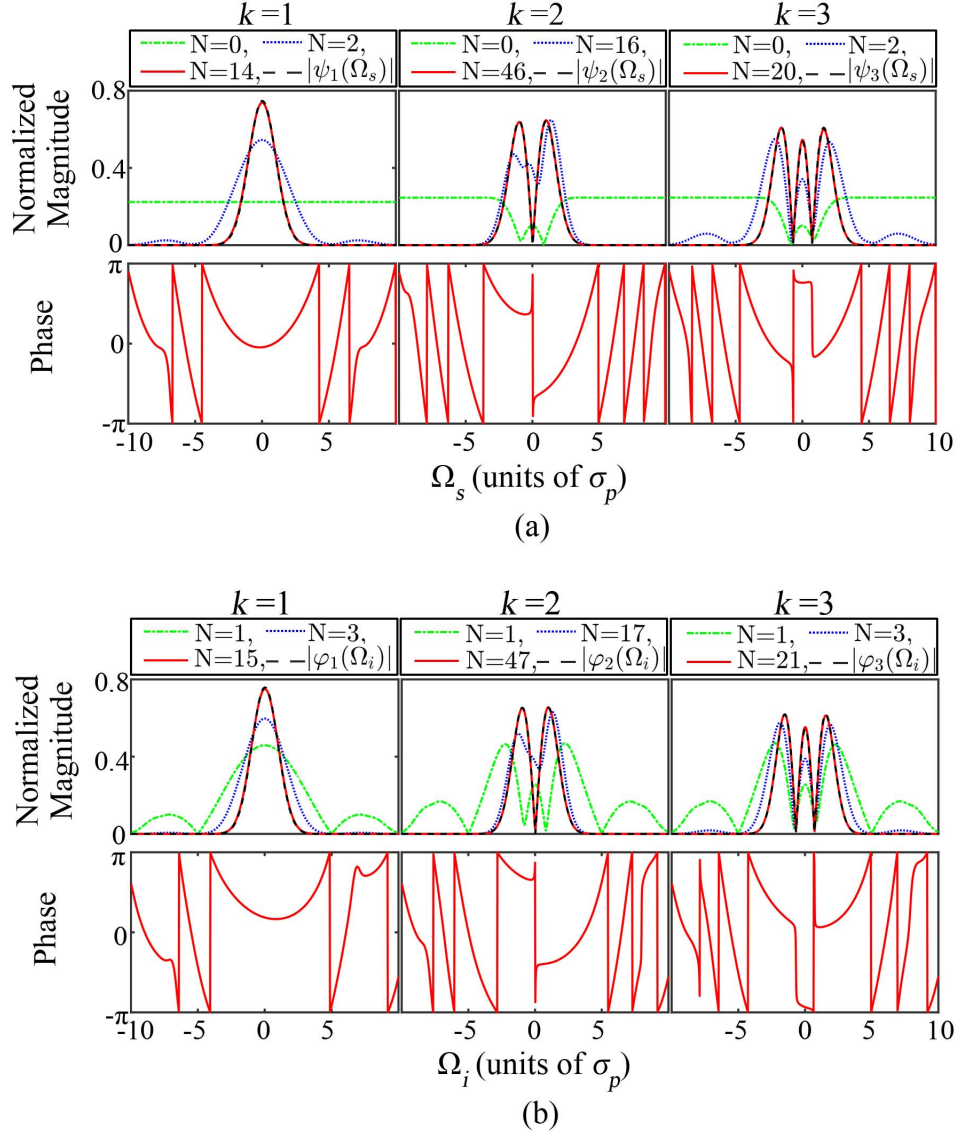


Figure 3.8. Simulated convergent output spectral functions with their magnitudes and phases for the first three modes $k = 1, 2, 3$ for the JSF given in Eq.(3.27) but with a chirped pump phase of $e^{i(\Omega_s + \Omega_i)^2 / \sigma_p^2}$ (Adapted from Ref.[39]). (a) signal field $\psi_k(\Omega_s)$ and (b) idler field $\varphi_k(\Omega_i)$. The green dash-dotted curves are the input spectral functions while the blue dotted and red solid curves are intermediate outputs after the iteration steps indicated in the legends. The black dashed curves are the final outputs.

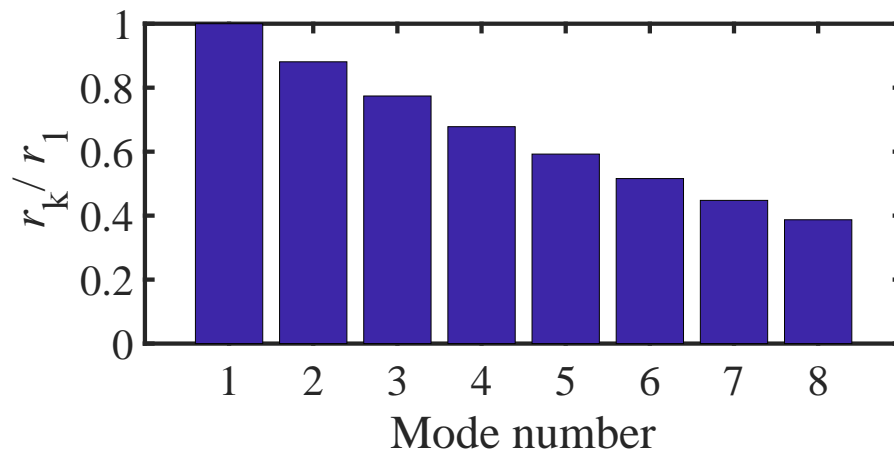


Figure 3.9. Mode number distribution obtained by simulation for the JSF given in Eq.(3.27) but with a modified phase of $e^{i(\Omega_s + \Omega_i)^2 / \sigma_p^2}$ added due to chirping of the pump field (Adapted from Ref.[39]).

As seen from Fig.3.6, the phases of the mode functions vary slowly with the frequency except a jump of π at zero points of the functions. This confirms the validity of the approximation of phase as a step function in Ref.[19]. To see an example of large phase variation in the mode functions, we add a chirped phase to the spectrum of the pump field resulting in a phase of $e^{i(\Omega_s+\Omega_i)^2/\sigma_p^2}$ to the JSF. Figure 3.8 shows the magnitudes and phases of the first three mode functions of the signal(a) and idler(b) fields for this case. As can be seen, the phases change rapidly as a function of frequency. Even though the extra chirped phase produces the same joint spectral intensity $|F(\omega_s, \omega_i)|^2$ as that in Eq.(3.27), it will change the mode structure as shown in the mode number distribution in Fig.3.9 as well as the bandwidths of the mode functions in Fig.3.8.

To further see the effectiveness of this procedure and the convergence processes, we calculate the ratio of the total output power of the idler to the total input power of the signal for each step, that is,

$$\left(R^{(2N-1)}\right)^2 \equiv \frac{\int d\omega |\beta_{out}^{(N)}(\omega)|^2}{\int d\omega |\alpha_{in}^{(N-1)}(\omega)|^2} \quad (3.29)$$

and similarly, the ratio of the output at the signal to the input at the idler

$$\left(R^{(2N)}\right)^2 \equiv \frac{\int d\omega |\alpha_{out}^{(N)}(\omega)|^2}{\int d\omega |\beta_{in}^{(N-1)}(\omega)|^2}, \quad (3.30)$$

where $N = 1, 2, 3, \dots$. These ratios can be measured experimentally. Since $\beta_{in}^{(N-1)}(\omega) \propto \beta_{out}^{(N)}(\omega)$ and $\alpha_{in}^{(N)}(\omega) \propto \alpha_{out}^{(N)}(\omega)$, using Eq.(3.17) and Eqs.(3.13,3.14), we can find for the first mode

$$\left(R_1^{(2N-1)}\right)^2 = \frac{\sum_{k=1}^{\infty} |\xi_k|^2 G_k^2 (r_k/r_1)^{4(N-1)}}{\sum_{k=1}^{\infty} |\xi_k|^2 (r_k/r_1)^{4(N-1)}} \quad (3.31)$$

and

$$\left(R_1^{(2N)}\right)^2 = \frac{\sum_{k=1}^{\infty} |\xi_k|^2 G_k^2 (r_k/r_1)^{4N-2}}{\sum_{k=1}^{\infty} |\xi_k|^2 (r_k/r_1)^{4N-2}}. \quad (3.32)$$

or combining the two cases above for $M = 2N - 1, 2N$, we have

$$\begin{aligned} \left(R_1^{(M)}\right)^2 &= \frac{\sum_{k=1}^{\infty} |\xi_k|^2 G_k^2 (r_k/r_1)^{2M-2}}{\sum_{k=1}^{\infty} |\xi_k|^2 (r_k/r_1)^{2M-2}} \\ &\rightarrow G^2 r_1^2 \text{ for } M \rightarrow \infty. \end{aligned} \quad (3.33)$$

M is now the overall step number. Likewise, for k_0 -th mode,

$$\begin{aligned} \left(R_{k_0}^{(M)}\right)^2 &= \frac{\sum_{k=k_0}^{\infty} |\xi_k|^2 G_k^2 (r_k/r_{k_0})^{2M-2}}{\sum_{k=k_0}^{\infty} |\xi_k|^2 (r_k/r_{k_0})^{2M-2}} \\ &\rightarrow G^2 r_{k_0}^2 \text{ for } M \rightarrow \infty. \end{aligned} \quad (3.34)$$

Like $\alpha_{out}^{(N)}, \beta_{out}^{(N)}$ in Eq.(3.17), the convergence of $R_{k_0}^{(M)}$ depends on the ratio r_k/r_{k_0} . So quantity $R_{k_0}^{(M)}$ can represent how the procedure converges as a function of step M . Hence, we calculate $R_{k_0}^{(M)}$ for each iteration step for the k_0 -th mode ($k_0 = 1, 2, 3$) and normalize it to Gr_1 for the JSF in Eq.(3.27). We plot it as a function of the iteration step numbers in Fig.3.10(a). It can be seen that after only a few steps, $R_k^{(M)}$ changes slowly and eventually converges to a final value r_k/r_1 . So, the rate of convergence is quite good. The normalized $R_{k_0}^{(M)}$ value of the first three mode is also plotted in Fig.3.10(b) for the JSF given in Eq.(3.27) but with a modified phase of $e^{i(\Omega_s + \Omega_i)^2 / \sigma_p^2}$ added due to chirping of the pump field. It shows a slower convergence rate because the r_k value of modes is more close to each other.

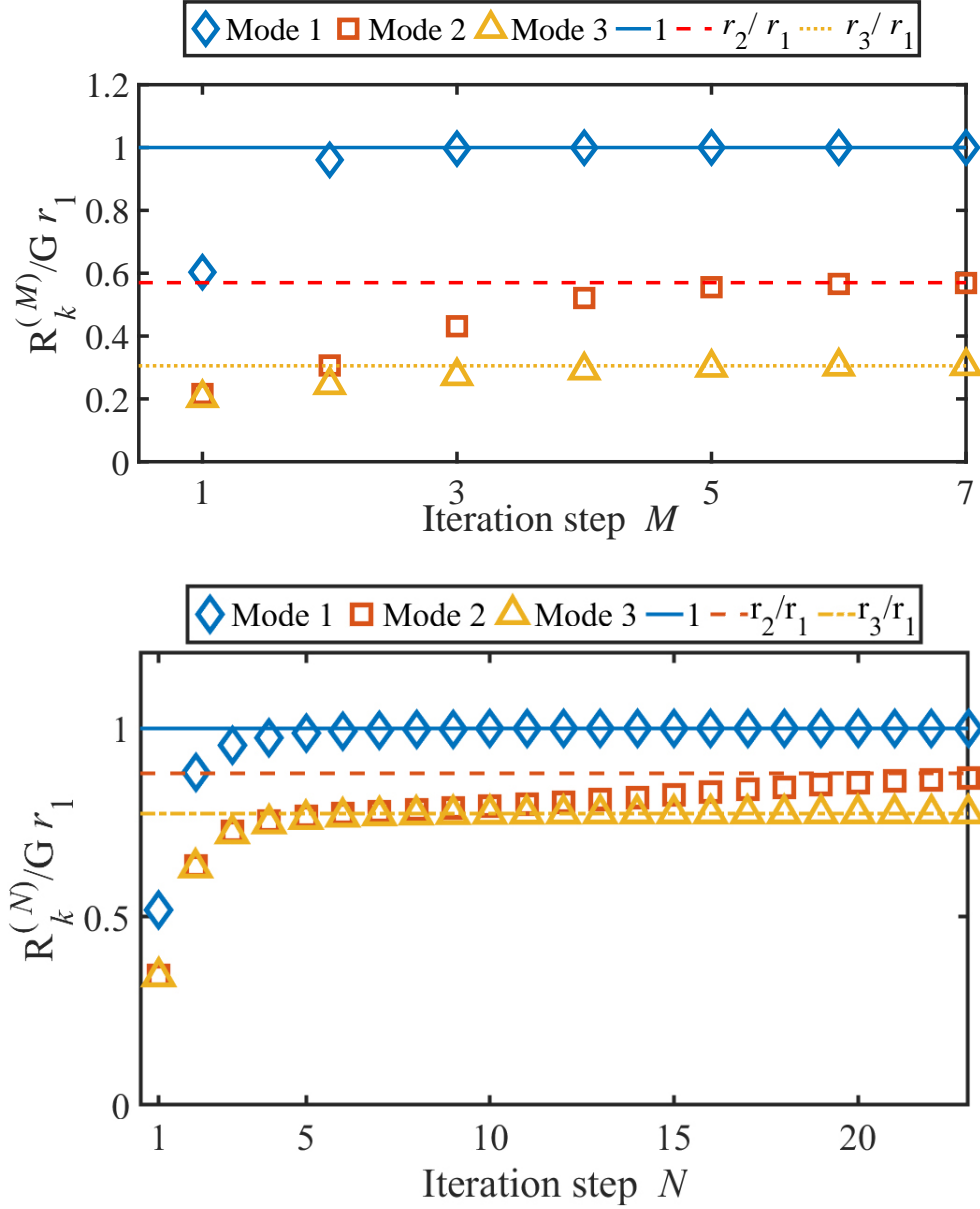


Figure 3.10. Normalized ratio $R_k^{(M)}/G r_1$ ($k = 1, 2, 3$) as a function of iteration step M , (a) ; obtained by simulation for the JSF given in Eq.(3.27) (Adapted from Ref.[39]), (b) for the JSF given in Eq.(3.27) but with a modified phase of $e^{i(\Omega_s + \Omega_i)^2 / \sigma_p^2}$ added due to chirping of the pump field. The straight lines are the limiting values of r_k/r_1 .

4. MODE STRUCTURE OF A BROADBAND HIGH GAIN PARAMETRIC AMPLIFIER

In the previous discussion we have not considered the issue of time ordering of the Hamiltonian. This treatment of parametric interaction Hamiltonian [15] fails when the gain of OPA exceeds some extent that the time ordering issue will play a significant role in the process and leads to the inaccurate result that TMs do not change in the high gain limit [41]. Indeed, recent studies with approaches that avoid the time ordering issue showed the spectrum broadening as the gain increases [45]. The experiment that directly measured the TM functions also confirmed the change of mode structure and mode functions as the gain increases [19].

The change of mode structure and mode functions with gain is troublesome in the production and applications of high quality quantum sources with quantum entanglement and noise reduction such as EPR entangled states and squeezed states, which require high gain operation in parametric processes. This is because the measurement on these states relies on the homodyne measurement technique in which the mode match between the local oscillator field (LO) and the quantum field is paramount and any mode mismatch is equivalent to losses and introduces extra vacuum noise. The knowledge of the exact profile of the mode functions will enable us to tailor the shape of LO field to match the quantum field [19]. But the change of the mode functions means that we also need to adjust the shape of LO to accommodate the change. The shape of the mode functions is also important for QPG [10], [11], [13] in TM multiplexing.

But so far there is no analysis about how mode structure and mode functions change with the gain. We investigate the pulse-pumped single-pass parametric processes at arbitrary pumping power. We will use an operator input-output approach that is usually employed for treating multi-stage nonlinear interferometers [48]. This avoids the time ordering issue of the interaction Hamiltonian and allows us to derive a set of coupled operator evolution equations in differential-integral form. We solve them numerically and analyze the mode structure and mode functions at the final output ports as a function of the pump parameter.

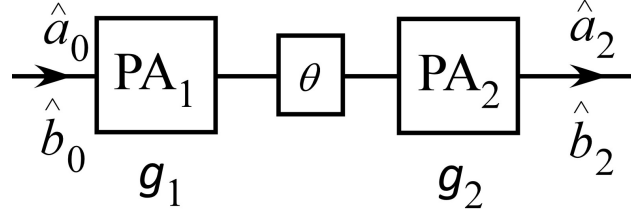


Figure 4.1. An SU(1,1) interferometer with PAs (PA_1, PA_2) in place of beam splitters (Adapted from Ref.[49]).

4.1 Multi-stage SU(1,1) Interferometers

In order to reveal the issue of time ordering in the derivation of evolution operator in parametric processes and find ways to tackle it, we consider an SU(1,1) interferometer, shown in Fig.4.1, which consists of two PAs (PA_1, PA_2) characterized by gain parameters g_1, g_2 together with a phase shift θ in between. This interferometer has recently been studied extensively [50] for precision phase measurement beyond standard quantum limit [51], quantum imaging with undetected photons [52], and quantum state engineering [43], [44].

The two PAs are described by the Hamiltonians:

$$\hat{H}_{PA}(\xi_j) = i\hbar\xi_j\hat{a}^\dagger\hat{b}^\dagger - i\hbar\xi_j^*\hat{a}\hat{b}, \quad (4.1)$$

where $j = 1, 2$. The input-output relations can be derived from evolution operators $\hat{U}_j = e^{(1/i\hbar)\hat{H}_{PA}(\xi_j)t}$ ($j = 1, 2$) and are respectively given as

$$\begin{aligned} \hat{a}_1 &= G_1\hat{a}_0 + g_1\hat{b}_0^\dagger, & \hat{b}_1 &= G_1\hat{b}_0 + g_1\hat{a}_0^\dagger; \\ \hat{a}_2 &= G_2\hat{a}'_1 + g_2\hat{b}'_1^\dagger, & \hat{b}_2 &= G_2\hat{b}'_1 + g_2\hat{a}'_1^\dagger; \end{aligned} \quad (4.2)$$

where $\hat{a}'_1 = \hat{a}_1 e^{i\theta/2}, \hat{b}'_1 = \hat{b}_1 e^{i\theta/2}$, the amplitude gains $g_j \equiv (\xi_j/|\xi_j|) \sinh |\xi_j t|$ ($j = 1, 2$), and $G_j = \cosh |\xi_j t|$ for the interaction time period of t . Here we assume the phase shifts are the same for both fields: $\theta_a = \theta_b = \theta/2$. The outputs of the interferometer are then [48]

$$\hat{a}_2 = G_T\hat{a}_0 + g_T\hat{b}_0^\dagger, \quad \hat{b}_2 = G_T\hat{b}_0 + g_T\hat{a}_0^\dagger, \quad (4.3)$$

with

$$\begin{aligned} G_T &= G_1 G_2 e^{i\theta/2} + g_1^* g_2 e^{-i\theta/2} \\ g_T &= G_1^* g_2 e^{-i\theta/2} + g_1 G_2 e^{i\theta/2}. \end{aligned} \quad (4.4)$$

This shows that we can treat the whole system as one PA with equivalent amplitude gains g_T , G_T . Furthermore, besides a propagation phase of $e^{i\theta/2}$ for both fields, the extra phase shift $e^{i\theta}$ can be absorbed in g_2 by redefining $g'_2 \equiv g_2 e^{-i\theta}$ or $\xi'_2 \equiv \xi_2 e^{-i\theta}$. Here $\xi'_2 = \xi_2 e^{-i\theta}$ takes the propagation phase shift $e^{i\theta}$ into consideration. Notice that only when $\arg \xi_1 = \arg \xi_2 - \theta$, other than a common phase of $e^{i\theta/2}$ for both fields, the whole system can be described by an equivalent overall Hamiltonian $\hat{H}_T = \hat{H}_{PA}(\xi_T) = \hat{H}_{PA}(\xi_1) + \hat{H}_{PA}(\xi'_2)$ with $\xi_T = \xi_1 + \xi'_2$. But if $\arg \xi_1 \neq \arg \xi_2 - \theta$, then $\hat{H}_T \neq \hat{H}_{PA}(\xi_1) + \hat{H}_{PA}(\xi'_2)$. This is because $e^{(1/i\hbar)\hat{H}_{PA}(\xi_1)t} e^{(1/i\hbar)\hat{H}_{PA}(\xi'_2)t} \neq e^{(1/i\hbar)[\hat{H}_{PA}(\xi_1) + \hat{H}_{PA}(\xi'_2)]t}$ if $[\hat{H}_{PA}(\xi_1), \hat{H}_{PA}(\xi'_2)] \neq 0$ when $\arg \xi_1 \neq \arg \xi_2 - \theta$.

This will have an inconvenient consequence when we extend the interferometer to multiple stages [43], [53], as shown in Fig.6.1. Because the phases in each stage are arbitrary, we therefore cannot write the overall Hamiltonian as the sum of each stage:

$$\hat{H}_T \neq \sum_j i\hbar(\xi'_j \hat{a}^\dagger \hat{b}^\dagger - \xi_j^* \hat{a} \hat{b}), \quad (4.5)$$

where the phase shifts at each stage are absorbed in the interaction parameter $\xi'_j = \xi_j e^{-i\theta_j}$.

To solve this problem, we can proceed by repeatedly using Eq.(4.4) to add each stage and obtain a recursive relation. Specifically for Eq.(4.4), we treat all the stage added up to stage k as the first PA with equivalent amplitude gains $G_T(k)$, $g_T(k)$ and the second PA is the $k + 1$ -th stage to be added:

$$\begin{aligned} G_T(k+1) &= G_T(k) G_{k+1} e^{i\theta_k/2} + g_T^*(k) g_{k+1} e^{-i\theta_k/2} \\ g_T(k+1) &= G_T^*(k) g_{k+1} e^{-i\theta_k/2} + g_T(k) G_{k+1} e^{i\theta_k/2}. \end{aligned} \quad (4.6)$$

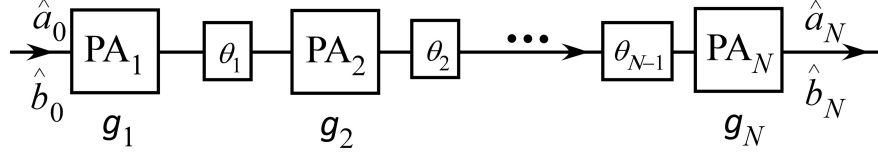


Figure 4.2. A multi-stage SU(1,1) interferometer (Adapted from Ref.[49]).

Unfortunately, we cannot find an analytical expression for the final outputs. In order to have some general idea about the outputs, we consider each stage has an infinitesimally small gain and phase shift whose sizes are proportional to an infinitesimal length scale Δx along the field propagation direction: $g_k \approx \zeta(x)\Delta x$, $\theta_k \approx \eta(x)\Delta x$ and we use location $x = k\Delta x$ to denote the k -th stage. When $\Delta x \rightarrow 0$, $G_{k+1} = \sqrt{1 + |g_{k+1}|^2} \approx 1 + o(\Delta x)$. So, Eq.(4.6) can be approximated as

$$\begin{aligned} G_T(x + \Delta x) &\approx G_T(x)(1 + i\eta\Delta x/2) + g_T^*(x)\zeta\Delta x \\ g_T(x + \Delta x) &\approx G_T^*(x)\zeta\Delta x + g_T(x)(1 + i\eta\Delta x/2). \end{aligned} \quad (4.7)$$

or

$$\begin{aligned} \frac{d}{dx}G_T(x) &= \zeta(x)g_T^*(x) + \frac{i\eta(x)}{2}G_T(x) \\ \frac{d}{dx}g_T(x) &= \zeta(x)G_T^*(x) + \frac{i\eta(x)}{2}g_T(x). \end{aligned} \quad (4.8)$$

These are the evolution equations for a PA with continuous gain function $\zeta(x)$. The phase parameter $\eta(x)$ usually corresponds to phase mismatching. The initial condition is obviously $G_T(0) = 1$, $g_T(0) = 0$. It is hard to analytically solve the differential equations if $\zeta(x)$, $\eta(x)$ depend on location x . For simplicity, let us assume ζ, η be constant. Then, Eq.(4.8) can be solved analytically and have the following solution:

If $\zeta \leq \eta/2$ and $\eta_0 \equiv \sqrt{\eta^2 - 4|\zeta|^2}$, we have

$$G_T(x) = \cos \frac{\eta_0 x}{2} + i \frac{\eta}{\eta_0} \sin \frac{\eta_0 x}{2}$$

$$g_T(x) = \frac{2\zeta}{\eta_0} \sin \frac{\eta_0 x}{2}. \quad (4.9)$$

If $\zeta \geq \eta/2$ and $\zeta_0 \equiv \sqrt{|\zeta|^2 - (\eta/2)^2}$, we have

$$\begin{aligned} G_T(x) &= \cosh(\zeta_0 x) + i \frac{\eta}{2\zeta_0} \sinh(\zeta_0 x) \\ g_T(x) &= \frac{\zeta}{\zeta_0} \sinh(\zeta_0 x). \end{aligned} \quad (4.10)$$

The exponential growth of the gain when $\zeta \geq \eta/2$ is typical of high gain PAs. But the oscillatory low gain behavior when $\zeta \leq \eta/2$ is the result of interference as we will see in the following.

In the limit of $\zeta \ll 1$, we have

$$\begin{aligned} G_T(x) &= e^{i\eta x/2}, \\ g_T(x) &= \zeta x \operatorname{sinc}(\eta x/2) \equiv e^{i\eta x/2} x \xi_T \\ &= e^{i\eta x/2} \int_0^x dx' \zeta e^{-i\eta x'}. \end{aligned} \quad (4.11)$$

The extra phase factor $e^{i\eta x/2}$ extracted out of g_T is for the consistency with G_T and is due to propagation of the fields through the system. The gain parameters in Eq.(4.11) are equivalent to an overall Hamiltonian of interaction parameter $\xi_T \equiv \zeta e^{-i\eta x/2} \operatorname{sinc}(\eta x/2)$ with evolution time t replaced by x :

$$\hat{H}_T = i\hbar(\xi_T \hat{a}^\dagger \hat{b}^\dagger - \xi_T^* \hat{a} \hat{b}), \quad (4.12)$$

which can thought of as the sum of all the stages:

$$\begin{aligned} \hat{H}_T &= \frac{1}{x} \int_0^x dx' i\hbar \zeta e^{-i\eta x'} \hat{a}^\dagger \hat{b}^\dagger + h.c. \\ &= \frac{1}{x} \int_0^x \hat{H}(d\xi'). \end{aligned} \quad (4.13)$$

Here, $d\xi' = \zeta e^{-i\eta x'} dx'$ is the infinitesimal gain parameter for each infinitesimal stage. Note that this equivalence is true only when $\zeta(x) = \text{constant}$ and $\eta(x) = \text{constant}$.

As a matter of fact, when gain parameters $|g_1|, |g_2| \ll 1$, we can add the two Hamiltonian to obtain overall Hamiltonian: $\hat{H}_T = \hat{H}_{PA}(\xi_T) = \hat{H}_{PA}(\xi_1) + \hat{H}_{PA}(\xi'_1)$. This can be seen from evolution operator

$$\begin{aligned}
\hat{U}_T &= \hat{U}_2(\xi_2)\hat{U}_1(\xi'_1) = e^{\hat{H}(\xi_2)\Delta x/i\hbar}e^{\hat{H}(\xi'_1)\Delta x/i\hbar} \\
&\approx [1 + \hat{H}(\xi_2)\Delta x/i\hbar][1 + \hat{H}(\xi'_1)\Delta x/i\hbar] \\
&\approx 1 + \hat{H}(\xi_2)\Delta x/i\hbar + \hat{H}(\xi'_1)\Delta x/i\hbar \\
&= 1 + \hat{H}_T\Delta x/i\hbar \approx e^{\hat{H}_T\Delta x/i\hbar},
\end{aligned} \tag{4.14}$$

Here, we assumed $|g_1| = |\xi_1|\Delta x \ll 1, |g_2| = |\xi'_1|\Delta x \ll 1$ and $\xi'_1 = \xi_1 e^{-i\theta}$ with phase shift $e^{-i\theta}$ included. So, when the amplitude gains $|g_j| \ll 1$, we can simply add the Hamiltonian of each stage:

$$\hat{H}_T = \sum_j i\hbar(\xi'_j \hat{a}^\dagger \hat{b}^\dagger - \xi_j^* \hat{a} \hat{b}) \tag{4.15}$$

and

$$g_T = \sum_k g'_k = \sum_k g_k e^{-i\theta_k}. \tag{4.16}$$

The above can also be thought of as a result of two-photon interference among the pair of photons generated by each stage [43], [53]. This can be confirmed by looking at the output state for vacuum input:

$$\begin{aligned}
|\Psi\rangle_T &= \hat{U}_T|0\rangle \\
&\approx |0\rangle + (\sum_k g'_k)|1_a, 1_b\rangle \\
&= |0\rangle + \sum_k |\Psi\rangle_k
\end{aligned} \tag{4.17}$$

with $|\Psi\rangle_k$ as the two-photon state generated by the k -th stage.

Notice that Eq.(4.15) is true only if the overall amplitude gain g_T is much smaller than 1 so that the last step of Eq.(4.14) stands. For the high gain case, Eq.(4.15) does not stand

and we have to resort to Eq.(4.6) or Eq.(4.10). This will pose a serious problem in finding a solution for a broad band PA in the high gain regime.

4.2 Broadband Parametric Amplifier

When parametric processes are pumped by high power pulses, broadband parametric amplification is achieved. They can be used to produce quantum entangled fields with a wide bandwidth. The traditional treatment of this situation is to start with a multi-mode Hamiltonian of the form [15], [46]

$$\begin{aligned} \hat{H}_M = & \chi \int d\omega_1 d\omega_2 d\omega_3 \Psi(\omega_1, \omega_2, \omega_3) \hat{a}^\dagger(\omega_1) \hat{b}^\dagger(\omega_2) \\ & \times A_p(\omega_3) e^{i(\omega_1 + \omega_2 - \omega_3)t} + h.c., \end{aligned} \quad (4.18)$$

where subscript ‘‘M’’ denotes multi-mode, χ is some parameter proportional to the nonlinear coefficient of nonlinear medium of length L_0 , $A_p(\omega_3)$ is the spectral amplitude of the pump field, and $\Psi(\omega_1, \omega_2, \omega_3)$ is obtained from spatial integration:

$$\Psi(\omega_1, \omega_2, \omega_3) \equiv \int_0^{L_0} dz e^{-iz\Delta k} = L_0 \frac{\sin \beta}{\beta} e^{-i\beta} \quad (4.19)$$

with $\beta \equiv \Delta k L_0 / 2$ and $\Delta k \equiv k_1 + k_2 - k_3$ as the phase mismatch. We then find evolution operator as

$$\hat{U} = \exp \left\{ \frac{1}{i\hbar} \int_{-\infty}^{\infty} dt \hat{H}_M \right\} \quad (4.20)$$

where time integration gives rise to a delta-function $\delta(\omega_1 + \omega_2 - \omega_3)$ and the integrated Hamiltonian has the form of

$$\int dt \hat{H}_M = i\hbar G \int d\omega_1 d\omega_2 \Phi(\omega_1, \omega_2) \hat{a}^\dagger(\omega_1) \hat{b}^\dagger(\omega_2) + h.c., \quad (4.21)$$

with $G \equiv \chi/C$ as a dimensionless gain parameter such that

$$\Phi(\omega_1, \omega_2) \equiv 2\pi CL_0 \frac{\sin \beta}{\beta} e^{-i\beta} A_p(\omega_1 + \omega_2) \quad (4.22)$$

is normalized: $\int d\omega_1 d\omega_2 |\Phi(\omega_1, \omega_2)|^2 = 1$. In general, this gives rise to a complicated coupling of different frequency components at the outputs:

$$\hat{a}^{(o)}(\omega_1) = \hat{U}^\dagger \hat{a}(\omega_1) \hat{U} = \int h_{1a}(\omega_1, \omega'_1) \hat{a}(\omega'_1) d\omega'_1 + \int h_{2a}(\omega_1, \omega'_2) \hat{b}^\dagger(\omega'_2) d\omega'_2 \quad (4.23)$$

$$\hat{b}^{(o)}(\omega_2) = \hat{U}^\dagger \hat{b}(\omega_2) \hat{U} = \int h_{1b}(\omega_2, \omega'_2) \hat{b}(\omega'_2) d\omega'_2 + \int h_{2b}(\omega'_1, \omega_2) \hat{a}^\dagger(\omega'_1) d\omega'_1, \quad (4.24)$$

where $\hat{a}^{(o)}, \hat{b}^{(o)}$ are the outputs at the end of nonlinear medium and $\hat{a}(\omega_1), \hat{b}(\omega_2)$ are those at the start. But we can make a singular value decomposition of the JSF $\Phi(\omega_1, \omega_2)$:

$$\Phi(\omega_1, \omega_2) = \sum_k r_k \psi_k(\omega_1) \varphi_k(\omega_2), \quad (4.25)$$

where $\{\psi_k, \phi_k\}$ are two sets of ortho-normal functions: $\int d\omega_1 \psi_j^*(\omega_1) \psi_k(\omega_1) = \int d\omega_2 \varphi_j^*(\omega_2) \varphi_k(\omega_2) = \delta_{jk}$ and $\{r_k\}$ are non-negative numbers satisfying $\sum_k r_k^2 = 1$. Then Eq.(4.21) becomes

$$\int dt \hat{H}_M = i\hbar G \sum_k r_k \hat{A}_k^\dagger \hat{B}_k^\dagger + h.c. \quad (4.26)$$

with $\hat{A}_k \equiv \int d\omega_1 \psi_j^*(\omega_1) \hat{a}(\omega_1)$, $\hat{B}_k \equiv \int d\omega_2 \varphi_j^*(\omega_2) \hat{b}(\omega_2)$ satisfying $[\hat{A}_j, \hat{A}_k^\dagger] = \delta_{jk} = [\hat{B}_j, \hat{B}_k^\dagger]$. Together with Eq.(4.20), this leads to de-coupling of the different TMs \hat{A}_k and \hat{B}_k for the two output fields:

$$\begin{aligned} \hat{A}_k^{(o)} &= \cosh(r_k G) \hat{A}_k + \sinh(r_k G) \hat{B}_k^\dagger, \\ \hat{B}_k^{(o)} &= \cosh(r_k G) \hat{B}_k + \sinh(r_k G) \hat{A}_k^\dagger, \end{aligned} \quad (4.27)$$

Unfortunately, it was pointed out [41] that the evolution operator in Eq.(4.20) is not correct for the Hamiltonian in Eq.(4.18) because $[\hat{H}_M(t), \hat{H}_M(t')] \neq 0$ for $t \neq t'$. The reason

is the same as those for Eq.(4.1). But Eqs.(4.23,4.24) are still correct for the Hamiltonian in Eq.(4.18).

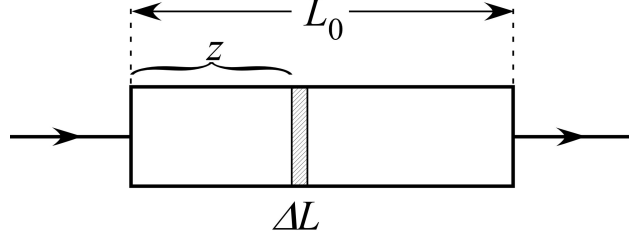


Figure 4.3. A PA from a single-pass pulse-pumped nonlinear medium (Adapted from Ref.[49]).

In order to treat this in a correct manner, we can apply the same approach in the previous section. Consider a nonlinear medium of length L which is divided into a small segment of size ΔL , as shown in Fig.4.3. Let us treat the small segment first. The Hamiltonian is given from Eq.(4.18) for the small segment as

$$\hat{H}(z, \Delta L) = \chi \int d\omega_1 d\omega_2 d\omega_3 \int_z^{z+\Delta L} dz' e^{-iz'\Delta k} \hat{a}^\dagger(\omega_1, z) \times \hat{b}^\dagger(\omega_2, z) A_p(\omega_3) e^{i(\omega_1+\omega_2-\omega_3)t} + h.c., \quad (4.28)$$

where the spatial integration starts at z instead of 0 because the ΔL segment is located at z inside the medium and we assume that there is no pump depletion. For $\Delta L = dL \rightarrow 0$, we have

$$\hat{H}(z, dL) = \chi dL \int d\omega_1 d\omega_2 d\omega_3 e^{-iz\Delta k} \hat{a}^\dagger(\omega_1, z) \hat{b}^\dagger(\omega_2, z) \times A_p(\omega_3) e^{i(\omega_1+\omega_2-\omega_3)t} + h.c. + o(dL). \quad (4.29)$$

The evolution operator for this segment is given by the Dyson series:

$$\hat{U}(z, \Delta L) = 1 + \sum_{n=1} \hat{U}_n \quad (4.30)$$

with

$$\begin{aligned} \hat{U}_n &= \left(\frac{1}{i\hbar}\right)^n \int_{-\infty}^{\infty} dt_1 \int_{-\infty}^{t_1} dt_2 \dots \int_{-\infty}^{t_{n-1}} dt_n \\ &\quad \times \hat{H}(z, dL, t_1) \dots \hat{H}(z, dL, t_n). \end{aligned} \quad (4.31)$$

Eq.(4.30) becomes Eq.(4.20) if $[\hat{H}(z, dL, t_1), \hat{H}(z, dL, t_2)] = 0$ but it is not true for $\hat{H}(z, dL)$ in Eq.(4.29). On the other hand, for $dL \rightarrow 0$, we have

$$\hat{U}(z, dL) = 1 + \hat{U}_1 + o(dL) \approx 1 + \int dt \hat{H}(z, dL). \quad (4.32)$$

So, we obtain the evolution of the field operators:

$$\begin{aligned} \hat{a}(\omega_1, z + dL) &= \hat{U}^\dagger(z, dL) \hat{a}(\omega_1, z) \hat{U}(z, dL) \\ &= \hat{a}(\omega_1, z) + [\hat{a}(\omega_1, z), \int dt \hat{H}(z, dL)] \\ &= \hat{a}(\omega_1, z) + 2\pi\chi dL \int d\omega_2 \hat{b}^\dagger(\omega_2, z) \\ &\quad \times e^{-iz\Delta k} A_p(\omega_1 + \omega_2), \end{aligned} \quad (4.33)$$

where the time integral gives rise to a δ -function for $\omega_1 + \omega_2 - \omega_3$ and $\Delta k = \Delta k|_{\omega_3=\omega_1+\omega_2}$.

With $d\hat{a}(\omega_1, z)/dz = [\hat{a}(\omega_1, z + dL) - \hat{a}(\omega_1, z)]/dL$, we have

$$\frac{d}{dz} \hat{a}(\omega_1, z) = 2\pi\chi \int d\omega_2 e^{-iz\Delta k} A_p(\omega_1 + \omega_2) \hat{b}^\dagger(\omega_2, z). \quad (4.34)$$

Likewise, we obtain

$$\frac{d}{dz} \hat{b}(\omega_2, z) = 2\pi\chi \int d\omega_1 e^{-iz\Delta k} A_p(\omega_1 + \omega_2) \hat{a}^\dagger(\omega_1, z). \quad (4.35)$$

Note that Eqs.(4.34,4.35) are in a similar form as those derived in Refs.[45],[54] with different methods. Using the input-output relation in Eq.(4.23) at location z , we obtain

$$\begin{aligned}\frac{d}{dz}h_{1a}(\omega_1, \omega'_1, z) &= \int d\omega_2 f(\omega_1, \omega_2) h_{2b}^*(\omega'_1, \omega_2, z) \\ \frac{d}{dz}h_{2b}(\omega'_1, \omega_2, z) &= \int d\omega_1 f(\omega_1, \omega_2) h_{1a}^*(\omega_1, \omega'_1, z),\end{aligned}\quad (4.36)$$

and

$$\begin{aligned}\frac{d}{dz}h_{1b}(\omega_2, \omega'_2, z) &= \int d\omega_1 f(\omega_1, \omega_2) h_{2a}^*(\omega_1, \omega'_2, z) \\ \frac{d}{dz}h_{2a}(\omega_1, \omega'_2, z) &= \int d\omega_2 f(\omega_1, \omega_2) h_{1b}^*(\omega_2, \omega'_2, z),\end{aligned}\quad (4.37)$$

where $f(\omega_1, \omega_2) \equiv 2\pi\chi e^{-iz\Delta k} A_p(\omega_1 + \omega_2)$. Since we have $\hat{a}^{(o)}(\omega_1, z = 0) = \hat{a}(\omega_1)$ and $\hat{b}^{(o)}(\omega_2, z = 0) = \hat{b}(\omega_2)$ at the start, the initial condition is

$$\begin{aligned}h_{1a}(\omega_1, \omega'_1, z = 0) &= \delta(\omega_1 - \omega'_1) \\ h_{1b}(\omega_2, \omega'_2, z = 0) &= \delta(\omega_2 - \omega'_2) \\ h_{2a}(\omega_1, \omega'_2, z = 0) &= 0 \\ h_{2b}(\omega_2, \omega'_1, z = 0) &= 0.\end{aligned}\quad (4.38)$$

From Eqs.(4.36,4.37) and initial conditions in Eq.(4.38), we can verify that

$$\begin{aligned}&\int d\omega'_1 h_{1a}(\omega_1, \omega'_1, z) h_{1a}^*(\bar{\omega}_1, \omega'_1, z) \\ &\quad - \int d\omega'_2 h_{2a}(\omega_1, \omega'_2, z) h_{2a}^*(\bar{\omega}_1, \omega'_2, z) = \delta(\omega_1 - \bar{\omega}_1), \\ &\int d\omega'_2 h_{1b}(\omega_2, \omega'_2, z) h_{1b}^*(\bar{\omega}_2, \omega'_2, z) \\ &\quad - \int d\omega'_1 h_{2b}(\omega'_1, \omega_2, z) h_{2b}^*(\omega'_1, \bar{\omega}_2, z) = \delta(\omega_2 - \bar{\omega}_2), \\ &\int d\omega'_1 h_{1a}(\omega_1, \omega'_1, z) h_{2b}(\omega'_1, \bar{\omega}_2, z) \\ &\quad - \int d\omega'_2 h_{1b}(\bar{\omega}_2, \omega'_2, z) h_{2a}(\omega_1, \omega'_2, z) = 0,\end{aligned}\quad (4.39)$$

These relations guarantee the commutation relations $[\hat{a}^{(o)}(\omega_1), \hat{a}^{(o)\dagger}(\bar{\omega}_1)] = \delta(\omega_1 - \bar{\omega}_1)$, $[\hat{b}^{(o)}(\omega_2), \hat{b}^{(o)\dagger}(\bar{\omega}_2)] = \delta(\omega_2 - \bar{\omega}_2)$, $[\hat{a}^{(o)}(\omega_1), \hat{b}^{(o)}(\bar{\omega}_2)] = 0$ from Eq.(4.23).

4.3 Eigen-modes of High Gain Parametric Processes

Although h -functions have very complicated form, we can in general use singular value decomposition method to decompose them as

$$\begin{aligned}
h_{1a}(\omega, \omega') &= \sum_k r_{1a}^{(k)} \psi_{1a}^{(k)}(\omega) \phi_{1a}^{(k)}(\omega') \\
h_{2a}(\omega, \omega') &= \sum_k r_{2a}^{(k)} \psi_{2a}^{(k)}(\omega) \phi_{2a}^{(k)}(\omega') \\
h_{1b}(\omega, \omega') &= \sum_k r_{1b}^{(k)} \psi_{1b}^{(k)}(\omega) \phi_{1b}^{(k)}(\omega') \\
h_{2b}(\omega, \omega') &= \sum_k r_{2b}^{(k)} \psi_{2b}^{(k)}(\omega) \phi_{2b}^{(k)}(\omega').
\end{aligned} \tag{4.40}$$

Because of relations in Eq.(4.39), it can be shown (see Appendix 4.A) that $\psi_{1a}^{(k)}(\omega) = \psi_{2a}^{(k)}(\omega) \equiv \psi_k^{(a)}(\omega)$, $\psi_{1b}^{(k)}(\omega) = \psi_{2b}^{(k)}(\omega) \equiv \psi_k^{(b)}(\omega)$, $\phi_{1a}^{(k)}(\omega') = \phi_{2b}^{(k)*}(\omega') \equiv \phi_k^{(a)}(\omega')$, $\phi_{1b}^{(k)}(\omega') = \phi_{2a}^{(k)*}(\omega') \equiv \phi_k^{(b)}(\omega')$, and $r_{1a}^{(k)} = r_{1b}^{(k)} \equiv \cosh r_k G$, $r_{2a}^{(k)} = r_{2b}^{(k)} = \sqrt{r_{1a}^{(k)2} - 1} = \sinh r_k G$. Here, $\psi_k^{(a)}(\omega)$, $\phi_k^{(a)}(\omega)$, $\psi_k^{(b)}(\omega)$, $\phi_k^{(b)}(\omega)$ are four sets of orthonormal mode functions satisfying $\int d\omega \psi_k^{(a,b)*}(\omega) \psi_{k'}^{(a,b)}(\omega) = \delta_{kk'}$, $\int d\omega \phi_k^{(a,b)*}(\omega) \phi_{k'}^{(a,b)}(\omega) = \delta_{kk'}$ and r_k 's are normalized mode coefficients satisfying $\sum_k r_k^2 = 1$ with G being some parameter depending on χ . So, h -functions are in the form of

$$\begin{aligned}
h_{1a}(\omega_1, \omega'_1, z) &= \sum_k \cosh(r_k G) \psi_k^{(a)}(\omega_1) \phi_k^{(a)}(\omega'_1), \\
h_{2a}(\omega_1, \omega'_2, z) &= \sum_k \sinh(r_k G) \psi_k^{(a)}(\omega_1) \phi_k^{(b)*}(\omega'_2), \\
h_{1b}(\omega_2, \omega'_2, z) &= \sum_k \cosh(r_k G) \psi_k^{(b)}(\omega_2) \phi_k^{(b)}(\omega'_2), \\
h_{2b}(\omega_1, \omega'_2, z) &= \sum_k \sinh(r_k G) \psi_k^{(b)}(\omega_1) \phi_k^{(a)*}(\omega'_2).
\end{aligned} \tag{4.41}$$

With these relations and orthonormal relations for $\psi_k^{(a,b)}(\omega)$, Eqs.(4.23,4.24) can be recast as

$$\begin{aligned}
\hat{A}_k^{(o)} &= \cosh(r_k G) \hat{A}_k + \sinh(r_k G) \hat{B}_k^\dagger, \\
\hat{B}_k^{(o)} &= \cosh(r_k G) \hat{B}_k + \sinh(r_k G) \hat{A}_k^\dagger,
\end{aligned} \tag{4.42}$$

where $\hat{A}_k^{(o)} \equiv \int d\omega \psi_k^{(a)*} \hat{a}^{(o)}(\omega)$, $\hat{B}_k^{(o)} \equiv \int d\omega \psi_k^{(b)*} \hat{b}^{(o)}(\omega)$, $\hat{A}_k \equiv \int d\omega \phi_k^{(a)} \hat{a}(\omega)$, $\hat{B}_k \equiv \int d\omega \phi_k^{(b)} \hat{b}(\omega)$ define the annihilation operators for the corresponding output and input TMs, similar to those given in Eq.(4.27). Because of orthonormal relations, they satisfy the Boson commutation relation for annihilation operators.

Because of the δ -function in the initial conditions in Eq.(4.38), we cannot solve directly the differential-integral equations in Eqs.(4.36,4.37). In order to proceed, let us write $\bar{h}_{1a}(\omega_1, \omega'_1, z) \equiv h_{1a}(\omega_1, \omega'_1, z) - \delta(\omega_1 - \omega'_1)$ and $\bar{h}_{1b}(\omega_1, \omega'_1, z) \equiv h_{1b}(\omega_1, \omega'_1, z) - \delta(\omega_1 - \omega'_1)$. Furthermore, for a specific parametric process from four-wave mixing in optical fiber with a Gaussian pumping profile, we have $A_p(\omega_3) = A_0^2 \exp[-(\omega_3 - 2\omega_{p0})^2/4\sigma_p^2]$ with pump bandwidth of σ_p and pump amplitude A_0 [55]. We can introduce some new dimensionless variables: $\zeta \equiv z/L_0$, $\Omega_j \equiv (\omega_j - \omega_{j0})/\sigma_p$ ($j = 1, 2$) with L_0 as the length of the nonlinear medium, and ω_{j0} ($j = 1, 2, p$) as the central frequency of the corresponding fields. Then, we can make Eqs.(4.36,4.37) dimensionless as

$$\begin{aligned} \frac{d}{d\zeta} \bar{h}_{1a}(\Omega_1, \Omega'_1, \zeta) &= \int d\Omega_2 f(\Omega_1, \Omega_2, \zeta) h_{2b}^*(\Omega'_1, \Omega_2, \zeta) \\ \frac{d}{d\zeta} h_{2b}(\Omega'_1, \Omega_2, \zeta) &= f(\Omega'_1, \Omega_2, \zeta) \\ &+ \int d\Omega_1 f(\Omega_1, \Omega_2, \zeta) \bar{h}_{1a}^*(\Omega_1, \Omega'_1, \zeta), \end{aligned} \quad (4.43)$$

and

$$\begin{aligned} \frac{d}{d\zeta} \bar{h}_{1b}(\Omega_2, \Omega'_2, \zeta) &= \int d\Omega_1 f(\Omega_1, \Omega_2, \zeta) h_{2a}^*(\Omega_1, \Omega'_2, \zeta) \\ \frac{d}{d\zeta} h_{2a}(\Omega_1, \Omega'_2, \zeta) &= f(\Omega_1, \Omega'_2, \zeta) \\ &+ \int d\Omega_2 f(\Omega_1, \Omega_2, \zeta) \bar{h}_{1b}^*(\Omega_2, \Omega'_2, \zeta), \end{aligned} \quad (4.44)$$

where $f(\Omega_1, \Omega_2, \zeta) \equiv K e^{-i\zeta \Delta k L_0} \exp[-(\Omega_1 + \Omega_2)^2/4]$ with $K \equiv 2\pi L_0 A_0^2 \sigma_p \chi$ as the dimensionless pump parameter and $h(\Omega_1, \Omega_2)$ -functions are dimensionless and is related to $h(\omega)$ -functions by $h(\Omega_1, \Omega_2) \equiv \sigma_p h(\omega_1, \omega_2)$. Phase mismatch $\Delta k L_0$ can be adjusted according to the dispersion of the nonlinear medium and in general has a linear form of $\Delta k L_0 =$

$\Omega_1/\Delta_1 + \Omega_2/\Delta_2$ with parameters Δ_1, Δ_2 determined by medium dispersion, pump bandwidth σ_p , and medium length L_0 . The initial conditions in Eq.(4.38) change to

$$\begin{aligned}
\bar{h}_{1a}(\Omega_1, \Omega'_1, \zeta = 0) &= 0 \\
\bar{h}_{1b}(\Omega_2, \Omega'_2, \zeta = 0) &= 0 \\
h_{2a}(\Omega_1, \Omega'_2, \zeta = 0) &= 0 \\
h_{2b}(\Omega'_1, \Omega_2, \zeta = 0) &= 0.
\end{aligned} \tag{4.45}$$

Note that when pump parameter is small: $K \ll 1$, $h_{2a}(\Omega_1, \Omega_2)$ has an approximate analytical solution:

$$\begin{aligned}
h_{2a}(\Omega_1, \Omega_2, \zeta = 1) &\approx K e^{-i\Delta k L_0/2} \text{sinc}(\Delta k L_0/2) \\
&\times \exp\left[-(\Omega_1 + \Omega_2)^2/4\right],
\end{aligned} \tag{4.46}$$

which is exactly the JSF $\Phi(\omega_1, \omega_2)$ in Eq.(4.22) after changing to dimensionless quantities. But for a sizable K , we cannot solve the differential-integral equations in Eqs.(4.43,4.44) analytically. Next, we will solve them numerically, subject to initial conditions in Eq.(4.45).

4.4 Numerical Solutions

Let us use a nonlinear fiber as the nonlinear medium. We use the parameters similar to those given in Ref.[17] for a real piece of 300m-long dispersion-shifted nonlinear fiber. We obtain the dimensionless parameters $1/\Delta_1 = 0.785, 1/\Delta_2 = -0.471$. The numerical solution of the amplitude of $h_{2a}(\Omega_1, \Omega_2)$ is shown in Fig.4.4 for four values of pump parameter K : $K = 0.01, 2, 4, 10$. For small $K (\ll 1, \text{ Fig.4.4(a)})$, $h_{2a}(\Omega_1, \Omega_2)$ is exactly the JSF $\Phi(\omega_1, \omega_2)$ given in Eq.(4.22), similar to Fig.2(a) of Ref.[17]. The shape starts to broaden as K increases. This can be seen in the profile change of the eigen-function $\psi_1^{(a)}(\Omega_1)$ obtained from singular value decomposition when we plot it in Fig.4.5 for four values of K (0.01, 2, 4, 10). To show the trend, we plot the full width at half maximum (FWHM) of $|\psi_1^{(a)}(\Omega_1)|$ as a function of K in the inset of Fig.4.5.

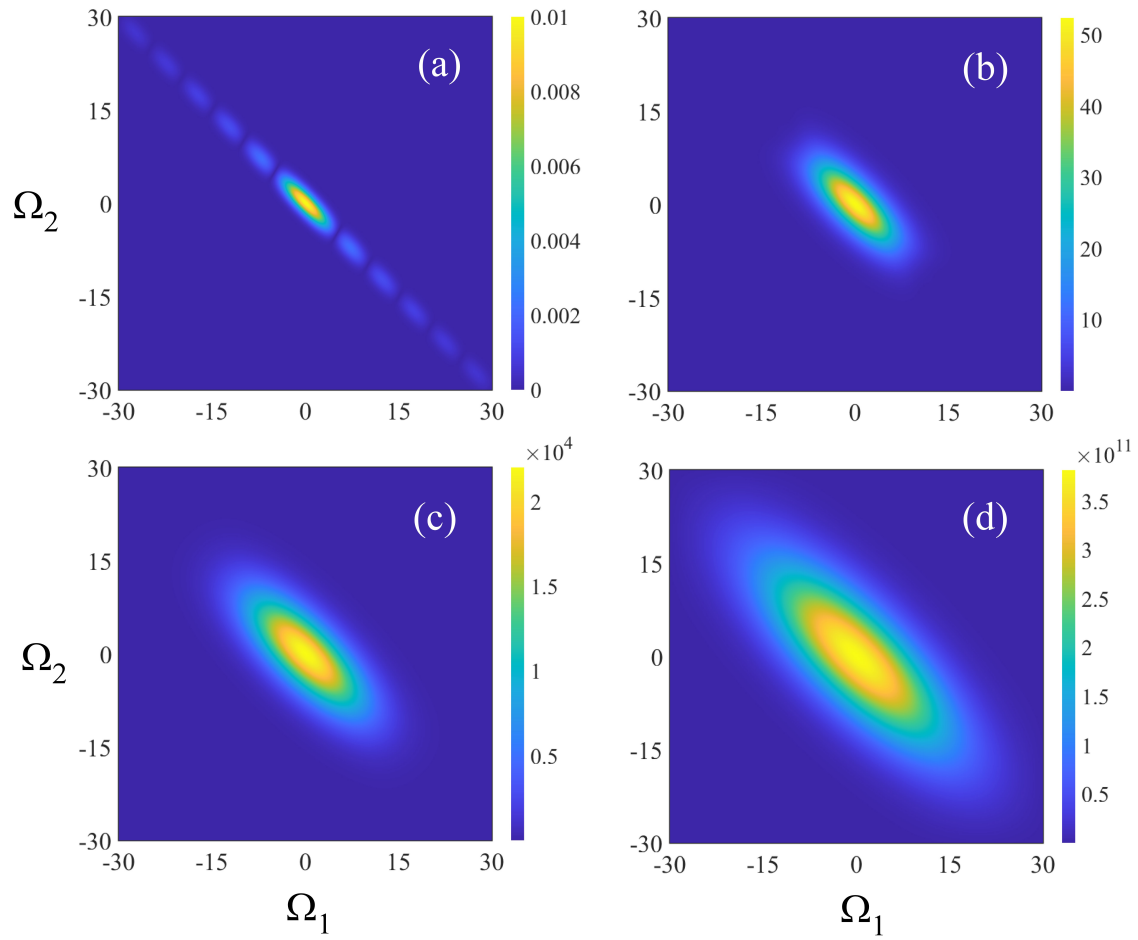


Figure 4.4. Contour plot of the amplitude of $h_{2a}(\Omega_1, \Omega_2)$ for $K =$ (a) 0.01, (b) 2, (c) 4, (d) 10. $\Omega_i \equiv (\omega_i - \omega_{i0})/\sigma_p$ ($i = 1, 2$) (Adapted from Ref.[49]).

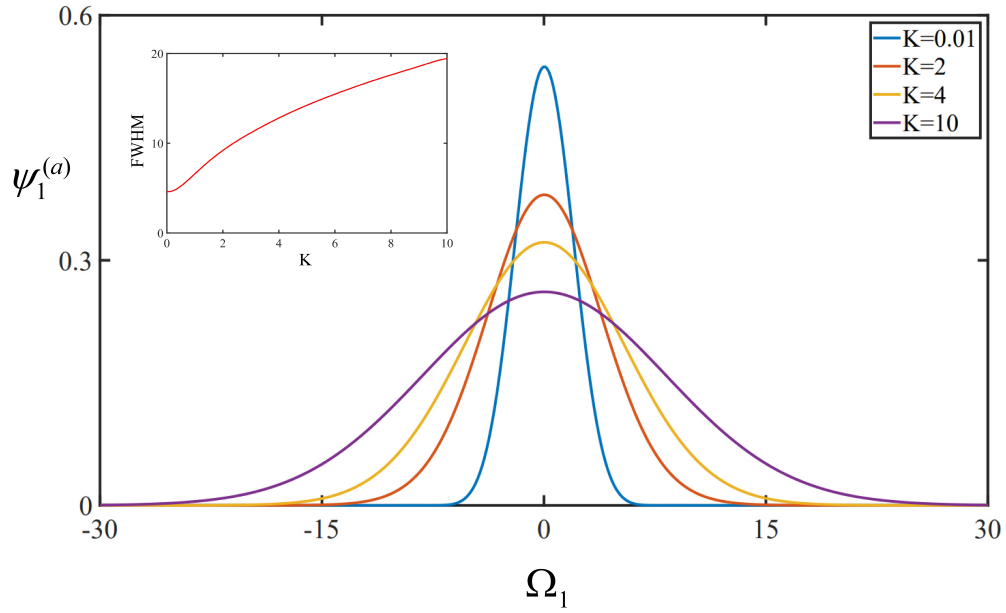


Figure 4.5. The amplitude function $\psi_1^{(a)}$ of mode 1 for pump parameter $K = 0.01, 2, 4, 10$, showing the broadening of the width. Inset: the full width at half maximum (FWHM) of mode 1 function as a function of the pump parameter K (Adapted from Ref.[49]).

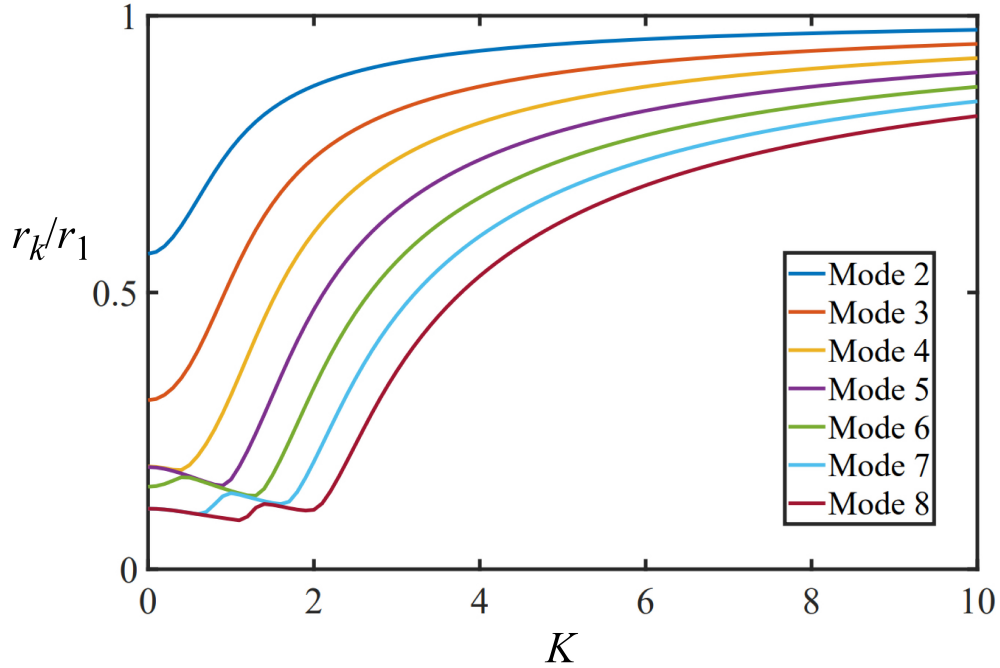


Figure 4.6. Mode coefficients r_k/r_1 as a function of dimensionless pump parameter K (Adapted from Ref.[49]).

The change of the transfer function $h_{2a}(\Omega_1, \Omega_2)$ with pump parameter K will lead to mode structure change. This is reflected in the change of the distribution of the mode coefficients $\{r_k\}$, whose normalized values to r_1 are plotted in Fig.4.6 as a function of the pump parameter K . The trend shows the increasing weight of the higher order modes in addition to the broadening of the mode functions as K increases.

The multi-mode nature and the broadening of the mode functions with pump parameter K are due to the values of Δ_1, Δ_2 in $\Delta k L_0$ for a realistic nonlinear fiber case, which gives rise to an asymmetric sinc-function in Φ of Eq.(4.22) or $h_{2a}(\Omega_1, \Omega_2)$ at small K (Fig.4.4(a)). In principle, we can adjust the dispersion parameters of the fiber to change Δ_1, Δ_2 in $\Delta k L_0$. It is found that the initial $h_{2a}(\Omega_1, \Omega_2)$ when $K \ll 1$ is nearly round or factorized with parameters $1/\Delta_1 = 2.198, 1/\Delta_2 = -2.198$, as shown in $h_{2a}(\Omega_1, \Omega_2)$ in Fig.4.7(a). The initial r_k distribution is indeed close to single mode with high order r_k much smaller than 1. This can be seen in Fig.4.8 for $K = 0$. However, the trend of mode spreading for large K in Fig.4.6 persists in Fig.4.8.

On the other hand, a close look at Fig.4.7(c,d) for large K shows that the function h_{2a} is still pretty round or nearly single mode. In fact, we find from mode decomposition in Eq.(4.41) that the coefficient of each mode is $\sinh^2(r_k G)$, which becomes $0.25e^{2r_k G}$ for large $r_k G$. So, the ratio of coefficients of the first mode to higher mode is then $e^{2(r_1 - r_k)G} \gg 1$ for large G , that is, the first mode will dominate in the mode decomposition in Eq.(4.41) at large K (or G) [56], which leads to a nearly round (or factorized) h_{2a} .

Furthermore, we can look at the mode purity of the output state. It is known that if we discard the other field, one of the output fields from a PA is in a thermal state. For broadband pulsed pumping, it becomes a multi-mode thermal field. Mode purity for a pulsed multi-mode thermal field was studied in Ref.Su2019PRA with the TM format described here. It was found that mode purity can be characterized by the normalized intensity correlation function $g^{(2)}$ defined as

$$\begin{aligned} g^{(2)} &\equiv \frac{\langle I^2 \rangle}{\langle I \rangle^2} \equiv 1 + \frac{1}{M} \\ &= 1 + \frac{\sum_k I_k^2}{(\sum_k I_k)^2}, \end{aligned} \quad (4.47)$$

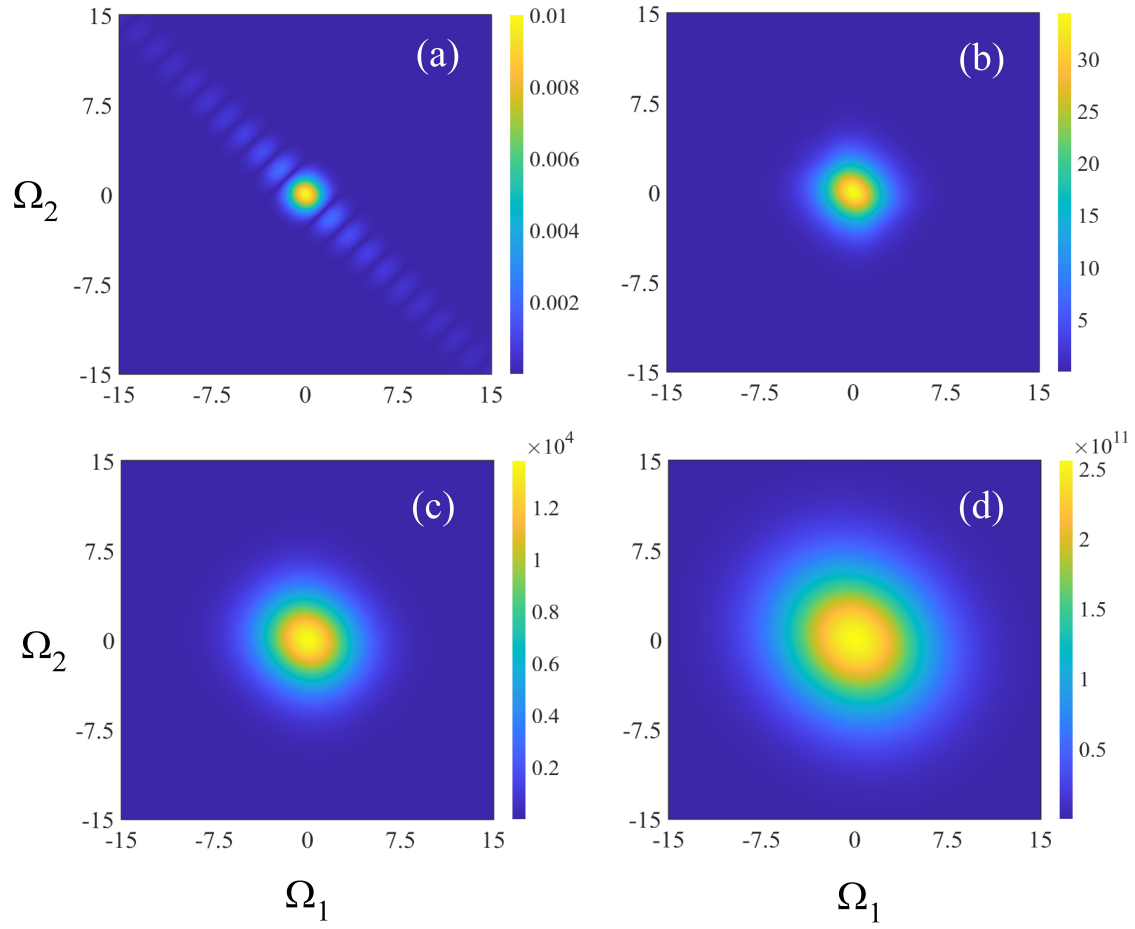


Figure 4.7. Contour plot of the amplitude of $h_{2a}(\Omega_1, \Omega_2)$ for the case of $1/\Delta_1 = 2.198, 1/\Delta_2 = -2.198$ with $K =$ (a) 0.01, (b) 2, (c) 4, (d) 10. $\Omega_i \equiv (\omega_i - \omega_{i0})/\sigma_p (i = 1, 2)$ (Adapted from Ref.[49]).

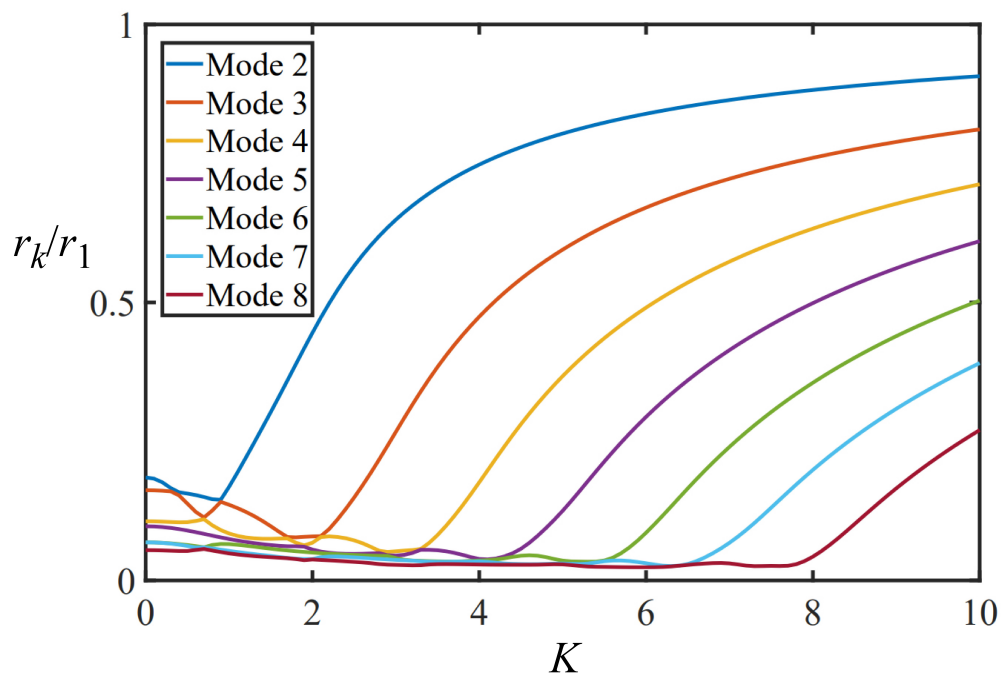


Figure 4.8. Mode coefficients r_k/r_1 as a function of dimensionless pump parameter K for the nearly factorized case of $1/\Delta_1 = 2.198, 1/\Delta_2 = -2.198$ (Adapted from Ref.[49]).

where M is defined as the number of modes ($M = 1$ gives the pure single-mode case) and I_k is the intensity of mode k . From Eq.(4.42), we find that $I_k = \sinh^2(r_k G)$ for vacuum input to the PA. So, Eq.(4.47) becomes

$$M = \frac{[\sum_k \sinh^2(r_k G)]^2}{\sum_k \sinh^4(r_k G)}. \quad (4.48)$$

Obviously, for the single mode case with $r_1 = 1, r_k = 0$ ($k > 1$), we have $M = 1$. Equation (4.48) was first derived by Christ *et al.* [15] for TMs and by Sharapova *et al.* [57] and Dyakonov *et al.* [58] for spatial modes in high gain parametric processes. For the two cases shown in Fig.4.4 and Fig.4.7, we evaluate mode number M in Eq.(4.48) as a function of pump parameter K and plot the results in Fig.4.9. It can be seen that mode number M indeed drops first as K increases. This drop is consistent with the dominance of the first mode as K increases. However, the drop stops at around $K = 2$ when a minimum of M is reached. M starts to slowly increase after $K > 2$. This is due to the increase of r_k for higher order modes as K increases, as shown in Fig.4.6 and Fig.4.8. The minimum M value depends on the initial M at low K ($\ll 1$). Thus, it is better to have a nearly single mode situation at low pump power.

4.A Appendix

In general, we can use singular value decomposition to write

$$\begin{aligned} h_{1a}(\omega, \omega') &= \sum_k r_{1a}^{(k)} \psi_{1a}^{(k)}(\omega) \phi_{1a}^{(k)}(\omega') \\ h_{2a}(\omega, \omega') &= \sum_k r_{2a}^{(k)} \psi_{2a}^{(k)}(\omega) \phi_{2a}^{(k)}(\omega') \\ h_{1b}(\omega, \omega') &= \sum_k r_{1b}^{(k)} \psi_{1b}^{(k)}(\omega) \phi_{1b}^{(k)}(\omega') \\ h_{2b}(\omega, \omega') &= \sum_k r_{2b}^{(k)} \psi_{2b}^{(k)}(\omega) \phi_{2b}^{(k)}(\omega') \end{aligned} \quad (4.49)$$

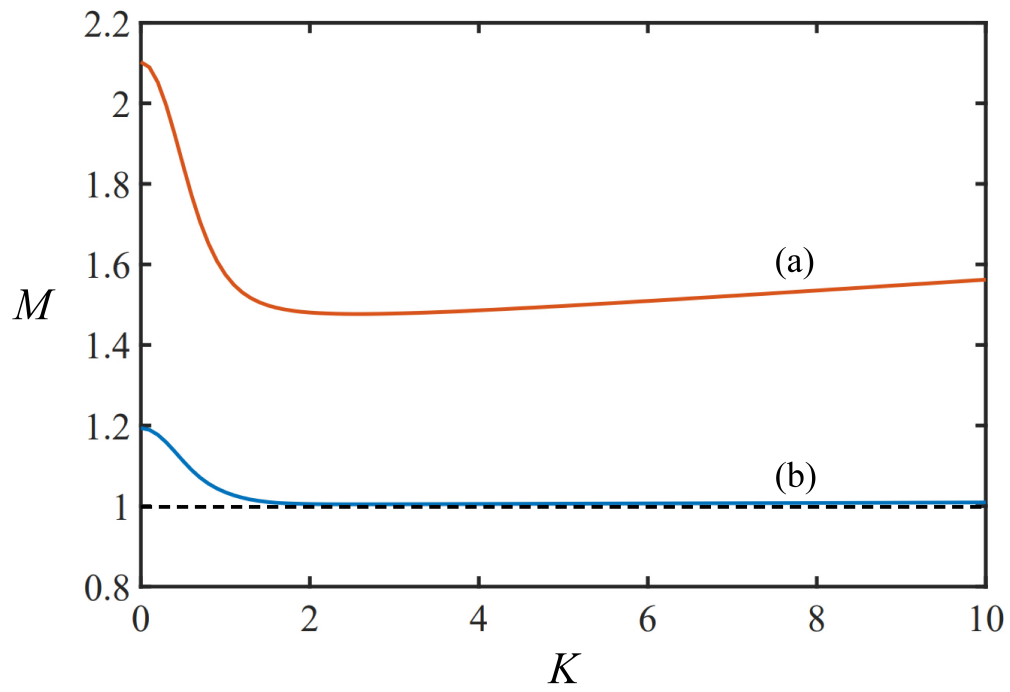


Figure 4.9. Mode number M as a function of pump parameter K for the cases shown in Fig.4.4 (orange, (a)) and Fig.4.7 (blue, (b)). The dashed line corresponds to $M = 1$ (Adapted from Ref.[49]).

where $\psi_{1a}^{(k)}(\omega), \phi_{1a}^{(k)}(\omega')$ etc. are 8 sets of orthonormal mode functions satisfying $\int d\omega \psi_{1a}^{(k)}(\omega) \psi_{1a}^{(k')*}(\omega) = \delta_{k,k'}$, etc. Using the decomposition in Eq.(4.49) and orthonormal relations, we write the left hand side of the first relation in Eq.(4.39) as

$$\begin{aligned}
& \int d\omega'' h_{1a}(\omega, \omega'') h_{1a}^*(\omega', \omega'') \\
& \quad - \int d\omega'' h_{2a}(\omega, \omega'') h_{2a}^*(\omega', \omega'') \\
& = \int d\omega'' \sum_{k,k'} r_{1a}^{(k)} r_{1a}^{(k')} \psi_{1a}^{(k)}(\omega) \psi_{1a}^{(k')*}(\omega') \phi_{1a}^{(k)}(\omega'') \phi_{1a}^{(k')*}(\omega'') \\
& \quad - \int d\omega'' \sum_{k,k'} r_{2a}^{(k)} r_{2a}^{(k')} \psi_{2a}^{(k)}(\omega) \psi_{2a}^{(k')*}(\omega') \phi_{2a}^{(k)}(\omega'') \phi_{2a}^{(k')*}(\omega'') \\
& = \sum_{k,k'} r_{1a}^{(k)} r_{1a}^{(k')} \psi_{1a}^{(k)}(\omega) \psi_{1a}^{(k')*}(\omega') \delta_{k,k'} \\
& \quad - \sum_{k,k'} r_{2a}^{(k)} r_{2a}^{(k')} \psi_{2a}^{(k)}(\omega) \psi_{2a}^{(k')*}(\omega') \delta_{k,k'} \\
& = \sum_k r_{1a}^{(k)2} \psi_{1a}^{(k)}(\omega) \psi_{1a}^{(k)*}(\omega') - \sum_k r_{2a}^{(k)2} \psi_{2a}^{(k)}(\omega) \psi_{2a}^{(k)*}(\omega').
\end{aligned} \tag{4.50}$$

Using the completeness of mode function $\{\psi_{1a}^{(k)}(\omega)\}$: $\sum_k \psi_{1a}^{(k)}(\omega) \psi_{1a}^{(k)*}(\omega') = \delta(\omega - \omega')$, we can rewrite the first relation in Eq.(4.39) as

$$\sum_k r_{2a}^{(k)2} \psi_{2a}^{(k)}(\omega) \psi_{2a}^{(k)*}(\omega') = \sum_k (r_{1a}^{(k)2} - 1) \psi_{1a}^{(k)}(\omega) \psi_{1a}^{(k)*}(\omega'). \tag{4.51}$$

Treating k as the row index and ω as the column index of a matrix, we can consider mode function $\psi^{(k)}(\omega)$ as matrix element of Ψ with $\{\Psi\}_{k,\omega} \equiv \psi^{(k)}(\omega)$ (we dropped subscript $1a, 2a$ for clarity). Then Eq.(4.51) is equivalent to the following matrix equation:

$$[\Psi_{2a}]^\dagger \begin{pmatrix} r_{2a}^{(1)2} & 0 & \dots \\ 0 & r_{2a}^{(2)2} & \dots \\ \vdots & \vdots & \ddots \end{pmatrix} \Psi_{2a} = [\Psi_{1a}]^\dagger \begin{pmatrix} r_{1a}^{(1)2} - 1 & 0 & \dots \\ 0 & r_{1a}^{(2)2} - 1 & \dots \\ \vdots & \vdots & \ddots \end{pmatrix} \Psi_{1a}. \tag{4.52}$$

Multiplying left of the above with matrix Ψ_{1a} and right with $[\Psi_{1a}]^\dagger$ and using orthonormal relation $\int d\omega \psi_{1a}^{(k)}(\omega) \psi_{1a}^{(k')*}(\omega) = \delta_{k,k'}$, we obtain a rotational transformation:

$$\mathbf{R} \begin{pmatrix} r_{2a}^{(1)2} & 0 & \dots \\ 0 & r_{2a}^{(2)2} & \dots \\ \vdots & \vdots & \ddots \end{pmatrix} \mathbf{R}^\dagger = \begin{pmatrix} r_{1a}^{(1)2} - 1 & 0 & \dots \\ 0 & r_{1a}^{(2)2} - 1 & \dots \\ \vdots & \vdots & \ddots \end{pmatrix} \quad (4.53)$$

with the transformation matrix $\mathbf{R} \equiv \Psi_{1a}[\Psi_{2a}]^\dagger$. The only solution for the above is $\mathbf{R} = \mathbf{I}$, or $\int d\omega \psi_{1a}^{(k)}(\omega) \psi_{2a}^{(k')*}(\omega) = \delta_{k,k'}$. With uniqueness of mode function set $\{\psi_{1a}^{(k)}(\omega)\}$, we have $\psi_{1a}^{(k)}(\omega) = \psi_{2a}^{(k)}(\omega)$, and then $r_{1a}^{(k)2} - r_{2a}^{(k)2} = 1$. Similarly, using the second relation in Eq.(4.39) we have $\psi_{1b}^{(k)}(\omega) = \psi_{2b}^{(k)}(\omega)$, and $r_{1b}^{(k)2} - r_{2b}^{(k)2} = 1$.

Next let us use the third relation in Eq.(4.39) and rewrite as:

$$\begin{aligned} & \int d\omega'' \sum_{k,k'} r_{1a}^{(k)} r_{2b}^{(k')} \psi_{1a}^{(k)}(\omega) \psi_{1b}^{(k')}(\omega') \phi_{1a}^{(k)}(\omega'') \phi_{2b}^{(k')}(\omega'') \\ & - \int d\omega'' \sum_{k,k'} r_{2a}^{(k)} r_{1b}^{(k')} \psi_{1a}^{(k)}(\omega) \psi_{1b}^{(k')}(\omega') \\ & \quad \times \phi_{2a}^{(k)}(\omega'') \phi_{1b}^{(k')}(\omega'') = 0. \end{aligned} \quad (4.54)$$

Multiplying both sides with $\psi_{1a}^{(k_1)*}(\omega) \psi_{1b}^{(k_2)*}(\omega')$ and integrating ω, ω' , with orthonormal relations for $\psi_{1a}^{(k)}(\omega), \psi_{1b}^{(k')}(\omega')$, we obtain

$$\cosh r_a^{(k_1)} \sinh r_b^{(k_2)} R_{k_2, k_1} = \sinh r_a^{(k_1)} \cosh r_b^{(k_2)} R'_{k_2, k_1}, \quad (4.55)$$

where we set $r_{1a}^{(k)} \equiv \cosh r_a^{(k)}$, $r_{1b}^{(k)} \equiv \cosh r_b^{(k)}$, then $r_{2a}^{(k)} = \sqrt{r_{1a}^{(k)2} - 1} = \sinh r_a^{(k)}$ and $r_{2b}^{(k)} = \sqrt{r_{1b}^{(k)2} - 1} = \sinh r_b^{(k)}$, and $R'_{k_2, k_1} \equiv \int d\omega \phi_{1b}^{(k_2)}(\omega) \phi_{2a}^{(k_1)}(\omega)$, $R_{k_2, k_1} \equiv \int d\omega \phi_{2b}^{(k_2)}(\omega) \phi_{1a}^{(k_1)}(\omega)$.

Switching back notations: $k = k_1, k' = k_2$, we have

$$\begin{aligned} R_{k,k} &= \tanh r_a^{(k)} \coth r_b^{(k')} R'_{k',k}, \\ R'_{k',k} &= \coth r_a^{(k)} \tanh r_b^{(k')} R_{k',k}, \end{aligned} \quad (4.56)$$

which, in matrix form, is simply $R = C_b R' C_a^{-1}$ or $R' = C_b^{-1} R C_a$ with

$$C_a \equiv \begin{pmatrix} \coth r_a^{(1)} & 0 & \dots \\ 0 & \coth r_a^{(2)} & \dots \\ \vdots & \vdots & \ddots \end{pmatrix} \quad (4.57)$$

and

$$C_b \equiv \begin{pmatrix} \coth r_b^{(1)} & 0 & \dots \\ 0 & \coth r_b^{(2)} & \dots \\ \vdots & \vdots & \ddots \end{pmatrix}. \quad (4.58)$$

Now notice that $RR^\dagger = I = R'R'^\dagger$, or using matrix form of Eq.(4.56), we obtain

$$C_b R' C_a^{-1} C_a^{-1} R'^\dagger C_b = I, \quad C_b^{-1} R C_a C_a R^\dagger C_b^{-1} = I. \quad (4.59)$$

Rewrite the above, we have

$$R' C_a^{-2} R'^\dagger = C_b^{-2}, \quad R C_a^2 R^\dagger = C_b^2. \quad (4.60)$$

Since matrices C_a, C_b are both diagonalized, the above expressions are true only if $R' = I = R$, or $\phi_{1a}^{(k)} = \phi_{2b}^{(k)*}$, $\phi_{1b}^{(k)} = \phi_{2a}^{(k)*}$ and $C_a = C_b$, or $r_a^{(k)} = r_b^{(k)}$.

Setting $r_a^{(k)} = r_b^{(k)} \equiv r_k G$ with r_k normalized: $\sum_k r_k^2 = 1$, and $\phi_{1a}^{(k)} = \phi_{2b}^{(k)*} \equiv \phi_k^{(a)}$, $\phi_{1b}^{(k)} = \phi_{2a}^{(k)*} \equiv \phi_k^{(b)}$, $\psi_{1a}^{(k)}(\omega) = \psi_{2a}^{(k)}(\omega) \equiv \psi_k^{(a)}(\omega)$, $\psi_{1b}^{(k)}(\omega) = \psi_{2b}^{(k)}(\omega) \equiv \psi_k^{(b)}(\omega)$ in Eq.(4.49), we obtain Eq.(4.41).

5. MEASUREMENT OF JOINT SPECTRAL DENSITY

5.1 Research Background

With the knowledge of JSF of SPDC, we can extract the TM structure and correlation information of the output fields with the singular value decomposition method. When the pump power is low, two-photon states are generated by the nonlinear interaction which dominate in the output fields except the vacuum state, as shown in Eq.(2.29). Joint spectral density $C_N|F(\omega_1, \omega_2)|^2$ (where C_N is a normalization factor) characterizes the frequency correlation of the output photon pair. $C_N|F(\omega_1, \omega_2)|^2 d\omega_1 d\omega_2$ describes the probability that the frequency of the photon of signal field is within $d\omega_1$ of ω_1 while the frequency of the correlated photon of idler field within $d\omega_2$ of ω_2 . The measurement of the JSF is of particular importance for the application of the TM framework of QIS. The TM structure can be derived theoretically with the singular value decomposition of the measured JSF. It can examine the application of the quantum nonlinear theory, and also verify our feedback-iteration method which directly measures the TMs of the output fields. Although the JSF can be measured, the joint spectral density is often measured in the laboratory instead for it's much easier to implement. This is valid when the spectral phases of TMs are relatively flat within the spectral range of interest. Even if it is not, the joint spectral density still provides the amplitude information of the TMs.

To date, joint spectral density has been measured with a statistical approach based on the spectrally resolved photon coincidence experiment [21]–[23], [59]. The measurement is very time consuming because the power of the pump field has been very low and the output field is mainly at two-photon states, and two single-photon detectors are used for the coincidence-counting measurements. Furthermore, the two single-photon detectors have to be adjusted each time to select specific frequencies. The two dimensional frequency domain has to be scanned over to reconstruct the joint spectral density graph. This leads to low resolution with a poor signal-to-noise ratio for the frequency drift of the pump laser in a long time duration. Recently an alternate method was implemented which measured the joint spectral density of the spontaneous process through the corresponding simulated process by a narrow-band seed laser beam [20], [24], [25]. It utilizes the relation of SPDC and stimulated emission that

share the same phase match relation and pump beam spectrum. This avoids the photon coincidence measurement and the spectrometer can be used as the detector instead of the single-photon detectors, therefore it saves measurement time and improves the resolution. We show an experimental demonstration of measurement of the joint spectral density for a SPDC process of a nonlinear crystal PPKTP pumped by an ultrafast pulse laser beam. A tunable CW external-cavity diode laser (ECDL) is used as a stimulated seed beam and the output beam is measured by a monochromator as a spectrometer. The joint spectral density is reconstructed by sweeping the seed wavelength.

Without considering the time ordering issue, the output two-photon state of the SPDC is given by

$$|\Psi_2\rangle \approx \int d\omega_1 d\omega_2 F(\omega_1, \omega_2) \hat{a}^\dagger(\omega_1) \hat{a}^\dagger(\omega_2) |vac\rangle, \quad (5.1)$$

which is the dominant component of the output field beside the vacuum state when the pump field is operated at relatively low power. Therefore the joint spectral density can be measured by the spectrally resolved single photon coincidence experiment $\langle \Psi_2 | \hat{a}^\dagger(\omega_1) \hat{a}^\dagger(\omega_2) \hat{a}(\omega_1) \hat{a}(\omega_2) | \Psi_2 \rangle = |F(\omega_1, \omega_2)|^2$. This measurement is very time consuming as we discussed above. Instead we can exploit the stimulated emission by using a CW coherent laser field $\alpha(\omega_1)$ in signal input port as a seed beam, and measure the spectrally pre-conditioned marginal output spectra of the idler field $\langle \Psi'_2 | \hat{a}^\dagger(\omega_2) \hat{a}(\omega_2) | \Psi'_2 \rangle$, with $|\Psi'_2\rangle = \int d\omega_1 d\omega_2 F(\omega_1, \omega_2) \hat{a}^\dagger(\omega_1) \hat{a}^\dagger(\omega_2) |\alpha(\omega_1), vac_2\rangle \approx \int d\omega_1 d\omega_2 F(\omega_1, \omega_2) \alpha^*(\omega_1) \hat{a}^\dagger(\omega_2) |\alpha(\omega_1), vac_2\rangle$ for $|\alpha|^2 \gg 1$. Here $|vac_2\rangle$ represents the vacuum state in the idler input port. Since CW coherent field has narrow spectral band $\alpha(\omega_1) = \alpha \delta(\omega_1 - \omega_{10})$, we have $\langle \Psi'_2 | \hat{a}^\dagger(\omega_2) \hat{a}(\omega_2) | \Psi'_2 \rangle$, with $|\Psi'_2\rangle = \alpha^* \int d\omega_2 F(\omega_{10}, \omega_2) \hat{a}^\dagger(\omega_2) |\alpha(\omega_1), vac_2\rangle$ (as long as we keep the power of the stimulated emission field much less than the seed field $|\alpha|^2 |F(\omega_{10}, \omega_2)|^2 \ll 1$, this term dominates in the output field besides the vacuum). and the output spectra of the idler field

$$\langle \Psi'_2 | \hat{a}^\dagger(\omega_2) \hat{a}(\omega_2) | \Psi'_2 \rangle = |\alpha|^2 |F(\omega_{10}, \omega_2)|^2. \quad (5.2)$$

Sweeping the seed frequency ω_{10} allows the reconstruction of the joint spectral density. (see Fig.5.1).

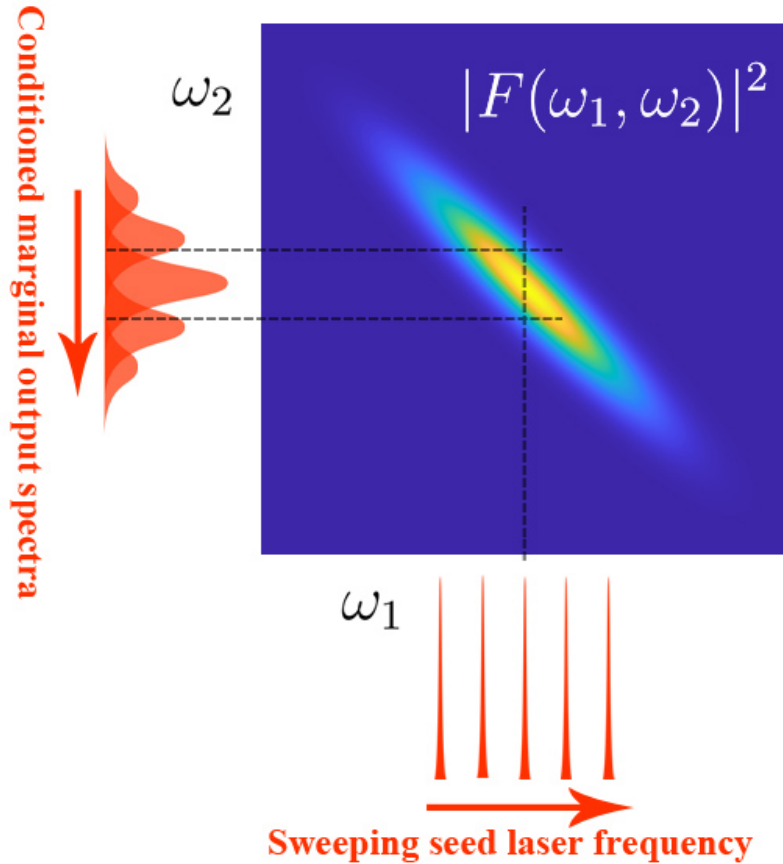


Figure 5.1. Reconstruction of a typical joint spectral density, shared by the SPDC and its counterpart stimulated emission process for the same nonlinear crystal at the same pump configuration. A narrow-band seed laser beam at frequency ω_{10} stimulates the emission of a spectrally pre-conditioned coherent output beam in the idler mode. This spectrum is proportional to the joint spectral density with the signal frequency being ω_{10} (Eq.(5.2)). The joint spectral density can be obtained by sweeping the frequency of the seed beam.

5.1.1 Quasi-phase Matching for Periodic Poled Material

Birefringence is the optical property of a material having a refractive index that depends on the polarization and propagation direction of light that passes through. Typically, SPDC is done in a birefringent crystalline material. The polarizations of the fields and the ori-

entation of the crystal are chosen such that the phase-matching condition is fulfilled. This phase-matching technique is called angle tuning. Typically a crystal has three axes, one or two of which have a different refractive index than the other one(s). Potassium titanyl phosphate (KTP) is a Biaxial crystal which has three refractive indices corresponding to three principal axes XYZ of the crystal. In our application we only exploit the YZ plane and call the two axes Y, Z with the traditional names "extraordinary" (e) and "ordinary" (o) axis, respectively, and the corresponding light beam with the polarization parallel to the axis e and o light, respectively. There are several schemes of choosing the polarizations for this crystal type. The two types we exploit in our experiment is type-0 and type-II phase matching: If the signal, idler and the pump beam have the same polarization ($o + o \rightarrow o$ or $z + z \rightarrow z$ interaction), it is called "type-0 phase matching", and if the signal and idler beam's polarizations are perpendicular ($e + o \rightarrow e$ or $y + z \rightarrow y$ interaction), it is called "type-II phase matching". PPKTP is produced by periodic poling of the crystal KTP, whereby a structure of regularly spaced ferroelectric domains with alternating orientations are created in the material. The structure is designed to achieve quasi-phase matching in the material. It ensures that the energy always flows from the pump field to the second harmonic fields even though their phases are not matched perfectly. We use two PPKTP in our experiment. The first one employs type-0 phase matching with the poling period length of the crystal of $3.425 \mu\text{m}$. The size of the crystal is $1 \times 1 \times 5 \text{ mm}$. It transfers o polarized pulse fields with the central wavelength of 810 nm to the o pulse fields with the central frequency of 405 nm with the second harmonic generation process. The output field works as the pump beam for the second PPKTP, the joint spectral density of which we are interested in measuring. The second PPKTP employs type-II phase matching with the poling period length of the crystal of $10 \mu\text{m}$. The size of the crystal is $1 \times 2 \times 2.5 \text{ mm}$. It transfers the pump beam into two different polarized (o and e) fields with the central frequencies near 810 nm with the SPDC process.

In the section 2.2.4, we obtain the JSF for birefringent phase matching. Now we will work on the quasi-phase matching. The technique of Periodic poling alternates the orientation of the crystal periodically in the direction of the pump beam. Therefore it changes the sign

of $\chi^{(2)}$ periodically in z direction. The interaction Hamiltonian of the nonlinear effect (Eq.(2.20)) is modified to

$$H_{int}^{(2),PPM} = \int d^3r \eta(z) \frac{2}{3} \epsilon_0 \vec{E}(\vec{r}, t) \cdot \chi^{(2)} : \vec{E}(\vec{r}, t)^2, \quad (5.3)$$

with $\eta(z) = 1$ for $(2n - 2)l \leq z < (2n - 1)l$ and $\eta(z) = -1$ for $(2n - 1)l \leq z < 2nl$. l is the half poling period length of the crystal. $n = 1, 2, 3, \dots$ denotes the n th half polling period. When pulsed laser is used as the pump laser, $\alpha_p(\omega_1 + \omega_2) = \sqrt{P} \exp[-\frac{(\omega_1 + \omega_2 - \omega_{pc})^2}{2\sigma_p^2}]$ describes the pump field with a Gaussian spectral envelope with width σ_p , a central frequency of ω_{pc} and the power of P . Work out the integral in Eq.(5.3) we obtain the joint spectral density

$$|F(\omega_1, \omega_2)|^2 \propto \left| \text{sinc}(\Delta Kl/2) \frac{\sin[(\Delta Kl + \pi)n/2]}{\sin[(\Delta Kl + \pi)/2]} \exp[-\frac{(\omega_1 + \omega_2 - \omega_{pc})^2}{2\sigma_p^2}] \right|^2, \quad (5.4)$$

where n is the number of the periods of the periodic polled material. From the term $\sin[(\Delta Kl + \pi)n]/\sin(\Delta Kl + \pi)$, we can see when $l = \pi/\Delta K$ the joint spectral density reached the peak. That is how the length of the period of the material is chosen in the production for the nonlinear process of specific wavelengths. We can change the variables of frequencies in Eq.(5.4) to wavelengths as following,

$$\exp[-\frac{(\omega_1 + \omega_2 - \omega_{pc})^2}{2\sigma_p^2}] = \exp[-\frac{\lambda_{pc}^4(1/\lambda_1 + 1/\lambda_2 - 1/\lambda_{pc})^2}{2\sigma_\lambda^2}], \quad (5.5)$$

where $\lambda_{pc} = 405$ nm, $\sigma_\lambda = 0.813$ nm

$$\Delta Kl = k_s l + k_i l - k_p l = \left[\frac{2\pi n_y(\lambda_1)}{\lambda_1} + \frac{2\pi n_z(\lambda_2)}{\lambda_2} - \frac{2\pi n_y(\lambda_p)}{\lambda_p} \right] l, \quad (5.6)$$

where $\lambda_p = \lambda_1 \lambda_2 / (\lambda_1 + \lambda_2)$.

$$\begin{aligned} n_y(\lambda) &= \sqrt{2.1518 + 0.87862\lambda^2/(\lambda^2 - 0.21801^2) - 0.01327\lambda^2}, \\ n_z(\lambda) &= \sqrt{2.3136 + 1.00012\lambda^2/(\lambda^2 - 0.23831^2) - 0.01679\lambda^2}. \end{aligned} \quad (5.7)$$

Here $l = 5.1 \mu\text{m}$ in Eq.(5.6) denotes the half length of the period of PPKTP, and the unit of wavelength in Eq.(5.7) is μm . We obtain the joint spectral density as the function of λ_1 and λ_2 . Fig.5.2 show the contour graph of the joint spectral density for the PPKTP.

5.1.2 Experimental Implementation

The experimental setup mainly comprises two stages. Firstly, OPA is realized with quasi-phase matching by fine tuning of angle with both the pump beam and seed beam being the pulse laser. Optimize the stimulated output with the help of a lock-in amplifier. Secondly, a CW beam from an ECDL is used as the seed beam instead of the pulsed seed beam. The seed beam is collimated and overlapped with the pulse pump beam while keeping the angles of the pump beam and the PPKTP fixed. Optimize the output. The first stage is necessary because it works as an assistantary process to align CW beam with the pump beam and PPKTP, which is difficult for the small signal of the output. Sweep the frequency of the seed beam and measure the spectrum of the stimulated output with the help of a monochromator or optical spectrum analyzer (OSA). This will make a measurement of the joint spectral density.

In the first stage, the experiment is set up as shown in Fig.5.4. The main laser source is a tunable femtosecond Ti:Sapphire laser with an output power at around 250 mW and pulse repetition rate of 76 MHz. The pulse duration for the femtosecond Ti:Sapphire laser is 100 fs. The bandwidth of the pulse beam is around 6.5 nm (see Fig.5.3). The wavelength of the laser source is tuned to 810 nm (IR), as marked in red color in the schematic Figure. Human's eye is not sensitive to this frequency. A near infrared (NIR) sensor card is used to spot the light beam. The laser beam first passed through the first type-0 PPKTP which doubles the frequency of the laser beam with the type-0 second harmonic generation. It generates a blue beam with the central wavelength of 405 nm from the IR pulse beam with the same polarization (perpendicular to the optical table). A pair of lenses is placed on both sides of the crystal to achieve a higher conversion rate while maintaining the profile of the laser beam. By fine tuning the angle of the beam and crystal so that the phase matching condition is satisfied, the second harmonic field is generated all the way through the crystal which propagates

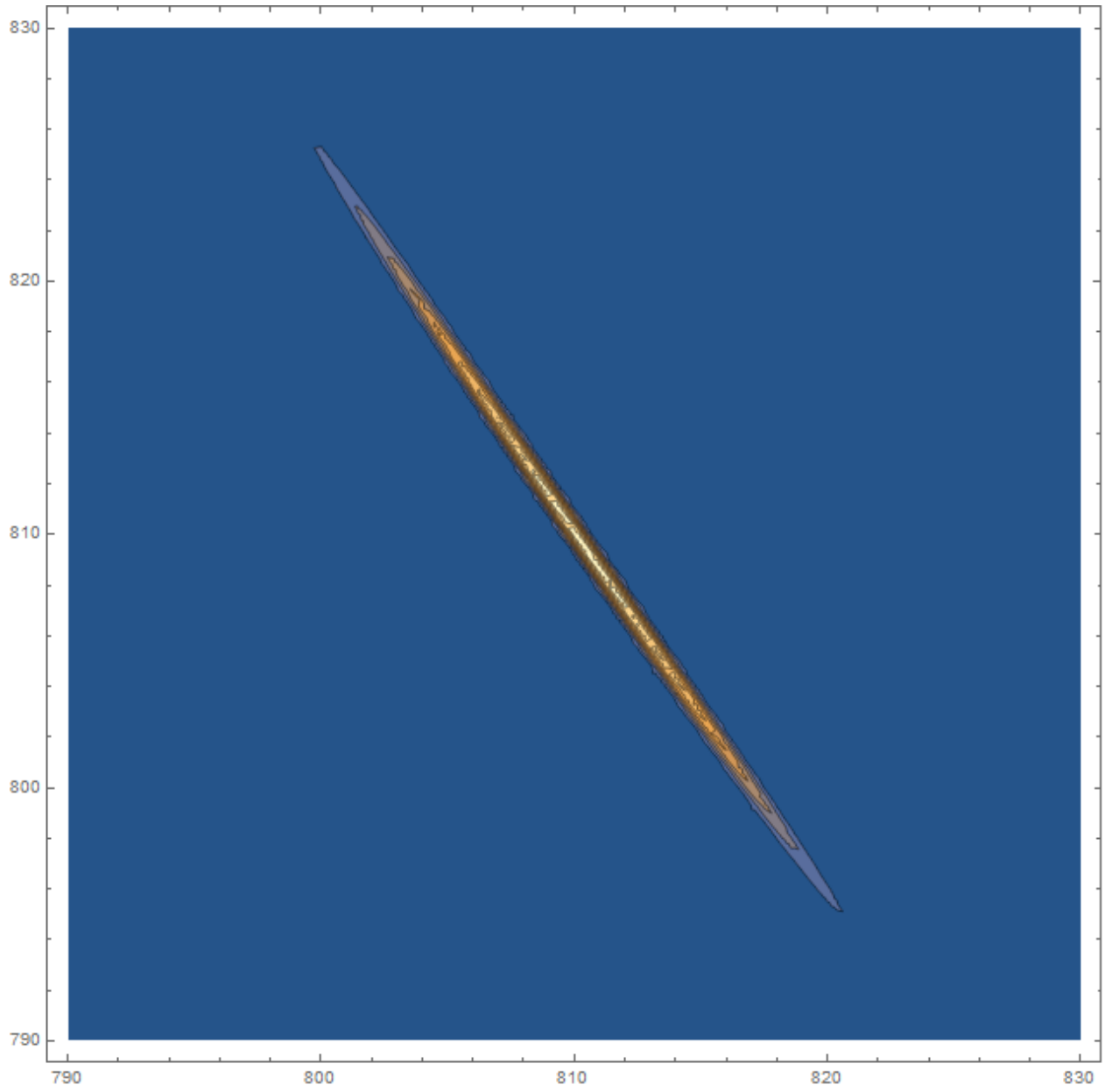


Figure 5.2. The joint spectral density for PPKTP obtained by theoretical calculation

collimated with the IR source beam. A Dichroic Beam Splitter (DBS) is used to separate the IR and blue beams. The output blue beam (with the polarization perpendicular to the optical table) works as the pump beam of the second PPKTP (after going through an optical chopper) for the SPDC and its counterpart stimulated emission process, the joint spectral density of which is to be measured. The IR beam (with the polarization perpendicular to the optical table) works as the seed beam for the second PPKTP after going through a delay, which is made out of two coated mirrors that are attached to a manual translation stage. The stage is adjusted back and forth to make sure the pulses of the IR beam and blue beam arrive at the second PPKTP simultaneously. The full width at half maximum (FWHM) of the pulse \times the speed of light shows how precisely we need to control the delay, i.e., $100 \text{ fs} \times 3 \times 10^8 \text{ m/s} = 30 \text{ }\mu\text{m}$. The stimulated emission of the parametric process for the second PPKTP is just a reverse type II second harmonic generation. It transfers the e polarized blue beam to an e IR beam which is the same as the seed beam, and an o polarized (parallel to the optical table) IR beam. The o polarized IR beam is extracted by a Polarizing Beam Splitter (PBS) and a longpass optical filter (which rejects the blue beam), and measured by the Model SR830 DSP lock-in amplifier with the oscillation signal from the optical chopper. We tune the angles of the laser beams and the directions of the crystals until obtaining the best output results.

The lock-in amplifier is used because although the PBS rejects the e IR seed beam, there is a component of the seed beam in the final output due to the imperfection of the experimental device. The stimulated emission is at a very low level so that the field from the seed beam is much larger than from the stimulated emission even after the PBS. Therefore the signal of the stimulated emission will be covered by that of the component of the seed beam and its fluctuation. However the stimulated emission is related to the pump beam the intensity of which is modulated by the optical chopper. The detection of the stimulated emission is an AC signal with the frequency determined by the optical chopper. The IR seed beam is not affected and corresponds to a DC signal in the measurement. With the lock-in amplifier, the AC signal of the stimulated emission field will be selected out and measured.

In the second stage of the experiment (Fig.5.5), A Littrow Modular CW Tunable External Cavity Laser from Sacher Lasertechnik is used as the seed beam instead of the pulse laser

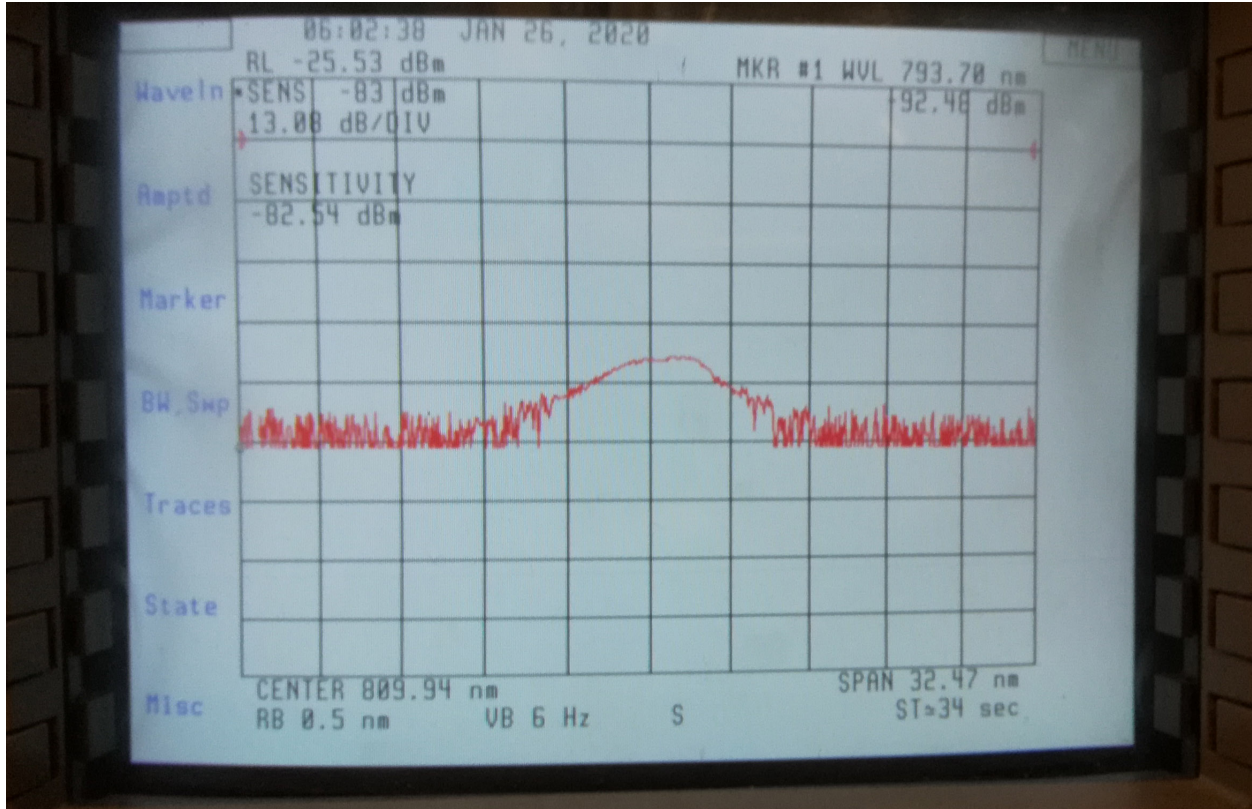


Figure 5.3. The spectrum of the femtosecond Ti:Sapphire laser measured with OSA. The central wavelength of the pulse spectrum is around 810 nm. The bandwidth of the pulse beam is around 6.5 nm.

from the Ti:Sapphire laser. This is achieved by a flipper mirror conveniently. When the flipper mirror is turned up, the CW beam will be injected to the second PPKTP and pulse IR beam is blocked, while if the flipper mirror is turned down, the pulse IR beam is injected to the PPKTP and the CW beam is blocked. The CW laser is operated at the power of around 15 mw and in the e polarization. A pair of lenses is used to modify the profile of the CW beam so that it shares the same spatial transverse mode with pulse IR beam to improve the efficiency of the OPA effect. Moreover the CW beam has to be adjusted so that it shares the same light path with the pulse IR beam too. We use the second flipper mirror in front of the second PPKTP to make sure the beam collimated and overlapped with the pump beam in a long distance. With the flipper mirror turned up, the two beams are projected to the NIR sensor card after the mirror. We adjust the CW beam so that the light spot overlaps with the pulse IR beam on the NIR sensor card both right after the flipper mirror and after

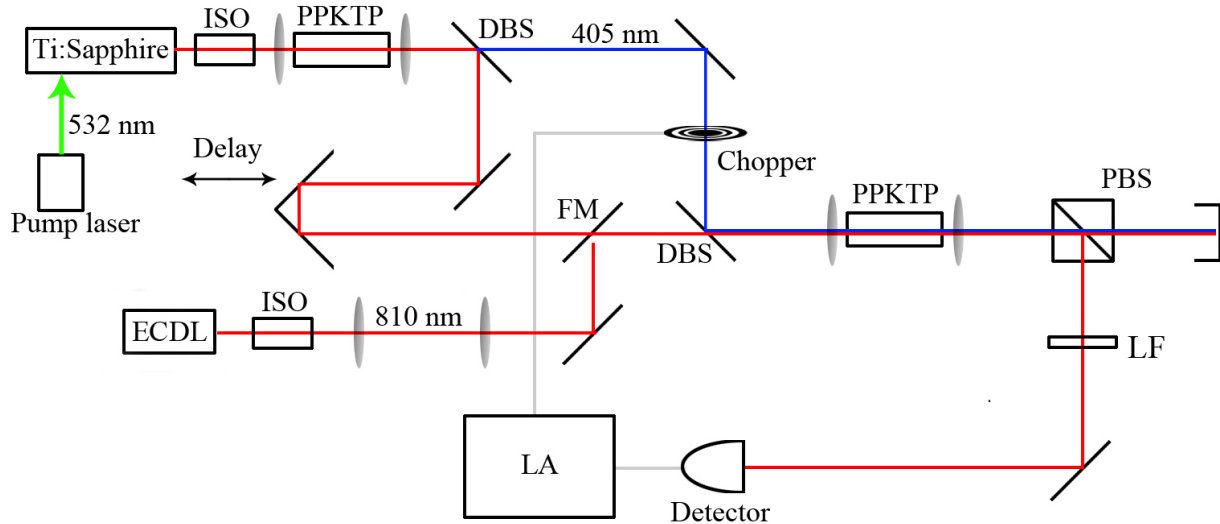


Figure 5.4. A schematic diagram for the first stage of the experiment. DBS: dichroic beam splitter. PBS: polarized beam splitter. ECDL: external-cavity diode laser. FM: flipper mirror. LA: lock-in amplifier. ISO: optical isolator. LF: optical longpass filter.

propagating a long distance. When the light beams are aligned, the flipper mirror is turned down and the output field of *o* polarization extracted by the PBS and longpass filter is measured by a detector with a lock-in amplifier. This gives the overall power of the output field so that we can optimize the nonlinear effect by maximising the output. To obtain the spectra of the stimulated emitted field, we can either place a monochromator in the front of the detector or just replace the whole detection system with an OSA, as shown in Fig.5.5. We tune the wavelength of the ECDL over the domain of interest (from 803 nm to 815 nm) with the steps of 0.5 nm and record the corresponding output spectra for reconstructing the joint spectral density. The wavelength of ECDL is measured with an OSA. Fig.5.6 is a photograph of the experimental setup in which the spectra of the stimulated emitted field is measured with the monochromator and lock-in amplifier (which is not shown in the graph).

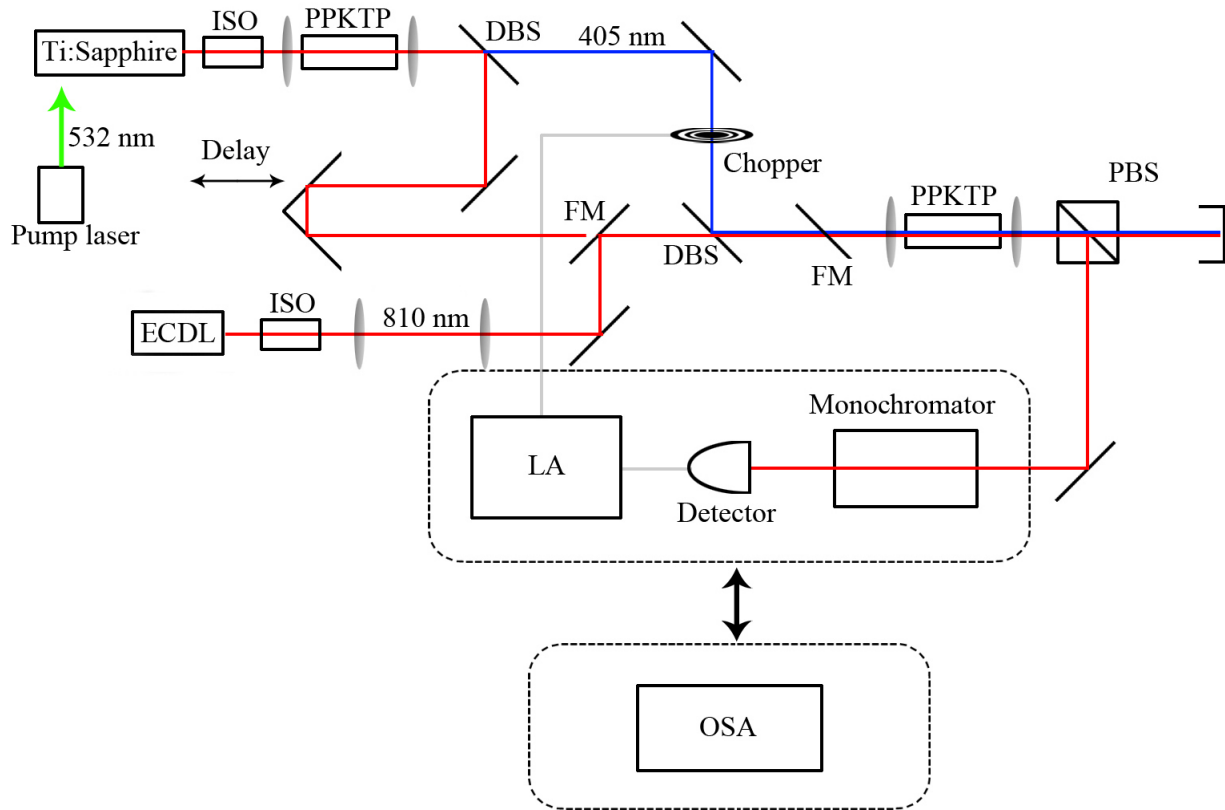


Figure 5.5. A schematic diagram for the second stage of the experiment. DBS: dichroic beam splitter. PBS: polarized beam splitter. ECDL: external-cavity diode laser. FM: flipper mirror. LA: lock-in amplifier. ISO: optical isolator. OSA: optical spectrum analyzer

5.1.3 Experimental Results and Discussions

Fig.5.7 shows the experimental measured joint spectral intensity (the normalization of which is the joint spectral density) based on the stimulated emission. The spectrum of the stimulated output is measured with an optical detector and lock-in amplifier. The profile of joint spectral density shows an anti-correlation of the seed beam (signal) and output beam (idler) wavelength. It is consistent with theoretical results (Fig.5.2). The data is measured with the resolution of 0.5 nm and interpolated with Matlab. The peak value of joint spectral density happens when the wavelength of the seed beam is around 807 nm. It deviates from the theoretical 810 nm. We have tried tuning the central wavelength of the Ti:Sapphire laser but the peak value doesn't change significantly. The deviation may be due to the fabrication

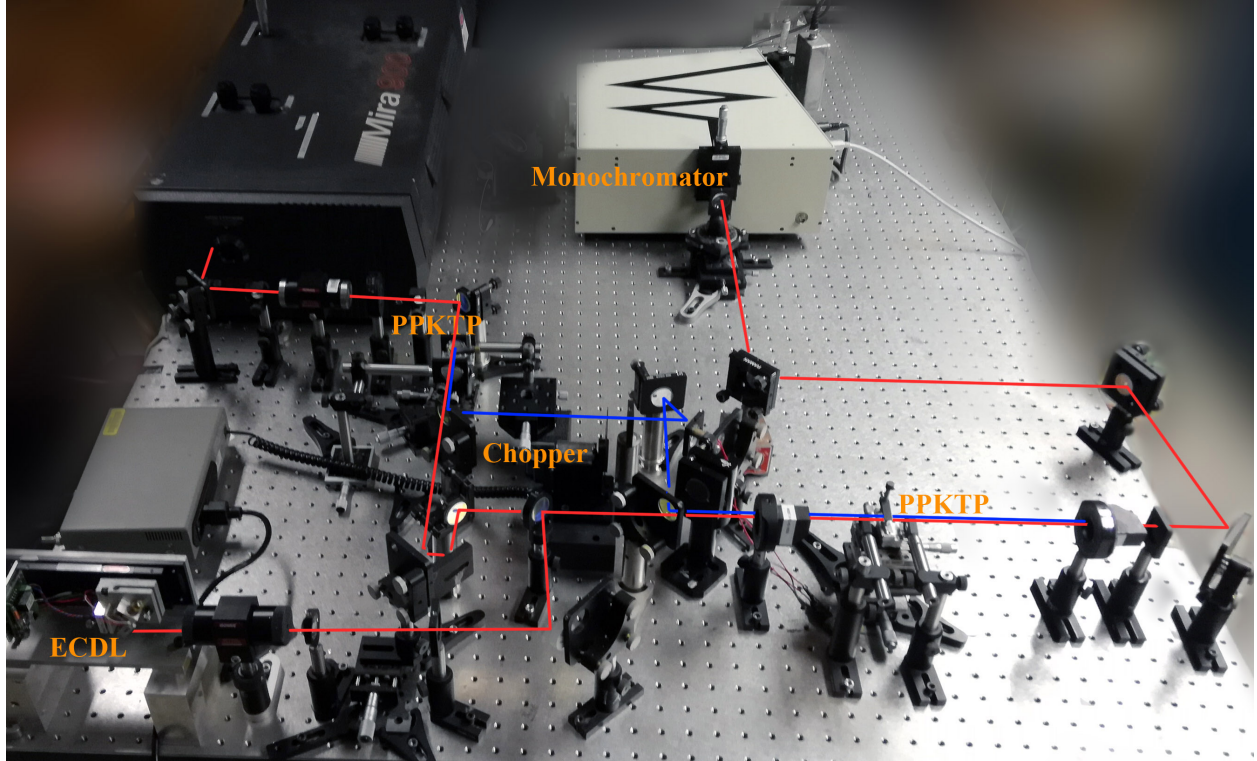


Figure 5.6. A photograph of the experimental setup taken from above the optical table.

error of the crystal. There is a line intersecting with the joint spectral density pattern. The wavelength of the output field is just correlated with the seed beam. But note that we use a lock-in amplifier to process the data with the oscillation signal from the optical chopper. The optical chopper is in the light path of the 405 nm pump beam. With the lock-in amplifier, only the AC signal with the same frequency of the chopper will be kept in the final data output. Thus this part of the spectrum shares the same wavelength with the seed beam, and is not only related to the seed beam but also with the pump beam. Its polarization is not the same as the output o beam but more close to e beam. The signal measured in the graph is only from the small o component extracted by the PBS. This is due to the imperfection of the experiment. Although only a small component of this beam is extracted by the PBS, The signal is either comparable with or much larger than stimulated emission, depending on the angle tuning. This output field may be explained by the stimulated Raman scattering of the crystal with the same pump and seed beam of SPDC. One photon of the pump beam is

transferred to one photon of the seed beam. The energy difference is absorbed by the crystal molecule in the form of the mechanical vibration.

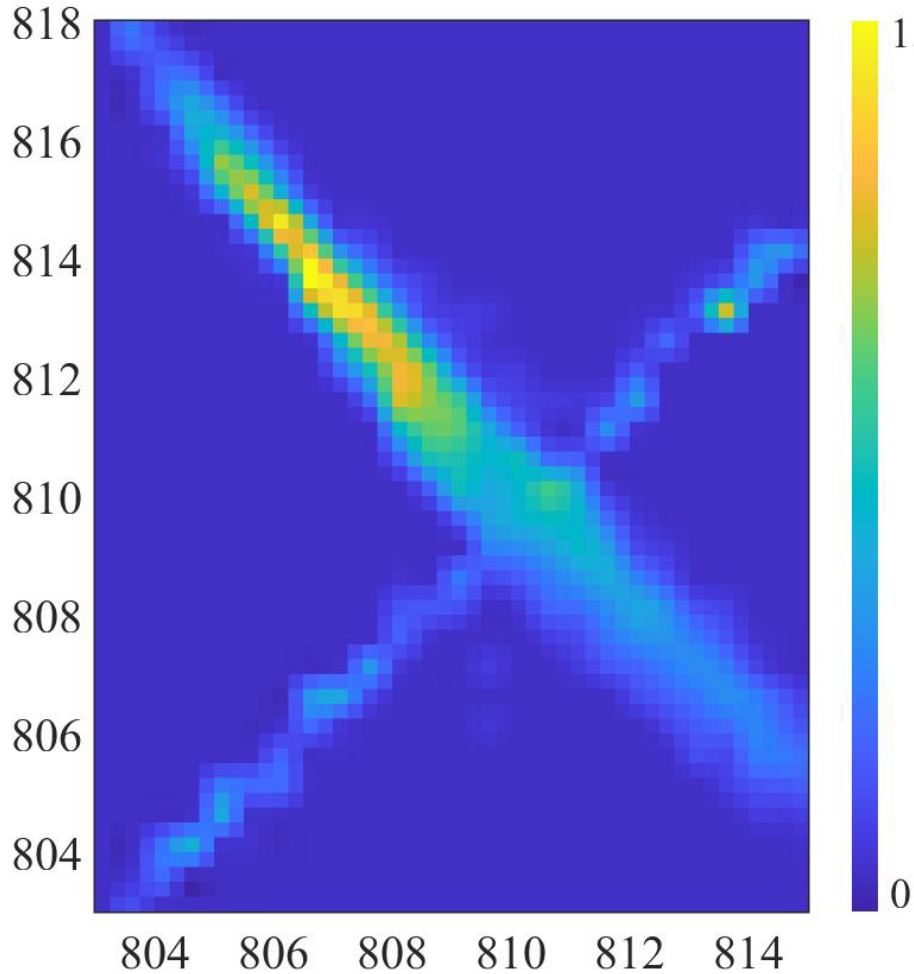


Figure 5.7. Experimental joint spectral intensity (normalized with the peak value) obtained by stimulated emission based measurements. The spectrum of the stimulated output is measured with an optical detector and lock-in amplifier. measurements

Fig.5.8 shows the joint spectral intensity measured with hp 70951A OSA. The data is read and recorded through HP-IB (GPIB) by PC with NI-488.2 Communicator of Labview. The spectrum of the stimulated output when the wavelength of the seed beam is 809 nm is shown Fig5.9. The spectrum of the seed beam (also the small *o* component) can be seen as well as the stimulated emission. Note OSA measures DC signal. So this is mainly the *o*

component of the seed beam. But the emission with the same wavelength of the seed beam is still there which is covered by the seed beam. In the reconstructed joint spectral density we remove the seed beam manually. The resolution of the wavelength for the seed beam scanning and spectrum data is set to 1 nm, and interpolated with matlab.

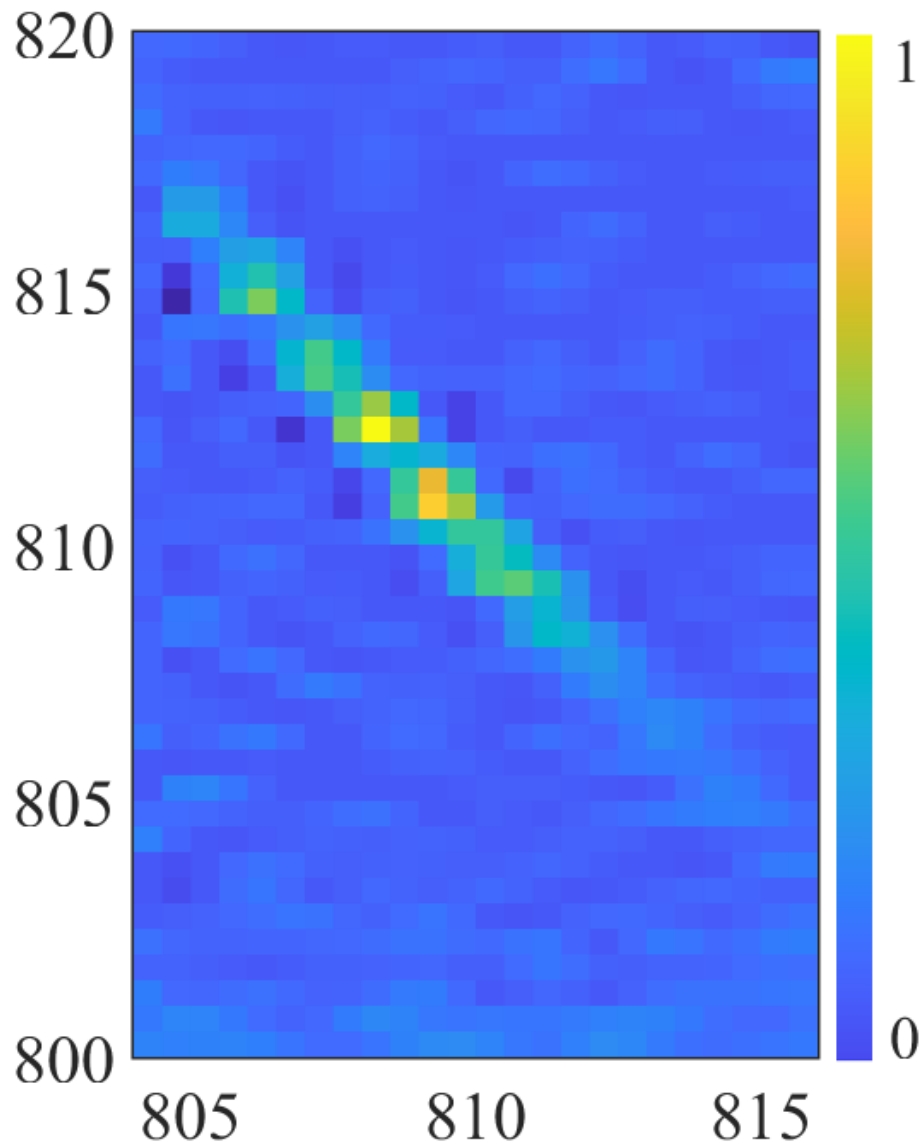


Figure 5.8. Experimental joint spectral intensity (normalized with the peak value) obtained by stimulated emission based measurements. The spectrum of the stimulated output is measured with OSA.

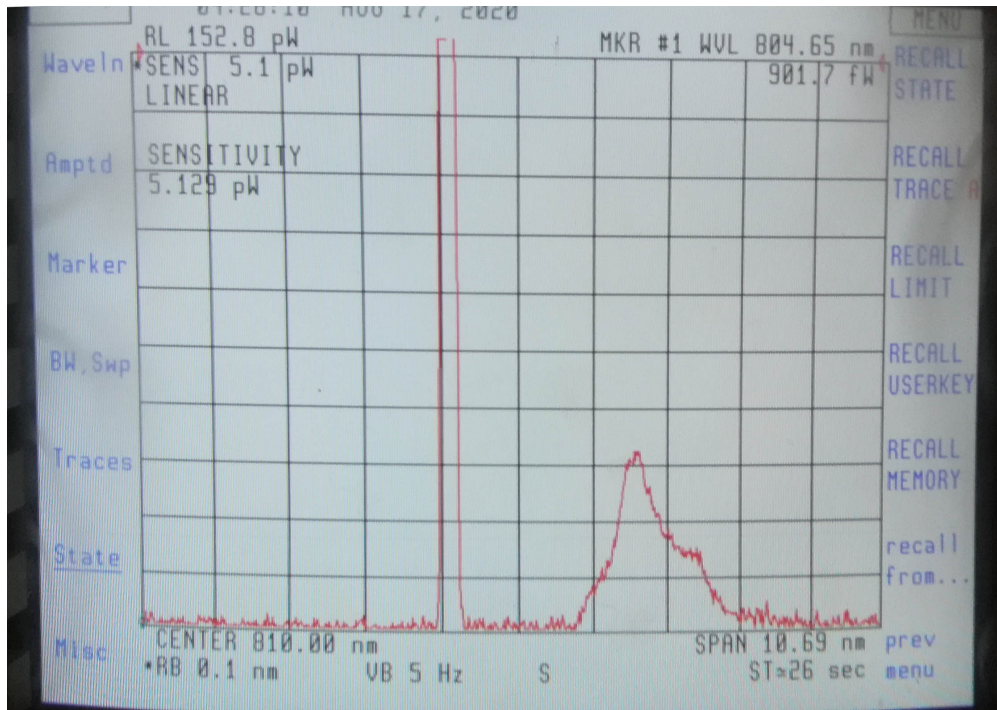


Figure 5.9. The spectrum of the stimulated output measured with OSA when the wavelength of the seed beam is 809 nm.

6. PARAMETRIC AMPLIFIER FOR BELL MEASUREMENT IN CONTINUOUS-VARIABLE QUANTUM STATE TELEPORTATION

Quantum interference plays an important role in the display of many quantum phenomena. It usually requires a linear beam splitter to superimpose two fields for interference between them. This happens in many protocols of quantum information processing. For example, optical quantum computing relies on the Hong-Ou-Mandel effect where a beam splitter is an essential element [4], [5]. Current applicable schemes of Bell measurement [26], [27] for quantum state teleportation [28]–[31] require beam splitters to mix the incoming unknown state with one field of an entangled state.

It is well-known that losses are notorious in degrading quantum effects and are the key obstacle in many protocols of quantum information processing. Detection process often introduces losses due to imperfect coupling and less-than-unit quantum efficiency. Highly efficient detectors are only available for some limited spectrum of the electromagnetic waves. Thus, it becomes a major concern in high fidelity quantum communication involving quantum measurement by detection. Quantum state teleportation is one of such quantum communication protocols where a Bell measurement is performed to projectively select out the required states. For continuous-variable quantum state teleportation, Bell measurement is usually achieved by homodyne detection, which is sensitive to losses. This will inevitably affect the fidelity of the teleported state.

On the other hand, amplification is known to overcome the effect of losses. Indeed, PA were recently used in $SU(1,1)$ interferometers [48] and quantum entanglement measurement [60] to mix two fields by replacing beam splitters (BS) for interference and was demonstrated to be loss-tolerant in detection processes.

At first look, it seems counter-intuitive that a PA can be of any use in QIS and play any role in mixing fields for interference since it is often portrayed as adding extra noise and thus degrading the signal in the amplification processes [61]. However, if we look into the origin of the extra noise, we find it comes from the vacuum fluctuations of the internal degrees of the amplifier. So, if we can access these internal degrees and place them in correlation

with the input, the extra noise can actually be suppressed due to quantum correlation [62], [63]. Therefore, by treating the internal degrees of the amplifier as another input, we mix them with the original input and use the amplifier as a field mixer similar to a beam splitter. Specifically, PAs are such devices for which the internal degree is the so-called idler field that we can easily access from outside. In essence, a PA is a four-port linear device just like a beam splitter, even though it is often realized through nonlinear interaction with energy actively pumped into it for amplification. We investigate the feasibility of replacing a beam splitter by a PA for Bell measurement in quantum teleportation scheme and demonstrate the loss tolerant property of the new scheme.

6.1 Quantum State Transformation of a Parametric Amplifier

The role played by a PA in the mixing of fields for interference can be understood from the following input-output relation:

$$\hat{a}_{1(PA)}^{(o)} = G\hat{a}_1^{(i)} + g\hat{a}_2^{(i)\dagger}, \quad \hat{a}_{2(PA)}^{(o)} = G\hat{a}_2^{(i)} + g\hat{a}_1^{(i)\dagger}, \quad (6.1)$$

where G, g are amplitude gains satisfying $G^2 - g^2 = 1$ and without loss of generality, we assume they are real and positive (otherwise, we can always absorb the extra phases in $\hat{a}_{1,2}$).

In comparison, the input-output relation for a beam splitter is given by

$$\hat{a}_{1(BS)}^{(o)} = t\hat{a}_1^{(i)} + r\hat{a}_2^{(i)}, \quad \hat{a}_{2(BS)}^{(o)} = t\hat{a}_2^{(i)} - r\hat{a}_1^{(i)} \quad (6.2)$$

with $t^2 + r^2 = 1$. It can be seen that the PA is basically a four-port linear device that not only amplifies but also, similar to a beam splitter, mixes the two input fields.

However, the difference between the two devices is also obvious: the PA output is related to the Hermitian conjugate of the second input field, which can lead to unwanted spontaneous emission even with input in vacuum, as seen in the average photon number:

$$\begin{aligned} \langle \hat{N}_{1(PA)}^{(o)} \rangle &\equiv \langle \hat{a}_1^{(o)\dagger} \hat{a}_1^{(o)} \rangle \\ &= G^2 \langle \hat{a}_1^{(i)\dagger} \hat{a}_1^{(i)} \rangle + g^2 (\langle \hat{a}_2^{(i)\dagger} \hat{a}_2^{(i)} \rangle + 1), \end{aligned} \quad (6.3)$$

if the two inputs are independent of each other. So, PA is not suitable for mixing photons or quantum information processing with discrete variables. On the other hand, the input-output relations for quadrature-phase amplitudes are given by

$$\hat{X}_{1,2(PA)}^{(o)} = G\hat{X}_{1,2}^{(i)} + g\hat{X}_{2,1}^{(i)}, \quad \hat{Y}_{1,2(PA)}^{(o)} = G\hat{Y}_{1,2}^{(i)} - g\hat{Y}_{2,1}^{(i)}, \quad (6.4)$$

which is similar to those for a beam splitter:

$$\hat{X}_{1,2(BS)}^{(o)} = t\hat{X}_{1,2}^{(i)} \pm r\hat{X}_{2,1}^{(i)}, \quad \hat{Y}_{1,2(BS)}^{(o)} = t\hat{Y}_{1,2}^{(i)} \pm r\hat{Y}_{2,1}^{(i)}, \quad (6.5)$$

where $\hat{X} \equiv \hat{a} + \hat{a}^\dagger$, $\hat{Y} \equiv (\hat{a} - \hat{a}^\dagger)/j$ ($j \equiv \sqrt{-1}$) for the corresponding field described by \hat{a} . So, they only differ in coupling coefficients. Therefore, for continuous variable quantum information processing, a PA can play the same role as a BS for superimposing two fields. Note from Eqs.(6.4,6.5) that similar to the situation of loss, which introduces quantum noise through vacuum in the unused port, amplification also adds noise through the vacuum of the second input if it is unattended and thus uncorrelated with the signal input. For this reason, the second input is usually called “idler”.

The relationships in Eqs.(6.4,6.5) provide us a way to evaluate quantum state transfer through a BS and a PA, which can be done through Wigner function representation [37]. For a PA with input state described by a Wigner function $W_{in}(X_1, Y_1; X_2, Y_2)$, the output Wigner function of the PA is given by (for details, see Appendix 6.A.1)

$$\begin{aligned} W_{out}^{(PA)}(x_1, y_1; x_2, y_2) \\ = W_{in}(Gx_1 - gx_2, Gy_1 + gy_2; Gx_2 - gx_1, Gy_2 + gy_1). \end{aligned} \quad (6.6)$$

Similarly for a BS with the same input state, the output state is described by [37]

$$\begin{aligned} W_{out}^{(BS)}(x_1, y_1; x_2, y_2) \\ = W_{in}(tx_1 - rx_2, ty_1 - ry_2; tx_2 + rx_1, ty_2 + ry_1). \end{aligned} \quad (6.7)$$

Comparing Eqs.(6.6,6.7), we find the output Wigner functions for the two devices give rise to superposition of input fields but with different phases and different transfer coefficients.

As an example, let us consider the input of a two-mode squeezed state with a Wigner function of [64]

$$\begin{aligned} W_{in}(x_1, y_1; x_2, y_2) &= \frac{1}{(2\pi)^2} e^{-\frac{1}{4}[(x_1+x_2)^2+(y_1-y_2)^2]e^{2s}} \\ &\quad \times e^{-\frac{1}{4}[(x_1-x_2)^2+(y_1+y_2)^2]e^{-2s}}, \end{aligned} \quad (6.8)$$

where s is the squeezing parameter. It is known that when $t = r = 1/\sqrt{2}$, the output of BS is two single-mode squeezed states with squeezing at orthogonal quadratures. This can be easily confirmed from Eq.(6.7):

$$\begin{aligned} W_{out}^{(BS)}(x_1, y_1; x_2, y_2) &= \frac{1}{(2\pi)^2} e^{-\frac{1}{2}(x_1^2+y_2^2)e^{2s}} e^{-\frac{1}{2}(x_2^2+y_1^2)e^{-2s}} \\ &= \frac{1}{2\pi} e^{-\frac{1}{2}(x_1^2e^{2s}+y_1^2e^{-2s})} \frac{1}{2\pi} e^{-\frac{1}{2}(x_2^2e^{-2s}+y_2^2e^{2s})}. \end{aligned} \quad (6.9)$$

The corresponding situation for a PA is:

$$\begin{aligned} W_{out}^{(PA)}(x_1, y_1; x_2, y_2) &= \frac{1}{(2\pi)^2} e^{-\frac{1}{4}[(x_1+x_2)^2+(y_1-y_2)^2]e^{2s}(G-g)^2} \\ &\quad \times e^{-\frac{1}{4}[(x_1-x_2)^2+(y_1+y_2)^2]e^{-2s}(G+g)^2}. \end{aligned} \quad (6.10)$$

Especially when $G + g = 1/(G - g) = e^s$, we have

$$\begin{aligned} W_{out}^{(PA)}(x_1, y_1; x_2, y_2) &= \frac{1}{2\pi} e^{-\frac{1}{2}(x_1^2+y_1^2)} \frac{1}{2\pi} e^{-\frac{1}{2}(x_2^2+y_2^2)}, \end{aligned} \quad (6.11)$$

which is just the Wigner function for vacuum. This is equivalent to the case of balanced gain in an SU(1,1) interferometer [48].

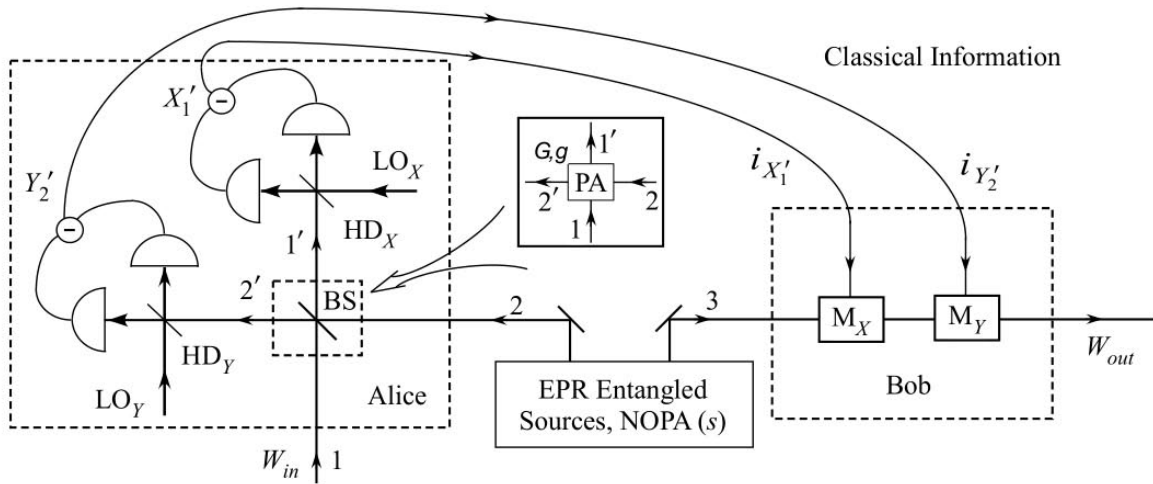


Figure 6.1. Schematics for the continuous-variable quantum state teleportation with a parametric amplifier (PA, inset) in place of a beam splitter (BS) (Adapted from Ref.[65]). NOPA: non-degenerate optical parametric amplifier; HD: homodyne detection; LO: local oscillator.

6.2 Application to Quantum State Teleportation

Consider the scheme shown in Fig.6.1 for quantum state teleportation with continuous variables. This is the scheme that makes a complete unconditioned state teleportation (even for vacuum state) [27], [31] in comparison [27] with the teleportation scheme of polarization states [28], [30]. In this scheme, an EPR entangled source in the form of Eq.(6.8) of strength characterized by s is produced from a NOPA and its two entangled fields (2 and 3) are sent to Alice and Bob, respectively. Bell projection measurement is performed with a beam splitter (BS) to mix the unknown state (field 1) to be teleported with one of the fields (field 2) of the EPR-entangled state, which is described in Eq.(6.8). The results $(i_{X1'}, i_{Y2'})$ of Bell measurement are sent by Alice via classical channel to Bob, who modifies field 3 (M_X, M_Y) to recover the original input state characterized by Wigner function W_{in} .

It has been shown that PA-assisted homodyne measurement can make the same quantum correlation measurement as the homodyne measurement [60]. So, let us now replace the BS with a PA of gain parameters G, g , shown in the inset of Fig.6.1. Using Eq.(6.8) for the EPR entangled state with a strength of s and labeling of the fields in Fig.6.1, we find the input state of the PA is described by the Wigner function:

$$\begin{aligned}
 W_{in}(x_1, y_1; x_2, y_2; x_3, y_3) &= \frac{1}{(2\pi)^2} e^{-\frac{1}{4}[(x_3+x_2)^2+(y_3-y_2)^2]e^{2s}} \\
 &\times e^{-\frac{1}{4}[(x_3-x_2)^2+(y_3+y_2)^2]e^{-2s}} W_{in}(x_1, y_1).
 \end{aligned} \tag{6.12}$$

From Eq.(6.6), the Wigner function after the PA becomes

$$\begin{aligned}
 W_{out}(x'_1, y'_1; x'_2, y'_2; x_3, y_3) &= \frac{1}{(2\pi)^2} e^{-\frac{1}{4}[(x_3+Gx'_2-gx'_1)^2+(y_3-gy'_1-Gy'_2)^2]e^{2s}} \\
 &\times e^{-\frac{1}{4}[(x_3-Gx'_2+gx'_1)^2+(y_3+gy'_1+Gy'_2)^2]e^{-2s}} \\
 &\times W_{in}(Gx'_1 - gx'_2, Gy'_1 + gy'_2).
 \end{aligned} \tag{6.13}$$

Now we make homodyne measurements of \hat{X}'_1 and \hat{Y}'_2 of the PA output fields. With a result of $i_{X'_1}$ and $i_{Y'_2}$, the state in field 3 (other field of the EPR-entangled state) is projected to a state described by the density operator:

$$\hat{\rho}_{proj} = \text{Tr}_{1'2'}(|i_{X'_1}, i_{Y'_2}\rangle\langle i_{X'_1}, i_{Y'_2}| \hat{\rho}_{sys}), \quad (6.14)$$

where $|i_{X'_1}, i_{Y'_2}\rangle$ is the common eigen state of \hat{X}'_1 and \hat{Y}'_2 . The Wigner function of the projected state is then

$$\begin{aligned} W_{proj}(x_3, y_3) &= \int dx'_2 dy'_1 W_{out}(x'_1, y'_1; x'_2, y'_2; x_3, y_3)|_{x'_1=i_{X'_1}, y'_2=i_{Y'_2}} \\ &= \int \frac{dx'_2 dy'_1}{(2\pi)^2} e^{-\frac{1}{4}[(x_3+Gx'_2-gi_{X'_1})^2+(y_3-gy'_1-Gi_{Y'_2})^2]} e^{2s} \\ &\quad \times e^{-\frac{1}{4}[(x_3-Gx'_2+gi_{X'_1})^2+(y_3+gy'_1+Gi_{Y'_2})^2]} e^{-2s} \\ &\quad \times W_{in}(Gi_{X'_1} - gx'_2, Gy'_1 + gi_{Y'_2}) \end{aligned} \quad (6.15)$$

Combining the common terms in the integral above, we obtain

$$\begin{aligned} W_{proj}(x_3, y_3) &= \frac{e^{-\frac{x_3^2+y_3^2}{2\cosh 2s}}}{(2\pi)^2} \int dx'_2 dy'_1 e^{-\frac{\cosh 2s}{2}(Gx'_2+x_3 \tanh 2s-gi_{X'_1})^2} \\ &\quad \times e^{-\frac{\cosh 2s}{2}(gy'_1+Gi_{Y'_2}-y_3 \tanh 2s)^2} \\ &\quad \times W_{in}(Gi_{X'_1} - gx'_2, Gy'_1 + gi_{Y'_2}). \end{aligned} \quad (6.16)$$

Taking the limit of $s \gg 1$ so that $\cosh 2s \gg 1$, we can approximate the Gaussian functions in the integral above with δ -functions. Then we have

$$\begin{aligned} W_{proj}(x_3, y_3) &= \frac{1}{2\pi \cosh 2s} e^{-\frac{1}{2\cosh 2s}(x_3^2+y_3^2)} \\ &\quad \times \int dx'_2 dy'_1 \delta(Gx'_2 + x_3 \tanh 2s - gi_{X'_1}) \\ &\quad \times \delta(gy'_1 + Gi_{Y'_2} - y_3 \tanh 2s) \\ &\quad \times W_{in}(Gi_{X'_1} - gx'_2, Gy'_1 + gi_{Y'_2}) \end{aligned}$$

$$\begin{aligned}
&= \frac{1}{2\pi G g \cosh 2s} e^{-\frac{1}{2\cosh 2s}(x_3^2 + y_3^2)} \\
&\quad \times W_{in}\left(\frac{g}{G}x_3 \tanh 2s + \frac{i_{X'_1}}{G}, \frac{G}{g}y_3 \tanh 2s - \frac{i_{Y'_2}}{g}\right). \tag{6.17}
\end{aligned}$$

When $g \gg 1$ so that $G = \sqrt{1+g^2} \approx g$, we have $g/G \approx G/g \approx 1$. Furthermore, if $\sqrt{\cosh 2s} \gg \text{Max}\{1, \text{the range of } W_{in}(x_3, y_3)\}$, we have $\tanh 2s \approx 1$ and $\cosh 2s \gg x_3^2 + y_3^2$ so that $e^{-\frac{1}{2\cosh 2s}(x_3^2 + y_3^2)} \approx 1$ within the range of $W_{in}(x_3, y_3)$. Then Eq.(6.17) becomes

$$\begin{aligned}
&W_{proj}(x_3, y_3) \\
&\simeq \frac{1}{2\pi G g \cosh 2s} W_{in}\left(x_3 + \frac{i_{X'_1}}{G}, y_3 - \frac{i_{Y'_2}}{g}\right). \tag{6.18}
\end{aligned}$$

The case of finite G and s is dealt with in Appendix 6.A and it is shown that the limits of $G \gg 1$ and $s \gg 1$ are independent. With the detection outcomes of $i_{X'_1}, i_{Y'_2}$, we transmit these measurement result through a classical channel to the location of field 3 and a displacement operation of $x_3 + \frac{i_{X'_1}}{G} \rightarrow x_3, y_3 - \frac{i_{Y'_2}}{g} \rightarrow y_3$ (M_X, M_Y in Fig.6.1) can be performed on field 3, leading to the displaced Wigner function as

$$W_{proj}^{disp}(x_3, y_3) \propto W_{in}(x_3, y_3). \tag{6.19}$$

This recovers the Wigner function of the input state thus achieving quantum state teleportation. So, we just showed that the quantum state teleportation scheme still works even after we replace the BS with a high gain PA. Note that the condition $G = \sqrt{1+g^2} \approx g$ is equivalent to $t = r = 1/\sqrt{2}$, which is required for the scheme with a BS.

6.3 Tolerance to Detection Loss

The quantum teleportation process involves homodyne detection which may introduce losses through detectors' less-than-unit quantum efficiency and imperfect mode matching to the local oscillator fields. It was known that PA-assisted homodyne measurement is tolerant to detection and propagation losses [60]. We will discuss the influence of these losses in this section. Let us start with the traditional BS scheme. This case was treated in Ref.[27] so we will only present the result here for the comparison with the PA case.

Given the input state in Eq.(6.12) and using the relation in Eq.(6.7), we can find the Wigner function after the 50:50 beam splitter of Bell measurement. We then introduce detection losses by using a beam splitter model with the same transmissivity η for both output fields 1' and 2' right before detection. Since the homodyne detection is on the x -quadrature of field 1' and y -quadrature of field 2', we can leave y'_1, x'_2 unchanged and integrate them out so that we only consider effect on x'_1, y'_2 together with the vacuum from the unused port of the beam splitter: $x'_1 \rightarrow \eta x''_1 + \sqrt{1-\eta^2} x'_{v1}$, $y'_2 \rightarrow \eta y''_2 + \sqrt{1-\eta^2} y'_{v2}$, $x_{v1} \rightarrow \eta x'_{v1} - \sqrt{1-\eta^2} x''_1$, $y_{v2} \rightarrow \eta y'_{v2} - \sqrt{1-\eta^2} y''_2$. Here, $\hat{a}'_{v1}, \hat{a}'_{v2}$ are the vacuum coupled in through loss. For the homodyne measurement with result of $x''_1 = i_{X'_1}$, $y''_2 = i_{Y'_2}$, we obtain the Wigner function for the projected state of field 3 by setting $x''_1 = i_{X'_1}$, $y''_2 = i_{Y'_2}$ and integrating the variables $y'_1, x'_2, x'_{v1}, y'_{v2}$. In the limit of $\cosh 2s \gg 1$, the projected Wigner function is

$$\begin{aligned}
& W_{proj}^{(BS)}(x_3, y_3) \\
& \propto \int dx dy W_{in}(x, y) e^{-\frac{1}{2\sigma_1^2} [(x - \frac{\sqrt{2}i_{X'_1}}{\eta} - x_3)^2 + (y - \frac{\sqrt{2}i_{Y'_2}}{\eta} - y_3)^2]}.
\end{aligned} \tag{6.20}$$

where $\sigma_1^2 = 2\frac{1-\eta^2}{\eta^2} + \frac{1}{\cosh 2s}$. In the ideal case of no loss, we have $\eta = 1$ and for large s , the Gaussian in Eq.(6.20) becomes a δ -function so that after the required displacement of $x_3 + \frac{\sqrt{2}i_{X'_1}}{\eta} \rightarrow x_3, y_3 + \frac{\sqrt{2}i_{Y'_2}}{\eta} \rightarrow y_3$ upon receiving of the detection outputs $i_{X'_1}, i_{Y'_2}$, we recover the input Wigner function $W_{in}(x_3, y_3)$. But with finite detection losses, vacuum noise will come into the quantum teleportation channel so even in the limit of large s , we have

$$\begin{aligned}
& W_{proj}^{(BS)}(x_3, y_3) \\
& \propto \int dx dy W_{in}(x, y) e^{-\frac{\eta^2}{4(1-\eta^2)} [(x-x_3)^2 + (y-y_3)^2]},
\end{aligned} \tag{6.21}$$

which involves a convolution with the vacuum Wigner function. Equation (6.21) was first derived in Ref.[27].

For the scheme with a PA in place of the BS, we introduce losses after the output of the PA but before the homodyne measurement. From Eq.(6.16) and similar procedure to

Eq.(6.20) but without $\cosh 2s \gg 1$ assumption, we have the projected Wigner function of field 3 after the homodyne measurement of results $x'_1 = i_{X'_1}, y'_2 = i_{Y'_2}$:

$$\begin{aligned}
W_{proj}^{(PA)}(x_3, y_3) &= \frac{1}{(2\pi)^3} e^{-\frac{1}{2\cosh 2s}(x_3^2 + y_3^2)} \int dx'_2 dy'_1 dx'_{v1} dy'_{v2} e^{-\frac{\cosh 2s}{2}[Gx'_2 + x_3 \tanh 2s - g(\eta i_{X'_1} + \sqrt{1-\eta^2} x'_{v1})]^2} \\
&\times e^{-\frac{\cosh 2s}{2}[gy'_1 + G(\eta i_{Y'_2} + \sqrt{1-\eta^2} y'_{v2}) - y_3 \tanh 2s]^2} e^{-\frac{1}{2}[(\eta x'_{v1} - \sqrt{1-\eta^2} i_{X'_1})^2 + (\eta y'_{v2} - \sqrt{1-\eta^2} i_{Y'_2})^2]} \\
&\times W_{in}(G(\eta i_{X'_1} + \sqrt{1-\eta^2} x'_{v1}) - gx'_2, Gy'_1 + g(\eta i_{Y'_2} + \sqrt{1-\eta^2} y'_{v2})).
\end{aligned} \tag{6.22}$$

Now we make a change of integral variables from x'_2, y'_1 to $x = G(\eta i_{X'_1} + \sqrt{1-\eta^2} x'_{v1}) - gx'_2, y = Gy'_1 + g(\eta i_{Y'_2} + \sqrt{1-\eta^2} y'_{v2})$. After integrating over x'_{v1}, y'_{v2} , we obtain the projected Wigner function in the form of

$$\begin{aligned}
W_{proj}^{(PA)}(x_3, y_3) &\propto e^{-\frac{1}{2\cosh 2s}(x_3^2 + y_3^2)} \int dx dy W_{in}(x, y) \\
&\times e^{-\frac{1}{2\sigma_{2x}^2}(x - \frac{i_{X'_1}}{\eta G} - \frac{gx_3}{G} \tanh 2s)^2} e^{-\frac{1}{2\sigma_{2y}^2}(y + \frac{i_{Y'_2}}{\eta g} - \frac{Gy_3}{g} \tanh 2s)^2}.
\end{aligned} \tag{6.23}$$

where $\sigma_{2x}^2 = \frac{1-\eta^2}{\eta^2 G^2} + \frac{g^2}{G^2 \cosh 2s}$, $\sigma_{2y}^2 = \frac{1-\eta^2}{\eta^2 g^2} + \frac{G^2}{g^2 \cosh 2s}$. Setting $G \gg 1$ and $s \gg 1$ so that $G \approx g$ and $\tanh 2s \approx 1, \cosh 2s \gg 1$ and making the displacement operation of $x_3 + i_{X'_1}/\eta g \rightarrow x_3$ and $y_3 - i_{Y'_2}/\eta G \rightarrow y_3$, we have

$$\begin{aligned}
W_{proj}^{(PA)}(x_3, y_3) \\
\propto \int dx dy W_{in}(x, y) e^{-\frac{1}{2\sigma_2^2}[(x-x_3)^2 + (y-y_3)^2]},
\end{aligned} \tag{6.24}$$

where $\sigma_2^2 \equiv \frac{1-\eta^2}{\eta^2 G^2} + \frac{1}{\cosh 2s} \approx \sigma_{2x}^2 \approx \sigma_{2y}^2$. Notice that the conditions of $G \approx g$ and $s \gg 1$ are independent of each other (see more in Appendix 6.A). Comparing σ_2^2 with σ_1^2 in Eq.(6.20) for the BS scheme, we find the PA scheme reduces the effect of losses by a factor of $2G^2$. If $G^2 \sim (1-\eta^2)e^{2s}/2\eta^2$, we have $\sigma_2^2 \rightarrow 4e^{-2s}$, which is similar to the lossless case ($\eta = 1$) of Eq.(6.20). Therefore, the effect of losses can be mitigated by large G .

6.4 Influence of Losses via Fidelity

To quantify the influence of losses and the gain size of PA in place of BS, we consider the fidelity of teleportation. For a pure input state $|\phi_{in}\rangle$ and an output described by density operator $\hat{\rho}_{out}$, it is given by [28]

$$F = \langle \phi_{in} | \hat{\rho}_{out} | \phi_{in} \rangle. \quad (6.25)$$

Note that if the output state is same as the input: $\hat{\rho}_{out} = |\phi_{in}\rangle\langle\phi_{in}|$, Eq.(6.25) gives $F = 1$.

Since the roles of G and s are independent of each other, for the simplicity of argument and emphasis on the effect of the PA, we set $s \rightarrow \infty$ here. The case of finite s will be presented in Appendix 6.A and the conclusion is similar to the case of $s \rightarrow \infty$.

6.4.1 Scheme with Beam Splitter

Consider the quantum state teleportation scheme as the quantum channel. For the case of using a BS for Bell measurement and with large s , the Wigner function of the output is connected to the input by Eq.(6.21) and is rewritten as

$$W_{out} = W_{in} \circ G_{\bar{\sigma}_1} \quad (6.26)$$

with \circ denoting convolution and $G_{\bar{\sigma}_1}$ as the two dimensional Gaussian distribution with a variance $\bar{\sigma}_1^2 = 2(1-\eta^2)/\eta^2$. The teleportation input-output relation for the Wigner functions described by Eq.(6.26) can also be cast in the density operator form as (See Appendix 6.A.2)

$$\hat{\rho}_{out} = \int dx dy \hat{D}\left(\frac{x + yj}{2}\right) \hat{\rho}_{in} \hat{D}^\dagger\left(\frac{x + yj}{2}\right) G_{\bar{\sigma}_1}(x, y), \quad (6.27)$$

where operator $\hat{D}(\alpha) \equiv \exp(\alpha \hat{a}^\dagger - \alpha^* \hat{a})$ is the displacement operator ($\alpha = (x + jy)/2$).

From Eq.(6.25), we find the fidelity for a pure state input is then

$$F = \int dx dy |\chi_{in}(x, y)|^2 G_{\bar{\sigma}_1}(x, y), \quad (6.28)$$

where $\chi_{in}(x, y) = \langle \phi_{in} | \hat{D}(\frac{x+yj}{2}) | \phi_{in} \rangle$, which is the single-mode characteristic function defined in Eq.(6.45) for the input state's Wigner function.

We can now evaluate the fidelity for a number of known input states. First for coherent state, it is easy to obtain the fidelity as

$$F = \frac{1}{1 + \bar{\sigma}_1^2/2} \quad (6.29)$$

with $\bar{\sigma}_1^2 \equiv 2(1 - \eta^2)/\eta^2$. For Fock state $|N\rangle$,

$$\begin{aligned} |\chi_{in}(x, y)|^2 &= |\langle N | \hat{D}\left(\frac{x+yj}{2}\right) | N \rangle|^2 \\ &= \left| \int dx' f_N^*(x') f_N(x' - x/\sqrt{2}) e^{j\frac{y(x'-x/\sqrt{2})}{\sqrt{2}}} \right|^2, \end{aligned} \quad (6.30)$$

where

$$f_N(x) = \frac{\pi^{-1/4}}{\sqrt{2^N N!}} e^{-x^2/2} H_N(x) \quad (6.31)$$

with $H_N(x)$ as the N th-order Hermite polynomials. We can then evaluate numerically fidelity F with Eq.(6.28) for a given loss modeled by a BS with transmission coefficient η . Figure 6.2 plots the dependence of F as a function of η for a coherent state of $\alpha = 3 + 3j$ and Fock states of $N = 1, 3, 5$, showing a fast drop of F with the increase of loss (decrease of η). The rate of drop is especially large for number states with higher photon numbers as compared to the coherent state (dashed curve). Thus, nonclassical states are more sensitive to loss in the teleportation process.

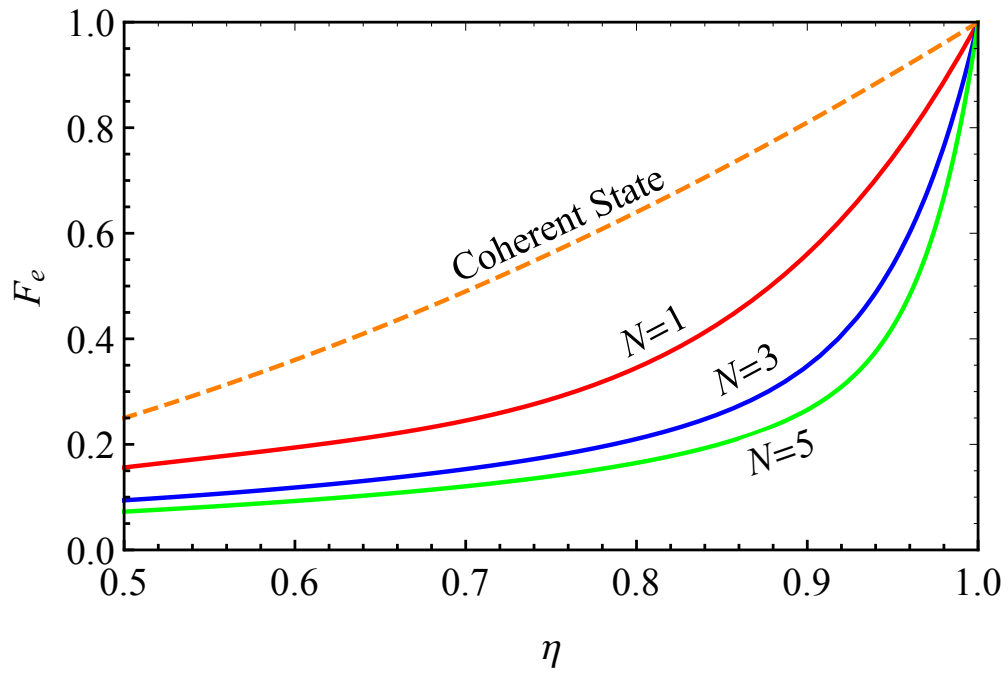


Figure 6.2. Fidelity F as a function of detection loss in the teleportation scheme with a BS for a coherent state $|\alpha\rangle$ with $\alpha = 3 + 3j$ (dashed line) and Fock states of $N = 1, 3, 5$ (Adapted from Ref.[65]).

6.4.2 Scheme with Parametric Amplifier

Next we consider the teleportation scheme with aid of a PA but having losses $1 - \eta$ before detection. The output is related to input by Eq.(6.23) but with $s \gg 1$ and can be rewritten in the form of Eq.(6.26) as

$$W_{out}(x, y) = \int dx' dy' W_{in}\left(x \frac{g}{G} - x', y \frac{G}{g} - y'\right) \times G_{\bar{\sigma}_{2x}}(x') G_{\bar{\sigma}_{2y}}(y'), \quad (6.32)$$

where $\bar{\sigma}_{2x}^2 \equiv (1 - \eta^2)/\eta^2 G^2$, $\bar{\sigma}_{2y}^2 \equiv (1 - \eta^2)/\eta^2 g^2$. Then Eq.(6.27) is changed to (See Appendix 6.A.2)

$$\hat{\rho}_{out} = \int dx dy \hat{S}(\epsilon) \hat{D}\left(\frac{x + yj}{2}\right) \hat{\rho}_{in} \hat{D}^\dagger\left(\frac{x + yj}{2}\right) \times \hat{S}^\dagger(\epsilon) G_{\bar{\sigma}_{2x}}(x) G_{\bar{\sigma}_{2y}}(y), \quad (6.33)$$

where $\hat{S}(\epsilon) \equiv \exp[\epsilon(\hat{a}^{\dagger 2} - \hat{a}^2)/2]$ is the squeezing operator with $\epsilon \equiv \ln(G/g)$, and Eq.(6.28) is modified to

$$F = \int dx dy |\chi_{PA}(x, y)|^2 G_{\bar{\sigma}_{2x}}(x) G_{\bar{\sigma}_{2y}}(y) \quad (6.34)$$

with $\chi_{PA}(x, y) = \langle \phi_{in} | \hat{S}(\epsilon) \hat{D}\left(\frac{x + yj}{2}\right) | \phi_{in} \rangle$.

For a coherent state $|\alpha\rangle$, we have

$$\begin{aligned} |\chi_{PA}^{(\alpha)}(x, y)|^2 &= |\langle \alpha | \hat{S}(\epsilon) \hat{D}\left(\frac{x + yj}{2}\right) | \alpha \rangle|^2 \\ &= |\langle \alpha | \hat{S}(\epsilon) | \alpha + \frac{x + yj}{2} \rangle|^2. \end{aligned} \quad (6.35)$$

Setting $\alpha = a + bj$, we then obtain from Eq.(6.34) with some manipulation

$$\begin{aligned} F &= \frac{2 \exp\left[-\frac{2a^2(1-g/G)^2}{1+g^2/G^2+\bar{\sigma}_{2x}^2} - \frac{2b^2(1-G/g)^2}{1+G^2/g^2+\bar{\sigma}_{2y}^2}\right]}{\sqrt{(1+g^2/G^2+\bar{\sigma}_{2x}^2)(1+G^2/g^2+\bar{\sigma}_{2y}^2)}} \\ &\approx \frac{\exp\left[-\frac{1}{4G^4} \frac{a^2+b^2}{1+\bar{\sigma}_2^2/2}\right]}{1+\bar{\sigma}_2^2/2} \quad \text{for } G \gg 1, \end{aligned} \quad (6.36)$$

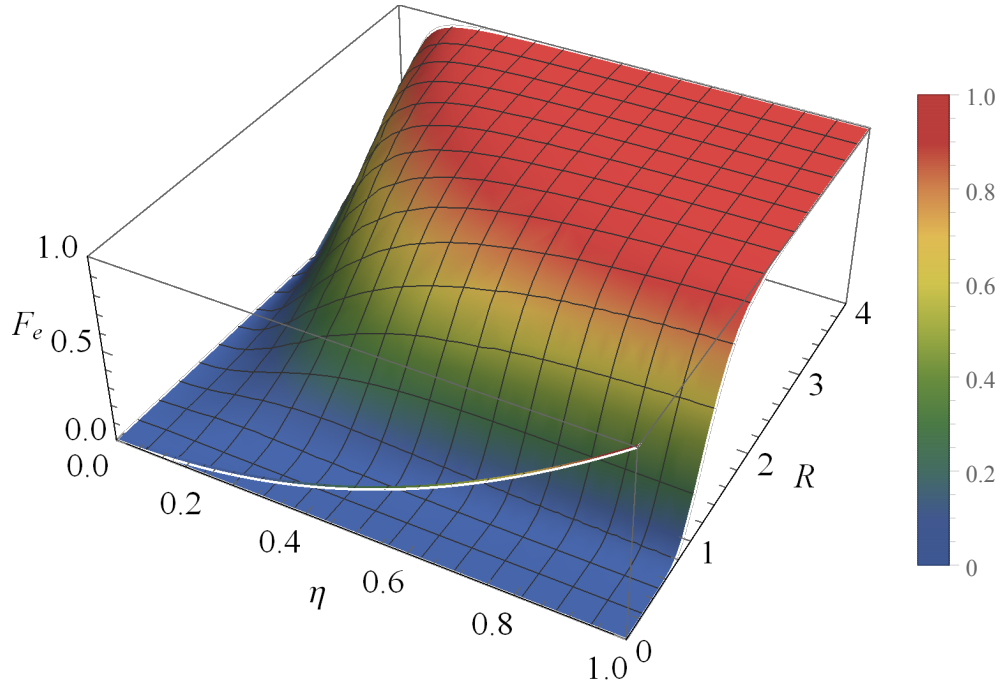


Figure 6.3. Three-dimensional plot of fidelity F as a function of transmission η (opposite of loss) and gain parameter R ($G \equiv \cosh R$) of the PA used in Bell measurement for teleportation of the coherent state $|\alpha\rangle$ with $\alpha = 3 + 3j$ (Adapted from Ref.[65]). The light curve at $R = 0$ corresponds to the case of using a beam splitter for the Bell measurement (the dashed line in Fig.6.2).

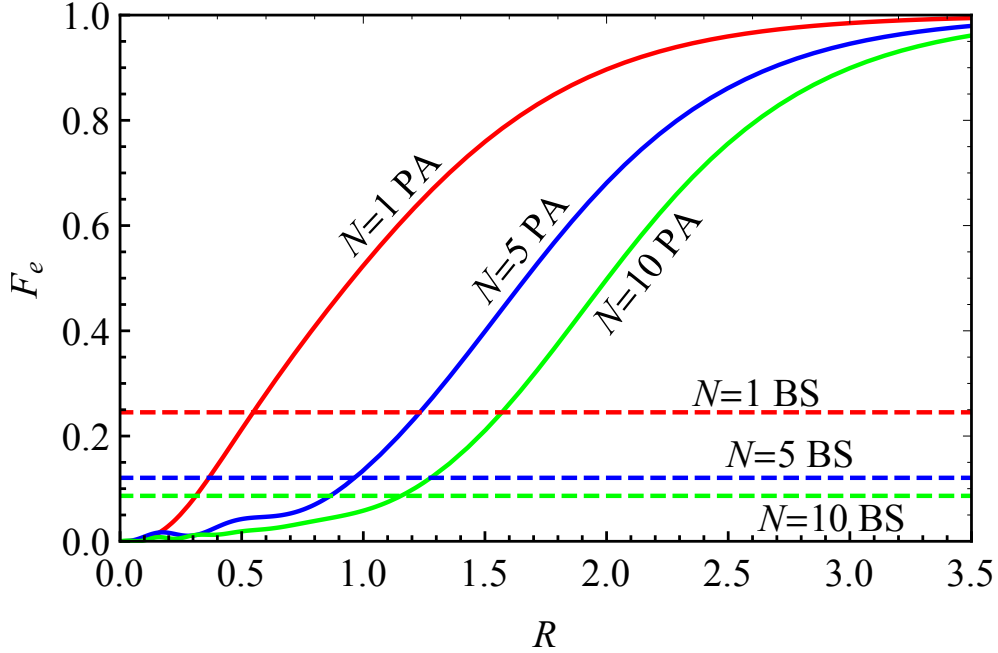


Figure 6.4. Fidelity F as a function of gain of PA at a loss of $\eta = 0.7$ for Fock state $|N\rangle$ with $N = 1, 5, 10$. The dashed lines are for the BS scheme (Adapted from Ref.[65]).

where $\bar{\sigma}_2^2 \equiv (1 - \eta^2)/\eta^2 G^2$. When G tends to a large value, we have $G \sim g$ and Eq.(6.36) approaches Eq.(6.29) but with $\bar{\sigma}_1^2$ replaced by $\bar{\sigma}_2^2$, which goes to zero as G becomes large. Hence, $F \rightarrow 1$ for large G and independent of the loss η . So, with the aid of a PA of large gain, the effect of detection loss can be reduced to zero. This is demonstrated in Fig.6.3 as the red region ($F \sim 1$) in the 3-D plot of F as a function of η and the gain-related parameter R with $G \equiv \cosh R$ (or $R \equiv \ln(G + \sqrt{G^2 - 1})$). Figure 6.3 is obtained from the first expression in Eq.(6.36) without approximation. The red region extends to low value of η (< 0.5 , large loss) at high gain ($R > 2$). The light colored curve at $R = 0$ is for the case when we use a beam splitter for Bell measurement (the dashed line in Fig.6.2). In this case, as can be seen, F drops fast as η decreases.

On the other hand, even with no detection loss ($\eta = 1, \bar{\sigma}_{2x} = \bar{\sigma}_{2y} = 0$) but a finite G , we have from Eq.(6.36)

$$\begin{aligned} F &= \frac{2Gg}{G^2 + g^2} \exp \left[-2 \frac{(G-g)^2}{G^2 + g^2} (a^2 + b^2) \right] \\ &\approx \exp \left[-(a^2 + b^2)/4G^4 \right] \quad \text{for } G \gg 1. \end{aligned} \quad (6.37)$$

The blue region (low $F < 0.15$) in Fig.6.3 extends to high η value when $R < 1$ for relatively low gain, which indicates that high gain ($R > 2$) is required for the PA-assisted scheme. From Eq.(6.37), we find that in order to have $F \approx 1$, we need $G^2 \gg \sqrt{a^2 + b^2} = |\alpha|$, that is, the larger the average the photon number, the bigger the gain G needs to be. This behavior is not limited to coherent states as we will see next for photon number Fock states.

Next we look at the nonclassical states of Fock state $|N\rangle$. The characteristic function χ_{PA} in Eq.(6.34) has the form of

$$\begin{aligned} |\chi_{PA}^{(N)}(x, y)|^2 &= |\langle N | \hat{S}(\epsilon) \hat{D}\left(\frac{x + jy}{2}\right) | N \rangle|^2 \\ &= \left| \int dx' \sqrt{\tanh R} e^{-jy[(x'/\sqrt{2})\tanh(\epsilon) + x/2]} \right. \\ &\quad \left. \times f_N^*(x') f_N(-x' \tanh(\epsilon) - x/\sqrt{2}) \right|^2, \end{aligned} \quad (6.38)$$

where the definition of $f_N(x)$ is the same as Eq.(6.31). The fidelity can be calculated numerically from Eq.(6.34). We plot in Fig.6.4 the fidelity F as a function of the gain-related parameter R for Fock states $|N\rangle$ with $N = 1, 5, 10$, respectively. The detection loss is set with transmission $\eta = 0.7$. As can be seen, larger gain (R value) is needed for higher N to reach $F \approx 1$, similar to the case of coherent states as predicted by the second line of Eq.(6.37). We also plot in Fig.6.4 the corresponding values of F for the BS scheme (dashed lines) for comparison, demonstrating the effect of PA to counter the detrimental effect of detection loss. The effect of loss on the Fock state $|5\rangle$ is displayed in Fig.6.5, where we plot F as a function of transmission coefficient η for $R = 1, 2, 3$ ($G = 1.54, 3.76, 10.07$), respectively. The result of the BS scheme (dashed line) is also plotted for comparison. As expected, PA-assisted scheme is no good for the case of relatively low gain ($R = 1, 2$). But with $R = 3$, it keeps relatively high F value (> 0.8) even at a large loss of 50% ($\eta = 0.5$).

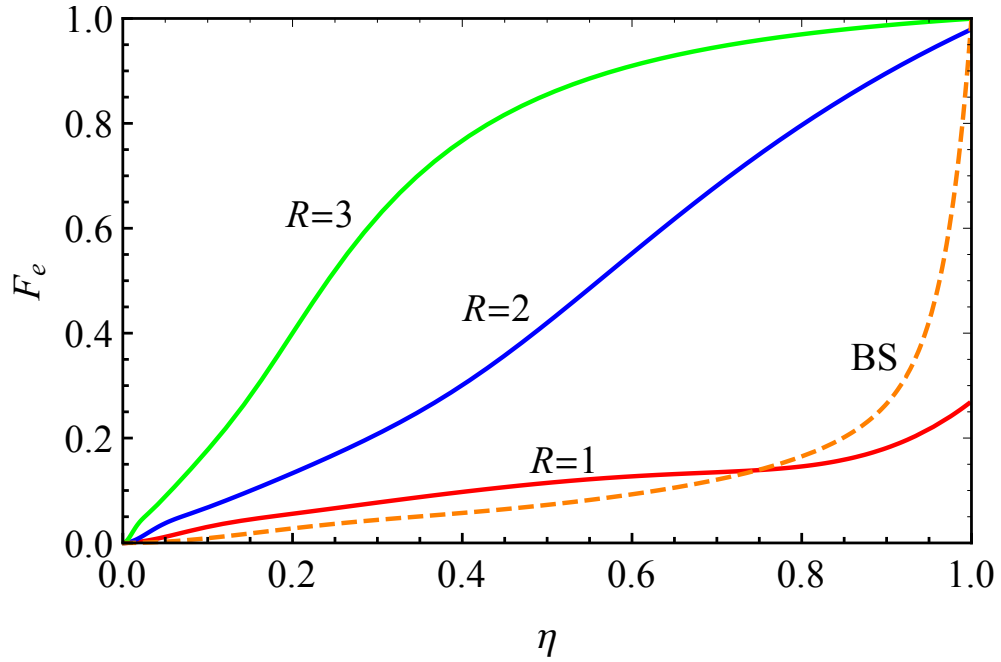


Figure 6.5. Fidelity F as a function of transmission η for Fock state $|N\rangle$ with $N = 5$ at gain of $R = 1, 2, 3$ ($G = 1.54, 3.76, 10.07$) for the PA-assisted scheme. The case of BS scheme is plotted as the dashed line for comparison (Adapted from Ref.[65]).

6.5 Influence of Loss on Entanglement

The input states in the previous sections are all pure states. In quantum communication, we more often transmit one field of entangled fields, as in, for example, entanglement swapping protocol [66]–[68]. The transmitted field is usually in a mixed state when the other entangled field is not considered. We will examine how losses in the two teleportation schemes will affect the transmission of an EPR-type of entangled states which is simply a two-mode squeezed state with a Wigner function given in Eq.(6.8).

6.5.1 Fidelity

For an input field that is entangled with another field, after tracing out the other field, it becomes a mixed state described by density operator $\hat{\rho}_{in}$. In this case, we cannot use Eq.(6.25) or its density operator form: $F' = \text{Tr}(\hat{\rho}_{in}\hat{\rho}_{out})$, for even in the ideal transmitted case of $\hat{\rho}_{out} = \hat{\rho}_{in}$, $F' = \text{Tr}(\hat{\rho}_{in}^2) \neq 1$ for mixed states. A widely used definition of fidelity for mixed states was given by Jozsa as $F_m = \text{Tr}[\sqrt{\sqrt{\hat{\rho}_{in}}\hat{\rho}_{out}\sqrt{\hat{\rho}_{in}}}]^2$ [69]. But this definition does not consider entanglement with the other field.

On the other hand, we can use the entanglement fidelity [70], which quantifies how well a quantum (teleportation) channel, which may interact with the environment E, preserves the transferred input state (in a state space denoted as Q) and its entanglement with another system in the space of R. The input state ($\hat{\rho}_{in}$) can be obtained by taking partial trace of an entangled pure state on a larger Hilbert space (a joint space of Q and the entangled space R) over the space R. For the case of no entanglement, the input state is then a pure state. According to Ref.[70], the entanglement fidelity only depends on the initial quantum state and the dynamic evolution of the input state on Q through the quantum channel. Suppose the general quantum evolution of the state on Q through the quantum channel can be cast in the form of $\hat{\rho}_{out} = \sum_k \hat{A}_k \hat{\rho}_{in} \hat{A}_k^\dagger$ by some operator-sum representation with \hat{A}_k being a collection of operators acting in the space of Q and satisfying the completeness relation $\sum_k \hat{A}_k^\dagger \hat{A}_k = 1$. Then, entanglement fidelity is defined as [70]

$$F_e = \sum_k \text{Tr}(\hat{A}_k \hat{\rho}_{in}) \text{Tr}(\hat{A}_k^\dagger \hat{\rho}_{in}). \quad (6.39)$$

For the special case of a pure input state $\hat{\rho}_{in} = |\phi_{in}\rangle\langle\phi_{in}|$, we have $F_e = \sum_k |\langle\phi_{in}|\hat{A}_k|\phi_{in}\rangle|^2 = \langle\phi_{in}|\hat{\rho}_{out}|\phi_{in}\rangle$, which recovers Eq.(6.25).

In our derivation of the output Wigner function for both teleportation protocols, the output density operators of Eqs.(6.27,6.33) have already been written in the form of $\hat{\rho}_{out} = \sum_k \hat{A}_k \hat{\rho}_{in} \hat{A}_k^\dagger$ with $\hat{A}_k \equiv \hat{D}(\frac{x+jy}{2})$ and $\hat{S}(\epsilon)\hat{D}(\frac{x+jy}{2})$ for the BS and PA schemes, respectively. Note that the sum over k is replaced by integral over x, y .

To obtain $\hat{\rho}_{in}$ for Eq.(6.39), we just need to take partial trace of the other field component of the density operator of the entangled states. For the EPR state (a two-mode squeezed state) in Eq.(6.8), the signal field becomes a thermal state with an average photon number $\bar{n} = \sinh^2(s)$. Its density operator can be expressed with P -Representation as $\hat{\rho}_{in} = \int d^2\alpha P(\alpha) |\alpha\rangle\langle\alpha|$, where $P(\alpha) = \frac{1}{\pi\bar{n}} e^{-|\alpha|^2/\bar{n}}$. The entanglement fidelity F_e can be obtained from Eqs. (6.28) and (6.34) with the characteristic functions being

$$\begin{aligned} & |\chi_{BS}(x, y)|^2 \\ &= \left| \int d^2\alpha P(\alpha) \langle\alpha| \hat{D}(\frac{x+yj}{2}) |\alpha\rangle \right|^2 \\ &= \left| \int d^2\alpha \frac{1}{\pi\bar{n}} e^{-|\alpha|^2/\bar{n}} \right. \\ &\quad \left. \times e^{[(x+yj)\alpha^* - (x-yj)\alpha]/2 - (x^2+y^2)/8} \right|^2 \end{aligned} \quad (6.40)$$

for the BS scheme and

$$\begin{aligned} & |\chi_{PA}(x, y)|^2 \\ &= \left| \int d^2\alpha P(\alpha) \langle\alpha| \hat{S}(\epsilon)\hat{D}(\frac{x+yj}{2}) |\alpha\rangle \right|^2 \\ &= \left| \int d^2\alpha \frac{1}{\pi\bar{n}} e^{-|\alpha|^2/\bar{n}} e^{[(x+yj)\alpha^* - (x-yj)\alpha]/4} \right. \\ &\quad \left. \times \langle\alpha| \hat{S}(\epsilon) |\alpha + \frac{x+yj}{2}\rangle \right|^2 \end{aligned} \quad (6.41)$$

for the PA-assisted scheme. Figure 6.6 shows the results of calculation. It is very similar to Fig.6.5 for the number state case.

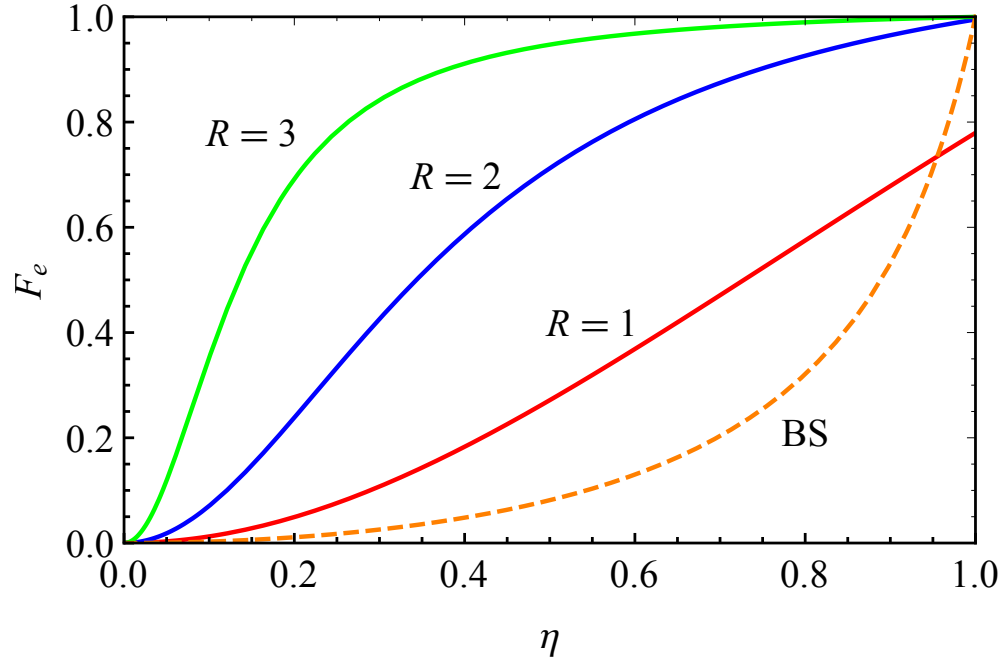


Figure 6.6. Entanglement fidelity F_e as a function of transmission η for a thermal state (one field of the EPR-entangled two-mode squeezed state) with average photon number $\bar{n} = \sinh^2(-1) = 1.38$ for the PA-assisted scheme with gain parameters of $R = 1, 2, 3$ (solid) and for the BS scheme (dashed) (Adapted from Ref.[65]).

6.5.2 Inseparability

Another way to see how entanglement is affected by teleportation protocols is to check the inseparability criterion through parameter I_s defined as [71]

$$I_s \equiv \langle \Delta^2(\hat{X}_1 - \hat{X}_2) \rangle + \langle \Delta^2(\hat{Y}_1 + \hat{Y}_2) \rangle. \quad (6.42)$$

For un-entangled fields, it has a minimum value of $I_s^{(0)} = 4$ for vacuum. $I_s < I_s^{(0)} = 4$ gives the criterion for entanglement between two fields and the smaller the value of I_s is, the more entangled are the two fields. The ideal value is $I_s = 0$, showing perfect EPR correlation between \hat{X}_1, \hat{X}_2 and between \hat{Y}_1, \hat{Y}_2 . For the EPR entangled state given in Eq.(6.8) with $s = -1$, we have normalized value $I_s^{EPR}/I_s^{(0)} = 0.135 = -8.69\text{dB}$. We will teleport one of the two entangled fields, say the signal beam, through the BS or PA-assisted teleportation scheme.

The Wigner functions of the output state are given by Eq.(6.26) and (6.32) as

$$W_{out} = \int dx' dy' W_{in}(x_1, y_1; x'_2 - x', y'_2 - y') \\ \times G_{\sigma'_x}(x') G_{\sigma'_y}(y'), \quad (6.43)$$

with $x'_2 = x_2$, $y'_2 = y_2$, $\sigma'_x = \sigma'_y = \bar{\sigma}_1$ for the BS scheme and $x'_2 = x_2 \frac{g}{G}$, $y'_2 = y_2 \frac{G}{g}$, $\sigma'_x = \bar{\sigma}_{2x}$, $\sigma'_y = \bar{\sigma}_{2y}$ for the PA-assisted scheme. We calculate I_s^{out} between the teleported signal field and the original idler field to examine how entanglement is affected by teleportation. $I_s^{out} = \langle \Delta^2 X_- \rangle_{out} + \langle \Delta^2 Y_+ \rangle_{out}$ with $X_- = x_1 - x_2$ and $Y_+ = y_1 + y_2$ is calculated from Wigner function by

$$\langle A \rangle_{out} = \int dx_1 dy_1 dx_2 dy_2 A(x_1, y_1; x_2, y_2) \\ \times W_{out}(x_1, y_1; x_2, y_2), \quad (6.44)$$

where $A = \Delta^2 X_-, \Delta^2 Y_+$, respectively. W_{out} is obtained from Eq.(6.43) with W_{in} given in Eq.(6.8) for an EPR entangled state. Figure 6.7 shows the results of calculation. As can be seen, the BS scheme (dashed curve) is very sensitive to losses: the value of I_s increases

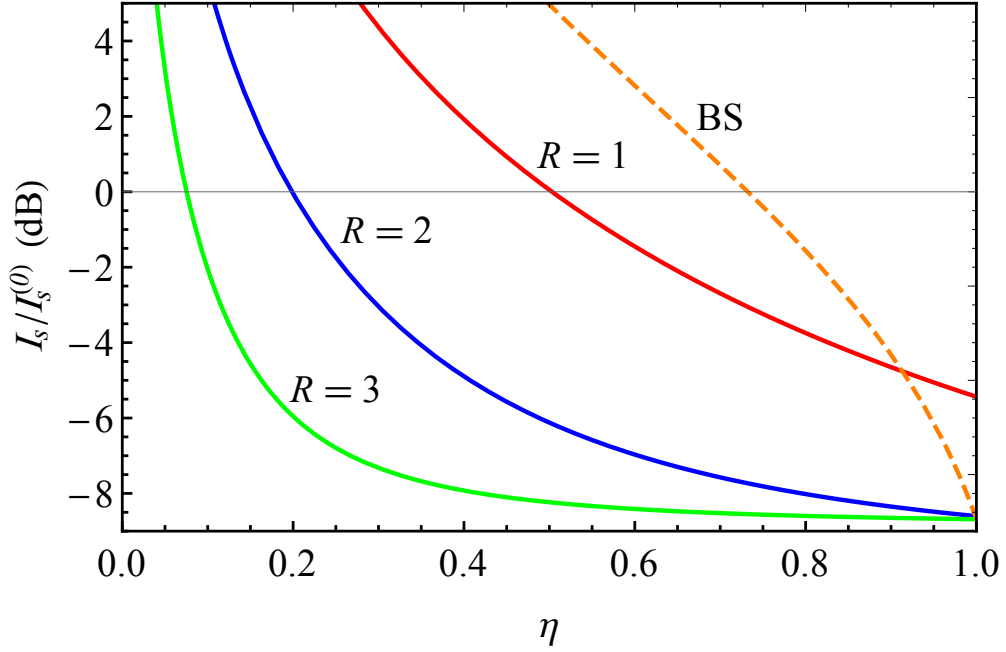


Figure 6.7. Normalized inseparability $I_s/I_s^{(0)}$ ($I_s^{(0)} = 4$ for vacuum) in log-scale as a function of transmission η for the EPR-entangled state with initial input $I_s^{EPR}/I_s^{(0)} = 0.135 = -8.69$ dB for various gain parameters of $R = 1, 2, 3$ for the PA-assisted scheme (solid) and the BS scheme (dashed). The light black line at 0 dB is the threshold for entanglement (Adapted from Ref.[65]).

quickly as detection efficiency η drops and the fields are unentangled for $\eta < 0.7$ (The light black line at 0 dB is the threshold for entanglement). The PA-assisted scheme, on the other hand, can keep I_s at quite a low value with a large gain ($R = 3$) even for η as low as 0.5. Small gain cannot preserve the original I_s value even at no loss $\eta = 1$ but the fields are still entangled up to $\eta = 0.5$.

Comparing Figs.6.6 and 6.7, we find that there is a high correlation between entanglement fidelity F_e and inseparability I_s although there is no direct connection between the two quantities. This reflects that F_e indeed quantifies how well the entanglement is preserved through transmission. In some sense, they both provide general characterization of the transmission quality of the teleportation protocols.

6.6 Summary and Discussion

In summary, we studied the quantum state teleportation scheme with a PA replacing the beam splitter (BS) for field mixing used in the Bell measurement process. With large enough gain for the PA, the new scheme is as good as the original scheme. In addition to field mixing, the PA amplifies input field to a level that is much higher than the vacuum quantum noise so that it can overcome the detection loss in the Bell measurement process, leading to a high teleportation fidelity even in the presence of a large detection loss. This will be especially useful for the spectrum of light where no efficient detector is available. However, internal losses of PA and the losses before PA such as mode mis-match will be the losses imposed on the incoming fields before the PA and thus cannot be overcome by the employment of PA [48]. They will have the same effect as in the BS scheme.

Addition of an active element of PA to replace a passive element like BS will not only require extra resources in the pumping of the PA but also add an extra level of control such as locking of the pump phase to the EPR source. In a real experiment, these can be easily handled, as shown in a recent demonstration in a fiber system [60] where a PA is used to replace a BS in battling the large coupling losses in fibers. The requirement of $R > 2$ discussed in Sect.V for a good fidelity corresponds to $G > 3.8$ or a power gain larger than 15, which can be easily achieved experimentally [60]. On the other hand, larger average

photon number requires higher gain, as shown in Eq.(6.37) and in Fig.6.4, and Fig.6.5. But states with larger photon numbers are more prone to losses in the BS scheme. So, one must balance between the cost and benefit of loss-tolerance in selecting a PA.

The application of PA is not limited to quantum teleportation schemes. The general principle of loss tolerance is applicable to overcome any loss before detection. For example, there may exist large losses in coupling light out of waveguide structure in integrated optics for detection. An on-chip PA will mitigate these losses before detection. On the other hand, the PA scheme can only be used in the final measurement of light and cannot be inserted into a quantum network to overcome losses. This is because the PA amplifies the fields to a macroscopic level that loses the quantum signature of the original input states. Furthermore, the scheme only works for measurement of continuous variables such as homodyne detection but fails in photon counting technique.

6.A Appendix

6.A.1 Derivation of input-output relation of Wigner function for a PA [Eq.(6.6)]

To find the input-output relation, we consider the two-mode Wigner function of a system in the state described by density operator $\hat{\rho}$, which is defined through the following characteristic function:

$$\begin{aligned} \chi(u_1, v_1; u_2, v_2) \\ = \text{Tr}(\hat{\rho} e^{jv_1 \hat{X}_1 - ju_1 \hat{Y}_1 + jv_2 \hat{X}_2 - ju_2 \hat{Y}_2}). \end{aligned} \quad (6.45)$$

The Wigner function is a Fourier transformation of the characteristic function:

$$\begin{aligned} W(x_1, y_1; x_2, y_2) \\ = \frac{1}{(2\pi)^2} \int dx_1 dy_1 dx_2 dy_2 \chi(u_1, v_1; u_2, v_2) \\ \times e^{ju_1 y_1 - jv_1 x_1 + ju_2 y_2 - jv_2 x_2}, \end{aligned} \quad (6.46)$$

Assume the input state is described by a Wigner function $W_{in}(X_1, Y_1; X_2, Y_2)$ for a PA. Since the input-output relations presented in Eqs.(6.4,6.5) are for Heisenberg picture, the state

described by density operator $\hat{\rho}$ is the same for both input and output. Using Eq.(6.4), we find

$$\begin{aligned}
\chi_{out}(u_1, v_1; u_2, v_2) &= \text{Tr}(\hat{\rho} e^{jv_1 \hat{X}_1^{(o)} - ju_1 \hat{Y}_1^{(o)} + jv_2 \hat{X}_2^{(o)} - ju_2 \hat{Y}_2^{(o)}}) \\
&= \text{Tr}(\hat{\rho} e^{jv'_1 \hat{X}_1^{(i)} - ju'_1 \hat{Y}_1^{(i)} + jv'_2 \hat{X}_2^{(i)} - ju'_2 \hat{Y}_2^{(i)}}) \\
&= \chi_{in}(v'_1, u'_1; v'_2, u'_2),
\end{aligned} \tag{6.47}$$

where $u'_1 = u_1 G - u_2 g$, $v'_1 = v_1 G + v_2 g$, $u'_2 = u_2 G - u_1 g$, $v'_2 = v_2 G + v_1 g$. Taking reverse Fourier transformation for W , we find

$$\begin{aligned}
W_{out}^{(PA)}(x_1, y_1; x_2, y_2) &= W_{in}(Gx_1 - gx_2, Gy_1 + gy_2; Gx_2 - gx_1, Gy_2 + gy_1).
\end{aligned} \tag{6.48}$$

6.A.2 Derivation of Eqs.(6.27) and (6.33)

For the scheme with a beam splitter for Bell measurement, we have from Eq.(6.26)

$$W_{out}(X, Y) = \int W_{in}(X - x, Y - y) G_{\bar{\sigma}_1}(x, y) dx dy. \tag{6.49}$$

In terms of Wigner function, the density matrix is

$$\begin{aligned}
\hat{\rho}_{out}(\hat{X}, \hat{Y}) &= \frac{1}{\pi} \int W_{out}(X, Y) e^{jv(\hat{X}-X) + ju(\hat{Y}-Y)} dv du dX dY \\
&= \frac{1}{\pi} \int W_{in}(X - x, Y - y) G_{\bar{\sigma}_1}(x, y) \\
&\quad \times e^{jv(\hat{X}-X) + ju(\hat{Y}-Y)} dv du dX dY dx dy.
\end{aligned} \tag{6.50}$$

Now, let us shift X, Y in $e^{jv(\hat{X}-X)+ju(\hat{Y}-Y)}$ to $X - x, Y - y$ by using operator $\hat{D}(\alpha) \equiv \exp(\alpha\hat{a}^\dagger - \alpha^*\hat{a})$: $\hat{D}(\alpha)\hat{a}\hat{D}^\dagger(\alpha) = \hat{a} - \alpha$. With $\alpha = (x + jy)/2$, we have

$$\begin{aligned} \hat{\rho}_{out}(\hat{X}, \hat{Y}) &= \frac{1}{\pi} \int W_{in}(X - x, Y - y) G_{\bar{\sigma}_1}(x, y) \\ &\quad \times \hat{D}\left(\frac{x + jy}{2}\right) e^{jv[\hat{X} - (X - x)] + ju[\hat{Y} - (Y - y)]} \\ &\quad \times \hat{D}^\dagger\left(\frac{x + jy}{2}\right) dv du dX dY dx dy \end{aligned} \quad (6.51)$$

Making a change of variables: $X - x, Y - y \rightarrow X, Y$ in the integral with respect to X, Y , we have

$$\begin{aligned} \hat{\rho}_{out}(\hat{X}, \hat{Y}) &= \frac{1}{\pi} \int W_{in}(X - x, Y - y) G_{\bar{\sigma}_1}(x, y) \\ &\quad \times \hat{D}\left(\frac{x + jy}{2}\right) e^{jv[\hat{X} - (X - x)] + ju[\hat{Y} - (Y - y)]} \\ &\quad \times \hat{D}^\dagger\left(\frac{x + jy}{2}\right) dv du d(X - x) d(Y - y) dx dy \\ &= \frac{1}{\pi} \int G_{\bar{\sigma}_1}(x, y) \hat{D}\left(\frac{x + jy}{2}\right) W_{in}(X, Y) \\ &\quad \times e^{jv(\hat{X} - X) + ju(\hat{Y} - Y)} dv du dX dY \hat{D}^\dagger\left(\frac{x + jy}{2}\right) dx dy \\ &= \int G_{\bar{\sigma}_1}(x, y) \hat{D}\left(\frac{x + jy}{2}\right) \hat{\rho}_{in}(\hat{X}, \hat{Y}) \hat{D}^\dagger\left(\frac{x + jy}{2}\right) dx dy, \end{aligned} \quad (6.52)$$

which is just Eq.(6.27).

For the scheme with a PA for Bell measurement, we have from Eq.(6.32)

$$\begin{aligned} W_{out}(X, Y) &= \int W_{in}\left(kX - x, \frac{Y}{k} - y\right) \\ &\quad \times G_{\bar{\sigma}_{2x}}(x) G_{\bar{\sigma}_{2y}}(y) dx dy. \end{aligned} \quad (6.53)$$

where $k \equiv g/G$. Defining $W'_{out} \equiv W_{in} \circ G_{\bar{\sigma}_{2x}} G_{\bar{\sigma}_{2x}}$, we have

$$\begin{aligned} W_{out}(X, Y) &= W'_{out}(kX, \frac{Y}{k}) \\ &= \frac{1}{2\pi} \int du \langle kX + u | \hat{\rho}'_{out} | kX - u \rangle e^{-ju \frac{Y}{k}}. \end{aligned} \quad (6.54)$$

Making a change of $U = u/k$ in Eq. (6.54), we have

$$\begin{aligned} W_{out}(X, Y) &= \\ &= \frac{k}{2\pi} \int dU \langle kX + kU | \hat{\rho}'_{out} | kX - kU \rangle e^{-jUY} \\ &= \frac{1}{2\pi} \int dU \langle X + U | \hat{S}(\epsilon) \hat{\rho}'_{out} \hat{S}^\dagger(\epsilon) | X - U \rangle e^{-jUY}, \end{aligned} \quad (6.55)$$

where $\epsilon = -\ln(k) = \ln(G/g)$. From Eqs.(6.52) and (6.54), we have

$$\hat{\rho}'_{out} = \int \hat{D}(\frac{x+yj}{2}) \hat{\rho}_{in} \hat{D}^\dagger(\frac{x+yj}{2}) G_{\bar{\sigma}_{2x}}(x) G_{\bar{\sigma}_{2y}}(y) dx dy \quad (6.56)$$

Therefore, we obtain Eq.(6.33)

$$\begin{aligned} \hat{\rho}_{out} &= \int \hat{S}(\epsilon) \hat{D}(\frac{x+yj}{2}) \hat{\rho}_{in} \hat{D}^\dagger(\frac{x+yj}{2}) \\ &\quad \times \hat{S}^\dagger(\epsilon) G_{\bar{\sigma}_{2x}}(x) G_{\bar{\sigma}_{2y}}(y) dx dy. \end{aligned} \quad (6.57)$$

6.A.3 Fidelity for Coherent States with Finite s and G

The PA scheme requires extra resources and large G to work. We also need to have a large s for the EPR entangled source for both BS and PA schemes. What is the relationship between G and s ?

To answer this, we calculate fidelity F for coherent state input with no approximation applied to G and s . We start from Eq.(6.23) but make the required displacement operation to obtain the final output state as

$$\begin{aligned} W_{out}(x, y) &= C \int dx' dy' e^{-\frac{1}{2\cosh 2s}(x^2+y^2)} W_{in}(x', y') \\ &\quad \times G_{\sigma_{2x}}(x'' - x') G_{\sigma_{2y}}(y'' - y'), \end{aligned} \quad (6.58)$$

with $x'' \equiv x \frac{g}{G} \tanh 2s$, $y'' \equiv y \frac{G}{g} \tanh 2s$, $\sigma_{2x}^2 = \frac{1-\eta^2}{\eta^2 G^2} + \frac{g^2}{G^2 \cosh 2s}$ and $\sigma_{2y}^2 = \frac{1-\eta^2}{\eta^2 g^2} + \frac{G^2}{g^2 \cosh 2s}$ for the PA case. C is a normalization constant. The BS case can be derived in a similar procedure leading to Eq.(6.20) and Eq.(6.23) but without $s \gg 1$ approximation and has the same form as Eq.(6.58) but with $x'' \equiv x \tanh 2s$, $y'' \equiv y \tanh 2s$, and $\sigma_{2x}^2, \sigma_{2y}^2$ both replaced by $\sigma_1 = 2 \frac{1-\eta^2}{\eta^2} + \frac{1}{\cosh 2s}$. Thus, the PA and BS schemes are equivalent as long as $G \approx g$ or $G \gg 1$. This condition is independent of the value of s . Of course, the PA scheme has the advantage of reducing the effect of losses by a factor of $2G^2$.

We next evaluate F from Eq.(6.25) for a coherent state input. The results are

$$\begin{aligned}
F_{BS} &= \frac{2 \left(\tanh^2 2s + \frac{\sigma_1^2 + 1}{\cosh 2s} \right)}{\tanh^2 2s + \sigma_1^2 + 1 + \frac{\sigma_1^2 + 1}{\cosh 2s}} \exp \frac{-2(a^2 + b^2) \left[(1 - \tanh 2s)^2 + \frac{\sigma_1^2 + 2}{\cosh 2s} \right]}{\tanh^2 2s + \sigma_1^2 + 1 + \frac{\sigma_1^2 + 1}{\cosh 2s}} \\
&\quad \exp \frac{2(a^2 + b^2)/\cosh 2s}{\tanh^2 2s + \frac{\sigma_1^2 + 1}{\cosh 2s}} \\
&\approx \frac{1}{1 + \bar{\sigma}_1^2/2} \quad \text{for } s \gg 1,
\end{aligned} \tag{6.59}$$

with $\bar{\sigma}_1 = 2 \frac{1-\eta^2}{\eta^2}$ and

$$\begin{aligned}
F_{PA} &= 2 \sqrt{\frac{\frac{g^2 \tanh^2 2s}{G^2} + \frac{\sigma_{2x}^2 + 1}{\cosh 2s}}{\frac{g^2 \tanh^2 2s}{G^2} + (\sigma_{2x}^2 + 1) \left(1 + \frac{1}{\cosh 2s} \right)}} \sqrt{\frac{\frac{G^2 \tanh^2 2s}{g^2} + \frac{\sigma_{2y}^2 + 1}{\cosh 2s}}{\frac{G^2 \tanh^2 2s}{g^2} + (\sigma_{2y}^2 + 1) \left(1 + \frac{1}{\cosh 2s} \right)}} \\
&\quad \times \exp \frac{-2a^2 \left[\left(1 - \frac{g \tanh 2s}{G} \right)^2 + \frac{\sigma_{2x}^2 + 2}{\cosh(2s)} \right]}{\frac{g^2 \tanh^2 2s}{G^2} + (\sigma_{2x}^2 + 1) \left(1 + \frac{1}{\cosh 2s} \right)} \exp \frac{-2b^2 \left[\left(1 - \frac{G \tanh 2s}{g} \right)^2 + \frac{\sigma_{2y}^2 + 2}{\cosh(2s)} \right]}{\frac{G^2 \tanh^2 2s}{g^2} + (\sigma_{2y}^2 + 1) \left(1 + \frac{1}{\cosh 2s} \right)} \\
&\quad \times \exp \left(\frac{2a^2/\cosh 2s}{\frac{g^2 \tanh^2 2s}{G^2} + \frac{\sigma_{2x}^2 + 1}{\cosh 2s}} + \frac{2b^2/\cosh 2s}{\frac{G^2 \tanh^2 2s}{g^2} + \frac{\sigma_{2y}^2 + 1}{\cosh 2s}} \right).
\end{aligned} \tag{6.60}$$

If $s \gg 1$ so that $\tanh 2s \approx 1$ and $1/\cosh 2s \ll 1$ (independent of G value), the expression above becomes Eq.(6.36). On the other hand, if $G \gg 1$ so that $G \approx g$ and $\sigma_{2x}^2 \approx \sigma_{2y}^2 \approx \sigma_2^2 \equiv \frac{1-\eta^2}{\eta^2 G^2} + \frac{1}{\cosh 2s}$, we have

$$\begin{aligned}
F_{PA} &\approx \frac{2 \left(\tanh^2 2s + \frac{\sigma_2^2 + 1}{\cosh 2s} \right)}{\tanh^2 2s + \sigma_2^2 + 1 + \frac{\sigma_2^2 + 1}{\cosh 2s}} \exp \frac{-2(a^2 + b^2) \left[(1 - \tanh 2s)^2 + \frac{\sigma_2^2 + 2}{\cosh 2s} \right]}{\tanh^2 2s + \sigma_2^2 + 1 + \frac{\sigma_2^2 + 1}{\cosh 2s}} \\
&\quad \times \exp \frac{2(a^2 + b^2)/\cosh 2s}{\tanh^2 2s + \frac{\sigma_2^2 + 1}{\cosh 2s}}
\end{aligned}$$

$$\approx \frac{1}{1 + \bar{\sigma}_2^2/2} \quad \text{for } s \gg 1 \quad (6.61)$$

with $\bar{\sigma}_2 = \frac{1-\eta^2}{\eta^2 G^2}$. Note that the difference between Eq. (6.59) and Eq.(6.61) is in $\sigma_1(\bar{\sigma}_1)$ and $\sigma_2(\bar{\sigma}_2)$ with σ_2 improved upon σ_1 by the reduction of the loss effect term by a factor of $2G^2$.

Comparing the corresponding terms in Eqs.(6.60) and (6.61), we find that their differences are all smaller than $1/G^2$, which is independent of s . Thus the limit of $G \gg 1$ is also independent of s .

7. SUMMARY

We analyze an experimentally implementable method to measure directly the TMs for the quantum states generated by pulse-pumped parametric processes. The method is based on the stimulated emission by a trial pulse and relies on a cross-feedback and iteration loop. We demonstrate the convergence of the procedure by numerical simulations for various situations. The feedback-iteration method is suitable for both the high gain PA, which gives rise to quantum entanglement in continuous variables, and for the low gain case, which produces a two-photon entangled state. Only a small modification is needed for both situations. We also demonstrate experimentally a method that directly determines the temporal/spectral profiles of the eigen-modes for the signal and idler fields generated from a fiber-based PA pumped by a short pulse, and also show that the mode structure depends on the gain of the PA. The technique can be generalized to other pulse-pumped systems such as frequency conversion process or other DOF such as spatial modes to find the eigen-modes of the system. So, the potential applications of the technique is not limited only to quantum optics but can be applied to classical systems as well.

We studied the mode structure for a broadband PA at different gains by using an input-output approach that avoids the crucial issue of time-ordering in Hamiltonian. Contrary to previous studies where the time-ordering issue was not treated, the mode structure changes as the gain increases in the sense that both the mode distribution and the mode functions broaden with the increase of the gain. Although the mode number, a quantity that characterizes the total number of modes, drops initially as the gain changes from low to high due to the dominance of the first mode, it reaches a minimum value before slowly increasing due to the broadening of the mode distribution. The mode structure change with the gain will have a profound impact on the application of broadband parametric processes in quantum technology with continuous variables, which relies on the homodyne detection method as the dominant measurement technique. It means that we will need to measure them constantly at different gains as we change the operation condition. Further study is needed to the availability of the feedback-iteration direct mode measurement method for the high gain PA when considering the time-ordering issue of the interaction Hamiltonian.

We reconstruct the joint spectral density of photon pairs produced by pumped PPKTP crystal with the spontaneous parametric down-conversion process. The measurement method is based on a stimulated emission process compared with old spectrally resolved photons coincidence measurements. It exploits the properties that the spontaneous parametric down-conversion and its counterpart stimulated emission process share the same phase matching configuration and pump spectrum and thus the same spectral correlation function, and can measure the JSD in a relatively short time, and thus improve the accuracy of the results. With reconstruction of the JSD, we can obtain the TM structure indirectly by the mathematical tool singular value decomposition and verify our feedback-iteration method which measures TM structure directly in experiment.

We studied the quantum state teleportation scheme with a PA replacing the beam splitter for field mixing used in the Bell measurement process. The new scheme is as good as the original scheme, when the gain for the PA is large enough. Moreover, because the PA amplifies the input field to a level that is much higher than the vacuum quantum noise, the new scheme can overcome the detection loss in the Bell measurement process, leading to a high teleportation fidelity even in the presence of a large detection loss. This will be especially useful for the spectrum of light where no efficient detector is available.

REFERENCES

- [1] M. A. Nielsen and I. L. Chuang, *Quantum Computation and Quantum Information*. Cambridge University Press, 2000, ISBN: 9780521635035.
- [2] V. Giovannetti, “Quantum-enhanced measurements: Beating the standard quantum limit,” *Science*, vol. 306, no. 5700, pp. 1330–1336, Nov. 2004. DOI: [10.1126/science.1104149](https://doi.org/10.1126/science.1104149). [Online]. Available: <https://doi.org/10.1126/science.1104149>.
- [3] E. Grumbling and M. Horowitz, Eds., *Quantum Computing*. National Academies Press, Mar. 2019. DOI: [10.17226/25196](https://doi.org/10.17226/25196). [Online]. Available: <https://doi.org/10.17226/25196>.
- [4] E. Knill, R. Laflamme, and G. J. Milburn, “A scheme for efficient quantum computation with linear optics,” *Nature*, vol. 409, no. 6816, pp. 46–52, Jan. 2001. DOI: [10.1038/35051009](https://doi.org/10.1038/35051009). [Online]. Available: <https://doi.org/10.1038/35051009>.
- [5] P. Kok, W. J. Munro, K. Nemoto, T. C. Ralph, J. P. Dowling, and G. J. Milburn, “Linear optical quantum computing with photonic qubits,” *Reviews of Modern Physics*, vol. 79, no. 1, pp. 135–174, Jan. 2007. DOI: [10.1103/revmodphys.79.135](https://doi.org/10.1103/revmodphys.79.135). [Online]. Available: <https://doi.org/10.1103/revmodphys.79.135>.
- [6] W. E. Lamb, “Anti-photon,” *Applied Physics B*, vol. 60, no. 2-3, pp. 77–84, Feb. 1995. DOI: [10.1007/bf01135846](https://doi.org/10.1007/bf01135846). [Online]. Available: <https://doi.org/10.1007/bf01135846>.
- [7] C. K. Law, I. A. Walmsley, and J. H. Eberly, “Continuous frequency entanglement: Effective finite hilbert space and entropy control,” *Physical Review Letters*, vol. 84, no. 23, pp. 5304–5307, Jun. 2000. DOI: [10.1103/physrevlett.84.5304](https://doi.org/10.1103/physrevlett.84.5304). [Online]. Available: <https://doi.org/10.1103/physrevlett.84.5304>.
- [8] M. ZUKOWSKI, A. ZEILINGER, and H. WEINFURTER, “Entangling photons radiated by independent pulsed sources,” *Annals of the New York Academy of Sciences*, vol. 755, no. 1, pp. 91–102, Apr. 1995. DOI: [10.1111/j.1749-6632.1995.tb38959.x](https://doi.org/10.1111/j.1749-6632.1995.tb38959.x). [Online]. Available: <https://doi.org/10.1111/j.1749-6632.1995.tb38959.x>.
- [9] J. G. RARITY, “Interference of single photons from separate sources,” *Annals of the New York Academy of Sciences*, vol. 755, no. 1, pp. 624–631, Apr. 1995. DOI: [10.1111/j.1749-6632.1995.tb39002.x](https://doi.org/10.1111/j.1749-6632.1995.tb39002.x). [Online]. Available: <https://doi.org/10.1111/j.1749-6632.1995.tb39002.x>.
- [10] A. Eckstein, B. Brecht, and C. Silberhorn, “A quantum pulse gate based on spectrally engineered sum frequency generation,” *Optics Express*, vol. 19, no. 15, p. 13 770, Jul. 2011. DOI: [10.1364/oe.19.013770](https://doi.org/10.1364/oe.19.013770). [Online]. Available: <https://doi.org/10.1364/oe.19.013770>.

- [11] B. Brecht, A. Eckstein, R. Ricken, V. Quiring, H. Suche, L. Sansoni, and C. Silberhorn, “Demonstration of coherent time-frequency schmidt mode selection using dispersion-engineered frequency conversion,” *Physical Review A*, vol. 90, no. 3, Sep. 2014. DOI: [10.1103/physreva.90.030302](https://doi.org/10.1103/physreva.90.030302). [Online]. Available: <https://doi.org/10.1103/physreva.90.030302>.
- [12] B. Brecht, D. V. Reddy, C. Silberhorn, and M. Raymer, “Photon temporal modes: A complete framework for quantum information science,” *Physical Review X*, vol. 5, no. 4, Oct. 2015. DOI: [10.1103/physrevx.5.041017](https://doi.org/10.1103/physrevx.5.041017). [Online]. Available: <https://doi.org/10.1103/physrevx.5.041017>.
- [13] D. V. Reddy, M. G. Raymer, and C. J. McKinstrie, “Efficient sorting of quantum-optical wave packets by temporal-mode interferometry,” *Optics Letters*, vol. 39, no. 10, p. 2924, May 2014. DOI: [10.1364/ol.39.002924](https://doi.org/10.1364/ol.39.002924). [Online]. Available: <https://doi.org/10.1364/ol.39.002924>.
- [14] D. V. Reddy and M. G. Raymer, “High-selectivity quantum pulse gating of photonic temporal modes using all-optical ramsey interferometry,” *Optica*, vol. 5, no. 4, p. 423, Apr. 2018. DOI: [10.1364/optica.5.000423](https://doi.org/10.1364/optica.5.000423). [Online]. Available: <https://doi.org/10.1364/optica.5.000423>.
- [15] A. Christ, K. Laiho, A. Eckstein, K. N. Cassemiro, and C. Silberhorn, “Probing multimode squeezing with correlation functions,” *New Journal of Physics*, vol. 13, no. 3, p. 033 027, Mar. 2011. DOI: [10.1088/1367-2630/13/3/033027](https://doi.org/10.1088/1367-2630/13/3/033027). [Online]. Available: <https://doi.org/10.1088/1367-2630/13/3/033027>.
- [16] W. Wasilewski, A. I. Lvovsky, K. Banaszek, and C. Radzewicz, “Pulsed squeezed light: Simultaneous squeezing of multiple modes,” *Physical Review A*, vol. 73, no. 6, Jun. 2006. DOI: [10.1103/physreva.73.063819](https://doi.org/10.1103/physreva.73.063819). [Online]. Available: <https://doi.org/10.1103/physreva.73.063819>.
- [17] X. Guo, N. Liu, X. Li, and Z. Y. Ou, “Complete temporal mode analysis in pulse-pumped fiber-optical parametric amplifier for continuous variable entanglement generation,” *Optics Express*, vol. 23, no. 23, p. 29 369, Nov. 2015. DOI: [10.1364/oe.23.029369](https://doi.org/10.1364/oe.23.029369). [Online]. Available: <https://doi.org/10.1364/oe.23.029369>.
- [18] A. O. C. Davis, V. Thiel, and B. J. Smith, “Measuring the quantum state of a photon pair entangled in frequency and time,” *Optica*, vol. 7, no. 10, p. 1317, Sep. 2020. DOI: [10.1364/optica.396933](https://doi.org/10.1364/optica.396933). [Online]. Available: <https://doi.org/10.1364/optica.396933>.

- [19] N. Huo, Y. Liu, J. Li, L. Cui, X. Chen, R. Palivela, T. Xie, X. Li, and Z. Ou, “Direct temporal mode measurement for the characterization of temporally multiplexed high dimensional quantum entanglement in continuous variables,” *Physical Review Letters*, vol. 124, no. 21, May 2020. DOI: [10.1103/physrevlett.124.213603](https://doi.org/10.1103/physrevlett.124.213603). [Online]. Available: <https://doi.org/10.1103/physrevlett.124.213603>.
- [20] M. Liscidini and J. E. Sipe, “Stimulated emission tomography,” *Physical Review Letters*, vol. 111, no. 19, Nov. 2013. DOI: [10.1103/physrevlett.111.193602](https://doi.org/10.1103/physrevlett.111.193602). [Online]. Available: <https://doi.org/10.1103/physrevlett.111.193602>.
- [21] Y.-H. Kim and W. P. Grice, “Measurement of the spectral properties of the two-photon state generated via type II spontaneous parametric downconversion,” *Optics Letters*, vol. 30, no. 8, p. 908, Apr. 2005. DOI: [10.1364/ol.30.000908](https://doi.org/10.1364/ol.30.000908). [Online]. Available: <https://doi.org/10.1364/ol.30.000908>.
- [22] W. Wasilewski, P. Wasylczyk, P. Kolenderski, K. Banaszek, and C. Radzewicz, “Joint spectrum of photon pairs measured by coincidence fourier spectroscopy,” *Optics Letters*, vol. 31, no. 8, p. 1130, Apr. 2006. DOI: [10.1364/ol.31.001130](https://doi.org/10.1364/ol.31.001130). [Online]. Available: <https://doi.org/10.1364/ol.31.001130>.
- [23] M. Avenhaus, A. Eckstein, P. J. Mosley, and C. Silberhorn, “Fiber-assisted single-photon spectrograph,” *Optics Letters*, vol. 34, no. 18, p. 2873, Sep. 2009. DOI: [10.1364/ol.34.002873](https://doi.org/10.1364/ol.34.002873). [Online]. Available: <https://doi.org/10.1364/ol.34.002873>.
- [24] A. Eckstein, G. Boucher, A. Lemaître, P. Filloux, I. Favero, G. Leo, J. E. Sipe, M. Liscidini, and S. Ducci, “High-resolution spectral characterization of two photon states via classical measurements,” *Laser & Photonics Reviews*, vol. 8, no. 5, pp. L76–L80, Jun. 2014. DOI: [10.1002/lpor.201400057](https://doi.org/10.1002/lpor.201400057). [Online]. Available: <https://doi.org/10.1002/lpor.201400057>.
- [25] B. Fang, O. Cohen, M. Liscidini, J. E. Sipe, and V. O. Lorenz, “Fast and highly resolved capture of the joint spectral density of photon pairs,” *Optica*, vol. 1, no. 5, p. 281, Oct. 2014. DOI: [10.1364/optica.1.000281](https://doi.org/10.1364/optica.1.000281). [Online]. Available: <https://doi.org/10.1364/optica.1.000281>.
- [26] S. L. Braunstein and A. Mann, “Measurement of the bell operator and quantum teleportation,” *Physical Review A*, vol. 51, no. 3, R1727–R1730, Mar. 1995. DOI: [10.1103/physreva.51.r1727](https://doi.org/10.1103/physreva.51.r1727). [Online]. Available: <https://doi.org/10.1103/physreva.51.r1727>.
- [27] S. L. Braunstein and H. J. Kimble, “Teleportation of continuous quantum variables,” *Physical Review Letters*, vol. 80, no. 4, pp. 869–872, Jan. 1998. DOI: [10.1103/physrevlett.80.869](https://doi.org/10.1103/physrevlett.80.869). [Online]. Available: <https://doi.org/10.1103/physrevlett.80.869>.

- [28] C. H. Bennett, G. Brassard, C. Crépeau, R. Jozsa, A. Peres, and W. K. Wootters, “Teleporting an unknown quantum state via dual classical and einstein-podolsky-rosen channels,” *Physical Review Letters*, vol. 70, no. 13, pp. 1895–1899, Mar. 1993. DOI: [10.1103/physrevlett.70.1895](https://doi.org/10.1103/physrevlett.70.1895). [Online]. Available: <https://doi.org/10.1103/physrevlett.70.1895>.
- [29] L. Vaidman, “Teleportation of quantum states,” *Physical Review A*, vol. 49, no. 2, pp. 1473–1476, Feb. 1994. DOI: [10.1103/physreva.49.1473](https://doi.org/10.1103/physreva.49.1473). [Online]. Available: <https://doi.org/10.1103/physreva.49.1473>.
- [30] D. Bouwmeester, J.-W. Pan, K. Mattle, M. Eibl, H. Weinfurter, and A. Zeilinger, “Experimental quantum teleportation,” *Nature*, vol. 390, no. 6660, pp. 575–579, Dec. 1997. DOI: [10.1038/37539](https://doi.org/10.1038/37539). [Online]. Available: <https://doi.org/10.1038/37539>.
- [31] A. Furusawa, “Unconditional quantum teleportation,” *Science*, vol. 282, no. 5389, pp. 706–709, Oct. 1998. DOI: [10.1126/science.282.5389.706](https://doi.org/10.1126/science.282.5389.706). [Online]. Available: <https://doi.org/10.1126/science.282.5389.706>.
- [32] A. Einstein, B. Podolsky, and N. Rosen, “Can quantum-mechanical description of physical reality be considered complete?” *Physical Review*, vol. 47, no. 10, pp. 777–780, May 1935. DOI: [10.1103/physrev.47.777](https://doi.org/10.1103/physrev.47.777). [Online]. Available: <https://doi.org/10.1103/physrev.47.777>.
- [33] E. Wigner, “On the quantum correction for thermodynamic equilibrium,” *Physical Review*, vol. 40, no. 5, pp. 749–759, Jun. 1932. DOI: [10.1103/physrev.40.749](https://doi.org/10.1103/physrev.40.749). [Online]. Available: <https://doi.org/10.1103/physrev.40.749>.
- [34] J. S. Bell and A. Aspect, *Speakable and Unsayable in Quantum Mechanics*. Cambridge University Press, Jun. 2004. DOI: [10.1017/cbo9780511815676](https://doi.org/10.1017/cbo9780511815676). [Online]. Available: <https://doi.org/10.1017/cbo9780511815676>.
- [35] P. A. Franken, A. E. Hill, C. W. Peters, and G. Weinreich, “Generation of optical harmonics,” *Physical Review Letters*, vol. 7, no. 4, pp. 118–119, Aug. 1961. DOI: [10.1103/physrevlett.7.118](https://doi.org/10.1103/physrevlett.7.118). [Online]. Available: <https://doi.org/10.1103/physrevlett.7.118>.
- [36] N. Quesada and J. E. Sipe, “Why you should not use the electric field to quantize in nonlinear optics,” *Optics Letters*, vol. 42, no. 17, p. 3443, Aug. 2017. DOI: [10.1364/ol.42.003443](https://doi.org/10.1364/ol.42.003443). [Online]. Available: <https://doi.org/10.1364/ol.42.003443>.
- [37] Z. J. Ou, *Quantum Optics for Experimentalists*. WORLD SCIENTIFIC, Feb. 2017. DOI: [10.1142/10453](https://doi.org/10.1142/10453). [Online]. Available: <https://doi.org/10.1142/10453>.

- [38] C. F. V. Loan, “Generalizing the singular value decomposition,” *SIAM Journal on Numerical Analysis*, vol. 13, no. 1, pp. 76–83, Mar. 1976. DOI: [10.1137/0713009](https://doi.org/10.1137/0713009). [Online]. Available: <https://doi.org/10.1137/0713009>.
- [39] X. Chen, X. Li, and Z. Y. Ou, “Direct temporal mode measurement of photon pairs by stimulated emission,” *Physical Review A*, vol. 101, no. 3, Mar. 2020. DOI: [10.1103/physreva.101.033838](https://doi.org/10.1103/physreva.101.033838). [Online]. Available: <https://doi.org/10.1103/physreva.101.033838>.
- [40] I. A. Walmsley and C. Dorrer, “Characterization of ultrashort electromagnetic pulses,” *Advances in Optics and Photonics*, vol. 1, no. 2, p. 308, Apr. 2009. DOI: [10.1364/aop.1.000308](https://doi.org/10.1364/aop.1.000308). [Online]. Available: <https://doi.org/10.1364/aop.1.000308>.
- [41] N. Quesada and J. E. Sipe, “Effects of time ordering in quantum nonlinear optics,” *Physical Review A*, vol. 90, no. 6, Dec. 2014. DOI: [10.1103/physreva.90.063840](https://doi.org/10.1103/physreva.90.063840). [Online]. Available: <https://doi.org/10.1103/physreva.90.063840>.
- [42] C. Polycarpou, K. N. Cassemiro, G. Venturi, A. Zavatta, and M. Bellini, “Adaptive detection of arbitrarily shaped ultrashort quantum light states,” *Physical Review Letters*, vol. 109, no. 5, Aug. 2012. DOI: [10.1103/physrevlett.109.053602](https://doi.org/10.1103/physrevlett.109.053602). [Online]. Available: <https://doi.org/10.1103/physrevlett.109.053602>.
- [43] J. Li, J. Su, L. Cui, T. Xie, Z. Y. Ou, and X. Li, “Generation of pure-state single photons with high heralding efficiency by using a three-stage nonlinear interferometer,” *Applied Physics Letters*, vol. 116, no. 20, p. 204 002, May 2020. DOI: [10.1063/5.0003601](https://doi.org/10.1063/5.0003601). [Online]. Available: <https://doi.org/10.1063/5.0003601>.
- [44] J. Su, L. Cui, J. Li, Y. Liu, X. Li, and Z. Y. Ou, “Versatile and precise quantum state engineering by using nonlinear interferometers,” *Optics Express*, vol. 27, no. 15, p. 20 479, Jul. 2019. DOI: [10.1364/oe.27.020479](https://doi.org/10.1364/oe.27.020479). [Online]. Available: <https://doi.org/10.1364/oe.27.020479>.
- [45] P. R. Sharapova, G. Frascella, M. Riabinin, A. M. Pérez, O. V. Tikhonova, S. Lemieux, R. W. Boyd, G. Leuchs, and M. V. Chekhova, “Properties of bright squeezed vacuum at increasing brightness,” *Physical Review Research*, vol. 2, no. 1, Mar. 2020. DOI: [10.1103/physrevresearch.2.013371](https://doi.org/10.1103/physrevresearch.2.013371). [Online]. Available: <https://doi.org/10.1103/physrevresearch.2.013371>.
- [46] X. Guo, X. Li, N. Liu, and Z. Y. Ou, “Multimode theory of pulsed-twin-beam generation using a high-gain fiber-optical parametric amplifier,” *Physical Review A*, vol. 88, no. 2, Aug. 2013. DOI: [10.1103/physreva.88.023841](https://doi.org/10.1103/physreva.88.023841). [Online]. Available: <https://doi.org/10.1103/physreva.88.023841>.

- [47] Z. J. Ou, *Multi-Photon Quantum Interference*. Springer US, 2007. DOI: [10.1007/978-0-387-25554-5](https://doi.org/10.1007/978-0-387-25554-5). [Online]. Available: <https://doi.org/10.1007/978-0-387-25554-5>.
- [48] Z. Y. Ou, “Enhancement of the phase-measurement sensitivity beyond the standard quantum limit by a nonlinear interferometer,” *Physical Review A*, vol. 85, no. 2, Feb. 2012. DOI: [10.1103/physreva.85.023815](https://doi.org/10.1103/physreva.85.023815). [Online]. Available: <https://doi.org/10.1103/physreva.85.023815>.
- [49] X. Chen, J. Zhang, and Z. Y. Ou, “Mode structure of a broadband high gain parametric amplifier,” *Physical Review Research*, vol. 3, no. 2, Jun. 2021. DOI: [10.1103/physrevresearch.3.023186](https://doi.org/10.1103/physrevresearch.3.023186). [Online]. Available: <https://doi.org/10.1103/physrevresearch.3.023186>.
- [50] Z. Y. Ou and X. Li, “Quantum $SU(1, 1)$ interferometers: Basic principles and applications,” *APL Photonics*, vol. 5, no. 8, p. 080 902, Aug. 2020. DOI: [10.1063/5.0004873](https://doi.org/10.1063/5.0004873). [Online]. Available: <https://doi.org/10.1063/5.0004873>.
- [51] F. Hudelist, J. Kong, C. Liu, J. Jing, Z. Ou, and W. Zhang, “Quantum metrology with parametric amplifier-based photon correlation interferometers,” *Nature Communications*, vol. 5, no. 1, Jan. 2014. DOI: [10.1038/ncomms4049](https://doi.org/10.1038/ncomms4049). [Online]. Available: <https://doi.org/10.1038/ncomms4049>.
- [52] G. B. Lemos, V. Borish, G. D. Cole, S. Ramelow, R. Lapkiewicz, and A. Zeilinger, “Quantum imaging with undetected photons,” *Nature*, vol. 512, no. 7515, pp. 409–412, Aug. 2014. DOI: [10.1038/nature13586](https://doi.org/10.1038/nature13586). [Online]. Available: <https://doi.org/10.1038/nature13586>.
- [53] L. Cui, J. Su, J. Li, Y. Liu, X. Li, and Z. Y. Ou, “Quantum state engineering by nonlinear quantum interference,” *Physical Review A*, vol. 102, no. 3, Sep. 2020. DOI: [10.1103/physreva.102.033718](https://doi.org/10.1103/physreva.102.033718). [Online]. Available: <https://doi.org/10.1103/physreva.102.033718>.
- [54] N. Quesada, G. Triginer, M. D. Vidrighin, and J. E. Sipe, “Theory of high-gain twin-beam generation in waveguides: From maxwell’s equations to efficient simulation,” *Physical Review A*, vol. 102, no. 3, Sep. 2020. DOI: [10.1103/physreva.102.033519](https://doi.org/10.1103/physreva.102.033519). [Online]. Available: <https://doi.org/10.1103/physreva.102.033519>.
- [55] O. Aytür and P. Kumar, “Pulsed twin beams of light,” *Physical Review Letters*, vol. 65, no. 13, pp. 1551–1554, Sep. 1990. DOI: [10.1103/physrevlett.65.1551](https://doi.org/10.1103/physrevlett.65.1551). [Online]. Available: <https://doi.org/10.1103/physrevlett.65.1551>.

- [56] N. Liu, Y. Liu, X. Guo, L. Yang, X. Li, and Z. Ou, “Approaching single temporal mode operation in twin beams generated by pulse pumped high gain spontaneous four wave mixing,” *Optics Express*, vol. 24, no. 2, p. 1096, Jan. 2016. DOI: [10.1364/oe.24.001096](https://doi.org/10.1364/oe.24.001096). [Online]. Available: <https://doi.org/10.1364/oe.24.001096>.
- [57] P. Sharapova, A. M. Pérez, O. V. Tikhonova, and M. V. Chekhova, “Schmidt modes in the angular spectrum of bright squeezed vacuum,” *Physical Review A*, vol. 91, no. 4, Apr. 2015. DOI: [10.1103/physreva.91.043816](https://doi.org/10.1103/physreva.91.043816). [Online]. Available: <https://doi.org/10.1103/physreva.91.043816>.
- [58] I. V. Dyakonov, P. R. Sharapova, T. S. Iskhakov, and G. Leuchs, “Direct schmidt number measurement of high-gain parametric down conversion,” *Laser Physics Letters*, vol. 12, no. 6, p. 065202, May 2015. DOI: [10.1088/1612-2011/12/6/065202](https://doi.org/10.1088/1612-2011/12/6/065202). [Online]. Available: <https://doi.org/10.1088/1612-2011/12/6/065202>.
- [59] H. S. Poh, C. Y. Lum, I. Marcikic, A. Lamas-Linares, and C. Kurtsiefer, “Joint spectrum mapping of polarization entanglement in spontaneous parametric down-conversion,” *Physical Review A*, vol. 75, no. 4, Apr. 2007. DOI: [10.1103/physreva.75.043816](https://doi.org/10.1103/physreva.75.043816). [Online]. Available: <https://doi.org/10.1103/physreva.75.043816>.
- [60] J. Li, Y. Liu, N. Huo, L. Cui, C. Feng, Z. Y. Ou, and X. Li, “Pulsed entanglement measured by parametric amplifier assisted homodyne detection,” *Optics Express*, vol. 27, no. 21, p. 30552, Oct. 2019. DOI: [10.1364/oe.27.030552](https://doi.org/10.1364/oe.27.030552). [Online]. Available: <https://doi.org/10.1364/oe.27.030552>.
- [61] C. M. Caves, “Quantum limits on noise in linear amplifiers,” *Physical Review D*, vol. 26, no. 8, pp. 1817–1839, Oct. 1982. DOI: [10.1103/physrevd.26.1817](https://doi.org/10.1103/physrevd.26.1817). [Online]. Available: <https://doi.org/10.1103/physrevd.26.1817>.
- [62] Z. Y. Ou, “Quantum amplification with correlated quantum fields,” *Physical Review A*, vol. 48, no. 3, R1761–R1764, Sep. 1993. DOI: [10.1103/physreva.48.r1761](https://doi.org/10.1103/physreva.48.r1761). [Online]. Available: <https://doi.org/10.1103/physreva.48.r1761>.
- [63] J. Kong, F. Hudelist, Z. Y. Ou, and W. Zhang, “Cancellation of internal quantum noise of an amplifier by quantum correlation,” *Physical Review Letters*, vol. 111, no. 3, Jul. 2013. DOI: [10.1103/physrevlett.111.033608](https://doi.org/10.1103/physrevlett.111.033608). [Online]. Available: <https://doi.org/10.1103/physrevlett.111.033608>.
- [64] Z. Y. Ou, S. F. Pereira, and H. J. Kimble, “Realization of the einstein-podolsky-rosen paradox for continuous variables in nondegenerate parametric amplification,” *Applied Physics B Photophysics and Laser Chemistry*, vol. 55, no. 3, pp. 265–278, Sep. 1992. DOI: [10.1007/bf00325015](https://doi.org/10.1007/bf00325015). [Online]. Available: <https://doi.org/10.1007/bf00325015>.

- [65] X. Chen and Z. Y. Ou, “Parametric amplifier for bell measurement in continuous-variable quantum state teleportation,” *Physical Review A*, vol. 102, no. 3, Sep. 2020. DOI: [10.1103/physreva.102.032407](https://doi.org/10.1103/physreva.102.032407). [Online]. Available: <https://doi.org/10.1103/physreva.102.032407>.
- [66] R. E. S. Polkinghorne and T. C. Ralph, “Continuous variable entanglement swapping,” *Physical Review Letters*, vol. 83, no. 11, pp. 2095–2099, Sep. 1999. DOI: [10.1103/physrevlett.83.2095](https://doi.org/10.1103/physrevlett.83.2095). [Online]. Available: <https://doi.org/10.1103/physrevlett.83.2095>.
- [67] P. van Loock and S. Braunstein, “Unconditional teleportation of continuous-variable entanglement,” in *Quantum Electronics and Laser Science Conference (QELS 2000). Technical Digest. Postconference Edition. TOPS Vol.40 (IEEE Cat. No.00CH37089)*, 2000, pp. 223–224.
- [68] O. Glöckl, S. Lorenz, C. Marquardt, J. Heersink, M. Brownnutt, C. Silberhorn, Q. Pan, P. van Loock, N. Korolkova, and G. Leuchs, “Experiment towards continuous-variable entanglement swapping: Highly correlated four-partite quantum state,” *Physical Review A*, vol. 68, no. 1, Jul. 2003. DOI: [10.1103/physreva.68.012319](https://doi.org/10.1103/physreva.68.012319). [Online]. Available: <https://doi.org/10.1103/physreva.68.012319>.
- [69] R. Jozsa, “Fidelity for mixed quantum states,” *Journal of Modern Optics*, vol. 41, no. 12, pp. 2315–2323, Dec. 1994. DOI: [10.1080/09500349414552171](https://doi.org/10.1080/09500349414552171). [Online]. Available: <https://doi.org/10.1080/09500349414552171>.
- [70] B. Schumacher, “Sending entanglement through noisy quantum channels,” *Physical Review A*, vol. 54, no. 4, pp. 2614–2628, Oct. 1996. DOI: [10.1103/physreva.54.2614](https://doi.org/10.1103/physreva.54.2614). [Online]. Available: <https://doi.org/10.1103/physreva.54.2614>.
- [71] L.-M. Duan, G. Giedke, J. I. Cirac, and P. Zoller, “Inseparability criterion for continuous variable systems,” *Physical Review Letters*, vol. 84, no. 12, pp. 2722–2725, Mar. 2000. DOI: [10.1103/physrevlett.84.2722](https://doi.org/10.1103/physrevlett.84.2722). [Online]. Available: <https://doi.org/10.1103/physrevlett.84.2722>.